



# UNIVERSITÀ DI PARMA

## ARCHIVIO DELLA RICERCA

University of Parma Research Repository

Chemical and isotope composition of the oilfield brines from Mishrif Formation (southern Iraq): Diagenesis and geothermometry

This is the peer reviewed version of the following article:

*Original*

Chemical and isotope composition of the oilfield brines from Mishrif Formation (southern Iraq): Diagenesis and geothermometry / Boschetti, Tiziano; Awadh, Salih Muhammad; Al-Mimar, Heba Sadoon; Iacumin, Paola; Toscani, Lorenzo; Selmo, Enricomaria; Yaseen, Zaher Mundher. - In: MARINE AND PETROLEUM GEOLOGY. - ISSN 0264-8172. - 122:(2020). [10.1016/j.marpetgeo.2020.104637]

*Availability:*

This version is available at: 11381/2879725 since: 2024-12-16T10:00:01Z

*Publisher:*

Elsevier Ltd

*Published*

DOI:10.1016/j.marpetgeo.2020.104637

*Terms of use:*

Anyone can freely access the full text of works made available as "Open Access". Works made available

*Publisher copyright*

note finali coverpage

(Article begins on next page)

21 April 2025

Manuscript Number: JMPG-D-19-01563R4

Title: Chemical and isotope composition of the oilfield brines from Mishrif Formation (southern Iraq): Diagenesis and geothermometry

Article Type: Full Length Article

Keywords: Oilfield waters; chemical composition; geothermometry; oxygen and hydrogen stable isotope ratios; strontium isotopes.

Corresponding Author: Dr. Zaher Mundher Yaseen, P.h.D

Corresponding Author's Institution: Ton Duc Thang University

First Author: Tiziano Boschetti

Order of Authors: Tiziano Boschetti; Salih Muhammad Awadh; Heba Sadoon Al-Mimar; Paola Iacumin; Lorenzo Toscani; Enricomaria Selmo; Zaher Mundher Yaseen, P.h.D

Abstract: This paper focuses on the geochemical composition and isotope geochemistry of brines in the Cenomanian-Turonian carbonate Mishrif reservoir of southern Iraq. Main dissolved constituents, trace elements,  $\delta^2\text{H}$  and  $\delta^{18}\text{O}$ ,  $87\text{Sr}/86\text{Sr}$ , mineral saturation indices and thermodynamic calculations were investigated in formation waters from the Mishrif Formation to obtain a better understanding of brine evolution and diagenetic effects over geological time. Previous published  $\delta^{11}\text{B}$  data were also reinterpreted as a geothermometer tool. The results are compared with previous published data for local oilfields and coeval formations in the Arabian Gulf. The Mishrif brine has a marine origin and is diagenetically modified to Ca-excess and Na-deficit. Formation waters are quartz supersaturated and are in equilibrium with chalcedony and calcite-dolomite in the temperatures range of 50-75°C, which is also confirmed by calcite-water oxygen isotope fractionation and  $\delta^{11}\text{B}$  geothermometer. The potential role of clays in conditioning brine chemistry during diagenetic processes was highlighted by activity diagrams; in particular, their adsorption/exchange effect on sodium could explain the lower temperature obtained by the Na/Li geothermometer (42 ± 6 °C). The  $\delta^2\text{H}$  and  $\delta^{18}\text{O}$  values show that oxygen isotope composition of the brines was isotopically more affected by interaction with limestone during diagenesis than seawater evaporation. The main effect is an  $^{18}\text{O}$ -enrichment on the brine starting from the SMOW value. Locally, dilution by present-day meteoric water was also detected (Rumaila South), which is shifted towards the local meteoric water line. The strontium isotope ratios range from 0.707713 to 0.707749 and correspond to a marine strontium of late Cenomanian-early Maastrichtian age, except for the Majnoon sample, which shows a more radiogenic value (0.708043). Radiogenic strontium and gypsum and anhydrite saturation indices of the Majnoon sample could indicate the contribution of calcium and sulphate from the strontium-rich sulphate minerals of the Cambrian salt domes occurring in the oilfields of southern Iraq. The higher manganese concentration (4 mg/l) and the slightly higher temperature inferred by geothermometers (up to 74 °C) in comparison with present-day could

indicate that the Majnoon brine is a hot fluid, probably related to a deeper structure such as the Zagros Foredeep Fault.

Research Data Related to this Submission

-----  
There are no linked research data sets for this submission. The following reason is given:

The used data has been reported in the manuscript.

1  
2  
3  
4 **Chemical and isotope composition of the oilfield brines from Mishrif**  
5  
6  
7 **Formation (southern Iraq): Diagenesis and geothermometry**  
8  
9

10 The authors very much appreciate the respected Editor for his constructive revision and all the  
11 technical and grammatical corrections.  
12

13 IMPORTANT NOTE: Reviewer attachments may have been uploaded to EES. If there are  
14 attachments for your paper, you can view them by clicking on the View Reviewer Attachments  
15 action link in EES.  
16

17  
18 Reviewers' comments:

19  
20 Associate Editor Katz's comments:

21  
22 \* Please review the highlighted wording, grammar and style revisions and make the appropriate  
23 revisions.  
24

25 **- All the reported language edits have been revised and modified accordingly.**  
26  
27  
28  
29  
30  
31  
32  
33  
34  
35  
36  
37  
38  
39  
40  
41  
42  
43  
44  
45  
46  
47  
48  
49  
50  
51  
52  
53  
54  
55  
56  
57  
58  
59  
60  
61  
62  
63  
64  
65

## Highlights

- Sr, O and H isotopic composition of formation brine from southern Iraq are presented
- Calcite-dolomite and chalcedony equilibria with water were achieved during diagenesis
- Chemically inferred and calcite-water oxygen isotope fractionation temperature agree
- Mineralogical composition is confirmed by plotting water samples on activity diagram

1  
2  
3  
4  
5  
6  
7  
8  
9  
10  
11  
12  
13  
14  
15  
16  
17  
18  
19  
20  
21  
22  
23  
24  
25  
26  
27  
28  
29  
30  
31  
32  
33  
34  
35  
36  
37  
38  
39  
40  
41  
42  
43  
44  
45  
46  
47  
48  
49  
50  
51  
52  
53  
54  
55  
56  
57  
58  
59  
60  
61  
62  
63  
64  
65

1           **Chemical and isotope composition of the oilfield brines from Mishrif**

2           **Formation (southern Iraq): Diagenesis and geothermometry**

3           Tiziano Boschetti<sup>1</sup>, Salih Muhammad Awadh<sup>2</sup>, Heba Sadoon Al-Mimar<sup>2</sup>, Paola Iacumin<sup>1</sup>,

4           Lorenzo Toscani<sup>1</sup>, Enricomaria Selmo<sup>1</sup>, Zaher Mundher Yaseen<sup>3,\*</sup>

5           <sup>1</sup> Department of Chemistry, Life Sciences and Environmental Sustainability, University of

6           Parma, Parco Area delle Scienze 157/A, 43124 Parma, Italy

7           <sup>2</sup> Department of Geology, College of Science, University of Baghdad, Baghdad, Iraq

8           <sup>3</sup> Sustainable Developments in Civil Engineering Research Group, Faculty of Civil

9           Engineering, Ton Duc Thang University, Ho Chi Minh City, Vietnam

10           \*Corresponding authors: Zaher Mundher Yaseen

11           Email: [yaseen@tdtu.edu.vn](mailto:yaseen@tdtu.edu.vn)

## 26 **Abstract**

27 This paper focuses on the geochemical composition and isotope geochemistry of brines in the  
28 Cenomanian–Turonian carbonate Mishrif reservoir of southern Iraq. Main dissolved  
29 constituents, trace elements,  $\delta^2\text{H}$  and  $\delta^{18}\text{O}$ ,  $^{87}\text{Sr}/^{86}\text{Sr}$ , mineral saturation indices and  
30 thermodynamic calculations were investigated in formation waters from the Mishrif  
31 Formation to obtain a better understanding of brine evolution and diagenetic effects over  
32 geological time. Previous published  $\delta^{11}\text{B}$  data were also reinterpreted as a geothermometer  
33 tool. The results are compared with previous published data for local oilfields and coeval  
34 formations in the Arabian Gulf. The Mishrif brine has a marine origin and is diagenetically  
35 modified to Ca-excess and Na-deficit. Formation waters are quartz supersaturated and are in  
36 equilibrium with chalcedony and calcite-dolomite in the temperatures range of 50–75°C,  
37 which is also confirmed by calcite-water oxygen isotope fractionation and  $\delta^{11}\text{B}$   
38 geothermometer. The potential role of clays in conditioning brine chemistry during diagenetic  
39 processes was highlighted by activity diagrams; in particular, their adsorption/exchange  
40 effect on sodium could explain the lower temperature obtained by the Na/Li geothermometer  
41 ( $42 \pm 6$  °C). The  $\delta^2\text{H}$  and  $\delta^{18}\text{O}$  values show that oxygen isotope composition of the brines  
42 was isotopically more affected by interaction with limestone during diagenesis than seawater  
43 evaporation. The main effect is an  $^{18}\text{O}$ -enrichment on the brine starting from the SMOW  
44 value. Locally, dilution by present-day meteoric water was also detected (Rumaila South),  
45 which is shifted towards the local meteoric water line. The strontium isotope ratios range  
46 from 0.707713 to 0.707749 and correspond to a marine strontium of late Cenomanian–early  
47 Maastrichtian age, except for the Majnoon sample, which shows a more radiogenic value  
48 (0.708043). Radiogenic strontium and gypsum and anhydrite saturation indices of the  
49 Majnoon sample could indicate the contribution of calcium and sulphate from the strontium-  
50 rich sulphate minerals of the Cambrian salt domes occurring in the oilfields of southern Iraq.

1  
2  
3  
4  
5  
6  
7  
8  
9  
10  
11  
12  
13  
14  
15  
16  
17  
18  
19  
20  
21  
22  
23  
24  
25  
26  
27  
28  
29  
30  
31  
32  
33  
34  
35  
36  
37  
38  
39  
40  
41  
42  
43  
44  
45  
46  
47  
48  
49  
50  
51  
52  
53  
54  
55  
56  
57  
58  
59  
60  
61  
62  
63  
64  
65  
66  
67  
68  
69  
70  
71  
72  
73  
74  
75  
76  
77  
78  
79  
80  
81  
82  
83  
84  
85  
86  
87  
88  
89  
90  
91  
92  
93  
94  
95  
96  
97  
98  
99  
100

The higher manganese concentration (4 mg/l) and the slightly higher temperature inferred by geothermometers (up to 74 °C) in comparison with present-day could indicate that the Majnoon brine is a hot fluid, probably related to a deeper structure such as the Zagros Foredeep Fault.

**Keywords:** Oilfield waters; chemical composition; geothermometry; oxygen and hydrogen stable isotope ratios; strontium isotopes.

## 1. Introduction

In the Jurassic–Cretaceous petroleum system of southern Iraq, hydrocarbons are mainly trapped in Lower Cretaceous sandstone and carbonate reservoirs. Crude oil is generated from the organic-rich Upper Jurassic (Sargelu and Sulaiy formations) changing the Lower Cretaceous carbonates of the Yamama Formation and the Zubair Formation, a clastics reservoir (Abeed et al., 2012; Abeed et al., 2013). The chemical composition of formation waters from the Yamama reservoir in the Zubair and North/South Rumaila oilfields is mainly composed of chloride (up to 143,589 ppm) with a salinity 6.2 times higher than seawater (Jamil, 1978), as for West Qurna oilfield, salinity 7.3 times higher than seawater and dominated by 191,700 ppm of chloride (Al-Marsoumi and Abdul-Wahab, 2005). These prior works utilized brine chemistry but did not address the evolution of the reservoir brine, as they relied mainly on cations and anions without considering isotopes. More recently, the boron stable isotope ratio of the brine from the Mishrif reservoir has given a seawater signature (Awadh et al., 2019a; Awadh et al., 2018) and highlighted the role of salinity in generating the formation pressure and controlling the fluid flow (Al-Mimar and Awadh, 2019). The developing of the oilfield brines over the geological time and its response to the flooding and diagenesis have a significant impact on petroleum reservoir quality, but this subject has not yet been investigated.



1  
2  
3  
4  
5  
6  
7  
8  
9  
10  
11  
12  
13  
14  
15  
16  
17  
18  
19  
20  
21  
22  
23  
24  
25  
26  
27  
28  
29  
30  
31  
32  
33  
34  
35  
36  
37  
38  
39  
40  
41  
42  
43  
44  
45  
46  
47  
48  
49  
50  
51  
52  
53  
54  
55  
56  
57  
58  
59  
60  
61  
62  
63  
64  
65

75 The diagenetic effects on brine waters can be evaluated by comparing the Na, Ca and  
76 Cl concentrations of the brine with those of seawater and with the so-called basinal fluid line  
77 in the Ca-excess versus Na-deficit binary diagram (Davisson and Criss, 1996). However, in  
78 this plot the interpretation could be misguided because: (i) the reference basinal fluid line  
79 takes into account only plagioclase albitisation, often without checking the real  
80 thermodynamic equilibria state of the involved waters; and ii) modelling involves the current  
81 seawater composition disregarding that of past periods (Babel and Schreiber, 2014;  
82 Lowenstein et al., 2003). A combination of isotope parameters as O-H stable isotope ratios  
83 and  $^{87}\text{Sr}/^{86}\text{Sr}$  was proposed by Danquigny et al. (2005) to evaluate the effect of water  
84 flooding in the Mishrif Formation water of Qatar. However, in that work, seawater  
85 evaporation, the isotope salt effect (Horita et al., 1993), and the contribution of radiogenic  
86 strontium to the limestones of the Mishrif Formation were not considered.

75 The objectives of this research are: i) to investigate the origin of the oilfield waters; ii)  
76 to evaluate the composition of oilfield waters over time; and iii) to trace the influence of  
77 diagenesis and any geothermal effects on the brine. This investigation considers the above  
78 described effects and processes in the Mishrif Formation brines by reinterpreting the  
79 previously published main chemical constituents, along with new and original data on trace  
80 elements, oxygen and hydrogen water isotope ratio, the  $^{87}\text{Sr}/^{86}\text{Sr}$  ratio, and thermodynamic  
81 calculations. Moreover, the previously published data of boron isotope ratio  $\delta^{11}\text{B}$  (Awadh et  
82 al., 2019a; Awadh et al., 2018) are here reinterpreted as a geothermometer tool, and are  
83 results compared with those obtained from chemical geothermometers. The main research  
84 contribution is to obtain better understanding of the oilfield brines evolution.

## 97 **2. Geological setting**

### 98 *2.1. Oilfield locations, main geological features and tectonics*

99 The studied oilfields, Rumaila South (RU), Rumaila North (R), West Qurna (WQ), Zubair  
100 (ZB) and Majnoon (MJ) are located in southern part of Iraq (Jassim and Buday, 2006) (Fig.  
101 1A). The Mesopotamian zone extends from middle to southern Iraq as a relatively flat terrain  
102 with a gradient of less than 10 cm/km in the north-west to the Arabian Gulf. The zone was  
103 probably uplifted during Hercynian deformation but was subject to subsidence from the Late  
104 Permian onwards (Jassim and Buday, 2006). The oilfields are located in the Zubair zone  
105 (Grabowski Jr., 2014; Sadooni and Aqrabi, 2000), southern part of the Mesopotamia plain  
106 (Fig. 1A), an area characterized by the presence of a gentle subsurface succession of  
107 anticlinal and synclinal structures. These structures form giant hydrocarbon traps: Rumaila  
108 South (37 km length, 16 km width), Rumaila North (40 km, 13.5 km), West Qurna (35 km, 8  
109 km) and Majnoon (48 km, 10 km).

110 From the interpretation of gravity and magnetic data, Alyasi et al. (2014) mentioned  
111 that the presence of anticlinal structures is due to the effect of the evaporites of the Late  
112 Jurassic Gotnia Formation and Late Ediacaran – Early Cambrian Hormuz Formation in  
113 addition to other tectonic forces, where salts moves upward by buoyant forces and the denser  
114 rocks remain below them. To the north of the Arabian Gulf, huge salt-gypsum domes are  
115 exposed at a surface coexisting with a mixture of igneous and metamorphic rocks peeled off  
116 from the Precambrian crystalline basement (Mortazavi et al., 2017). Jabal Sanam is one of the  
117 salt diapirs in southern Iraq / northern Kuwait border (Fig. 1); it is an extension of the  
118 Hormuz Formation, located in Iran at the northern part of the Arabian Gulf, which contains  
119 more than 200 salt domes composed of sequences of evaporates, shales, siltstones and  
120 carbonates (Mortazavi et al., 2017). The role of tectonic events (extensional faulting) and  
121 differential loading of sedimentary cover above the mobile salt layer are the main triggering  
122 factors of the salt diapirism (Singh, 2012). In particular, the Permo-Triassic Tethyan rifting,  
123 the Cretaceous-Paleogene obduction and the compressive events associated with basement

124 reactivation of north-south Arabian trends could have started the episodic salt diapir activity  
125 in the area of this study (Singh, 2012). However, traces of a neotectonic reactivation were  
126 also documented (Sissakian et al., 2017).

127 The Zubair zone is a southern part of the Mesopotamian Basin that is located close to  
128 the junction of the Arabian Shelf and Iranian continental block. Collision of these plates at  
129 the Mesozoic-Cenozoic boundary produced the Zagros Foredeep fault and the Mesopotamian  
130 Basin, which is a member of the Arabian Gulf Basin (Konyuhov and Maleki, 2006). During  
131 the Mesozoic and Cenozoic, the study area was a tropical region, with organic-rich  
132 carbonates or organic-rich argillaceous sediments being deposited. Good-quality source rocks  
133 were preserved in different intervals of geological time, particularly during the Mesozoic. For  
134 example (Fig. 1B): the Alan Formation in the Middle Jurassic; the Sargelu, Najmah and  
135 Sulaiy formations are the source rocks in the Upper Jurassic; the Yamama Formation is a  
136 reservoir and productive carbonate and the Zubair Formation is a reservoir and productive  
137 sand in the Lower Cretaceous; the Ratawi, Shuaiba and Nahr Umr formations are carbonate  
138 reservoirs in the Lower Cretaceous. The Mauddud, Ahmadi and Rumaila formations are the  
139 mainly carbonate reservoirs in the Cenomanian. The Mishrif Formation is a main carbonate  
140 reservoir of the Cenomanian-Turonian (Fig. 1B). The Khasib and Tanuma formations are  
141 poor reservoirs. Tectonic fracturing of younger higher carbonate permits vertical migration of  
142 hydrocarbons into anticlines under efficient evaporitic seals. The regional evaporite seal is  
143 Gotnia Formation in the Upper Jurassic, and Fat'ha Formation in the Tertiary (Fig. 1B).

## 144 *2.2. Stratigraphy, paleogeography and mineralogy*

145 The Mishrif Formation is the main productive reservoir in southern Iraq, the United Arab  
146 Emirates, Oman, and Qatar. It was deposited in a shallow environment on the Rumaila  
147 Formation conformity. Its upper contact is unconformable with the Khasib Formation,  
148 representing a regression in the Turonian-Campanian age (Al-Mimar et al., 2018;

149 Awadeesian et al., 2019). It is represented by a unique lithostratigraphic unit regionally  
150 deposited in a fluctuating environment of shallow to deep-water reflecting the tectonic  
151 activity in the area (Alsharhan and Nairn, 1988). The carbonate rocks are composed of  
152 bioclastic particles (algae, rudist and coral reef) and represent the main facies of the Mishrif  
153 Formation. In terms of mineralogy, the Mishrif Formation is mainly composed of calcite  
154 (90% av.), with heterogeneous distribution of small amounts of dolomite, kaolinite, chlorite,  
155 authigenic quartz and clays (smectites and mixed layers) that do not exceed 10% (Al-Mimar  
156 et al., 2018). Southwardly, facies change to distal mid-ramp and proximal mid-ramp deposits  
157 and grade into outer-ramp deposits (Aqrawi et al., 1998). Eastwardly, close to the Zagros  
158 Foredeep Fault (ZFF) on the border with Iran, the Mishrif Formation is thicker (up to 400 m)  
159 and deeper (up to 3000 m) (Abbas and Mahdi, 2019; Mahdi et al., 2013). In particular, thick  
160 lagoonal units were deposited in the Majnoon field, implying a paleogeographic change in the  
161 eastern part of the study area where carbonate production caught up with the rising sea level  
162 until the filling of accommodation space with lagoonal deposits (Mahdi et al., 2013). The  
163 movement of the Hormuz Formation's salts was particularly important in southern Iraq  
164 (Murriss, 1980). Sadooni (2005) suggested that rudist build-ups in the Basrah area nucleated  
165 on the crests of growing salt structures. When the build-ups reached wave-base, they were  
166 eroded and rudist fragments were reworked, transported and dispersed to form bioclastic  
167 packstone/grainstones (Aqrawi et al., 2010).

### 3. Methodology

#### 3.1. Chemical and isotope analyses

170 Physicochemical parameters and major ion composition of five formation water samples  
171 from Rumaila South (RU287), Rumaila North (R590), West Qurna (WQ87), Majnoon  
172 (MJ20), and Zubair (ZB140) oilfields were reprised from Awadh et al. (2018) (mean values

173 and standard deviations at N = 28) and reinterpreted to investigate diagenesis and the  
174 temperature of the system using geothermometry. In this study, trace elements (total sulphur,  
175 Ba, Li, Fe, Mn, Rb, Sr) were analysed at the ALS Group Laboratory in Seville (Spain) using  
176 Inductively Coupled Plasma-Atomic Emission Spectroscopy (ICP-AES; ALS analytical code  
177 ME-ICP14L) after filtration and acidification by nitric acid. The dissolved silica as SiO<sub>2</sub>(aq)  
178 was analysed using the heteropoly blue spectrophotometric method (Clesceri et al., 1999) on  
179 filtered and diluted (1:5 by 18 MOhm ASTM Type 1 water) samples. The delta isotope  
180 values of hydrogen and oxygen of water molecules in ‰ versus V-SMOW reference standard  
181  $\delta^2\text{H}(\text{H}_2\text{O})_c$  and  $\delta^{18}\text{O}(\text{H}_2\text{O})_c$ , respectively, were obtained; where subscript ‘c’ represents the  
182 ‘composition’ scale (Horita et al., 1993). These isotope measurements were conducted by the  
183 H<sub>2</sub>-H<sub>2</sub>O and CO<sub>2</sub>-H<sub>2</sub>O gas equilibration isotope ratio mass spectrometry (IRMS) method on  
184 the vacuum-distilled samples (Boschetti et al., 2011). The salt effect parameter  $10^3\ln\Gamma$  of the  
185 brines was calculated taking into account the chemical composition and the temperature of  
186 the samples by PHREEQCI code, version 3, with the Pitzer thermodynamic database  
187 (Boschetti et al., 2011; Horita et al., 1993; Parkhurst and Appelo, 2013). According to Horita  
188 et al. (1993), the delta activity of hydrogen and oxygen,  $\delta^2\text{H}(\text{H}_2\text{O})_a$  and  $\delta^{18}\text{O}(\text{H}_2\text{O})_a$ ,  
189 respectively, was obtained summing the salt effect parameter and the delta isotope  
190 composition of hydrogen and oxygen.

191 The strontium isotope ratios,  $^{87}\text{Sr}/^{86}\text{Sr}$ , of the brines were obtained using thermal  
192 ionization mass spectrometry (TIMS). Prior to the analytical process, separation of Sr from  
193 the matrix bulk elements, and especially from Rb, was executed using heat plate evaporation  
194 with Teflon® vials at 80°C, followed by chromatographic extraction using Sr-Resin™  
195 (TrisKem International) (crown-ether (4, 4’ (5’)-di-t-butylcyclohexano-18-crown-6). The  
196 final Sr fraction was recovered from the bulk using HNO<sub>3</sub> 0.05M as eluent, then evaporated  
197 on a heat plate at 80°C and introduced into the mass spectrometer. Possible  $^{87}\text{Rb}$  interferences

198 were corrected in the Sr analysis and the  $^{87}\text{Sr}/^{86}\text{Sr}$  ratio was normalised in order to correct for  
199 mass fractionation, taking into account a reference value of  $^{86}\text{Sr}/^{88}\text{Sr} = 0.1194$ . The  $^{87}\text{Sr}/^{86}\text{Sr}$   
200 results were normalised to NBS SRM 987 (National Bureau of Standards Standard Reference  
201 Material 987 – strontium carbonate). Internal precision was  $3 \times 10^{-6}$ .

### 202 *3.2. Thermodynamic calculations*

203 PHREEQCI code and Pitzer thermodynamic dataset were also used to define:

- 204 i) the mineral-water saturation indices  $SI = \log(\text{IAP}/K)$ , where IAP and K are the ion  
205 activity product of the dissolved constituents and K is the mineral solubility product in a  
206 specific reaction, respectively, and the partial pressure of carbon dioxide by the Peng–  
207 Robinson equation of state (Parkhurst and Appelo, 2013);
- 208 ii) a geothermal model based on multimineral equilibria.

209 Results were compared to previously published chemical and isotopic  
210 geothermometers specific for sedimentary brines (Boschetti et al., 2015; Kharaka and  
211 Mariner, 1989; Sanjuan et al., 2014). The calculated activity of the dissolved constituents was  
212 also used to calculate the saturation index of a carbonate solid solution made of calcite,  
213 magnesite, rhodochrosite, siderite and strontianite by EQ3/6 code, version 8 (Wolery and  
214 Jarek, 2003).

215 The Geochemist's Workbench® code (GWB), version 7.0.6 (Bethke and Yeakel,  
216 2008), was used to calculate the evaporation path of Cretaceous seawater using the React  
217 tool, HMW thermodynamic database, and the main chemical composition of seawater during  
218 that period (Bäbel and Schreiber, 2014). According to Bäbel and Schreiber (2014), a chloride  
219 concentration of present-day seawater ( $565 \text{ mmol kg}^{-1} \text{ H}_2\text{O}$ ) was taken as a reference; then  
220 chloride concentration was charge-balanced, taking into account other main constituents and  
221  $\text{pH} = 7.5$  (Hönisch et al., 2012), and a  $\log\text{PCO}_2(\text{g}) = -3$  was settled during evaporation. This

222 latter corresponded to a mean concentration of 1000 ppmv of CO<sub>2</sub> in the Cretaceous  
223 atmosphere (Hönisch et al., 2012; Wang et al., 2014).

224 Finally, activity diagrams using a thermodynamic database of the minerals and  
225 dissolved constituents, recalculated at a pressure of 20 MPa, were plotted using the Act tool  
226 of the GWB-code (Boschetti et al., 2016). The Rxn tool of the same code was also used to  
227 check the thermodynamic equilibria of specific reactions.

#### 228 **4. Results and Discussion**

229 The physicochemical and isotope parameters are reported in Table 1. The recalculated main  
230 chemical composition in equivalents per liter of formation water from the southern region of  
231 Iraq shows a Cl-Na composition. In particular, the Na/Cl equivalent ratios range span  
232 between 0.77 and 0.91, with a mean of  $0.83 \pm 0.05$ , which is similar to that of present-day  
233 seawater (0.86). The Ca/(SO<sub>4</sub> + HCO<sub>3</sub>) equivalent ratios of the brines are largely over 1, with  
234 a mean of  $44 \pm 19$  and a range between 15 and 78. Therefore, brines can be classified also as  
235 Ca-Cl, according to Rosenthal (1997). The mean measured temperature of the water sampled  
236 in the Mishrif Formation is  $65 \pm 2$  °C (N = 28) (Awadh et al., 2018). Between the  
237 investigated trace elements, the concentration of barium and manganese are higher in  
238 Majnoon (5.43 and 4.47 mg/l, respectively) in comparison with the range of the samples from  
239 the other oilfields (1.44-1.79 and 0.10-0.13 mg/l, respectively). All samples showed  
240 supersaturation in calcite, aragonite, and dolomite (Table 2). Barite and anhydrite are also  
241 supersaturated in all but one sample (RU287). Finally, waters are in equilibrium with  
242 chalcedony and oversaturated in quartz.

##### 243 *4.1 Chemical composition: diagenesis and geothermometry*

244 According to the previous published works on southern Iraq oilfields (Awadh et al., 2019a;  
245 Awadh et al., 2018), the above described chemical ratios of Na/Cl =  $0.83 \pm 0.05$  and Ca/(SO<sub>4</sub>

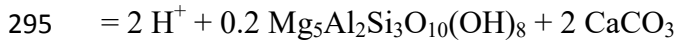
246 + HCO<sub>3</sub>) = 44 ± 19 are typical of marine origin formation waters that have undergone  
247 chemical modification due to diagenesis (Boschetti et al., 2011; Rosenthal, 1997). The  
248 Langelier–Ludwig and brine differentiation diagrams (Boschetti, 2011; Hounslow, 1995) of  
249 Figure 2 depict the distinct composition of the oilfield brines in comparison with the local  
250 shallow groundwater (Hamdan, 2017) and surface waters (Al-Mallah, 2014; ROPME, 2011;  
251 Rzóška, 1980). Surface water (Ghalib and Almallah, 2017), water produced from crude oil  
252 dehydration (Al-Shamkhani, 2013) or a mixture of both were used in the oilfields for water-  
253 flooding purposes. In Figure 2A, the brine samples from this study and literature are grouped  
254 in a narrow field, whereas in the brine differentiation plot (Figure 2B), brines are displaced  
255 between the evaporation curve of Cretaceous seawater and the produced waters from  
256 dehydrators (Al-Furaiji, 2016; Al-Shamkhani, 2013). Similarly to the Cretaceous formation  
257 brines in Venezuela (Boschetti et al., 2016), most of the studied brines affected by diagenesis  
258 show a Ca-excess and Na-deficit and seem to follow the typical Ca-Na exchange trend of the  
259 so-called basinal fluid line (Davisson and Criss, 1996) (Figure 3). Sample RU287 was  
260 probably affected by dolomitization and then by mixing with waters produced from crude  
261 dehydrators (“produced water” field in Figure 3). The hottest (115°C) water sample from the  
262 deeper Zubair sandstone indicates that the chemical effects of Ca-Na reactions (Al-Marsoumi  
263 and Abdul-Wahab, 2005), most probably due to albitisation, are more pronounced at higher  
264 temperatures (Figure 3A). Different from the Mishrif Formation, albite was found in the  
265 Zubair Formation (Al-Ziayyir, 2018). Moreover, from a theoretical point of view, the  
266 diagenetic effects could be more or less pronounced if the variability of the seawater  
267 composition in the past was considered. If Cretaceous seawater is used as a reference instead  
268 of present-day seawater, the oilfield brines are more clustered towards the axes origin of  
269 Figure 3B (which coincides with the composition of less saline surface water) or towards the  
270 “produced water” fields. The dolomitization process seems to have had a greater role in the



271 Ca-excess of the waters (Figure 3B). However, the geothermal modelling indicated in Figure  
272 4, also suggests that calcite-dolomite equilibration occurred along with chalcedony instead of  
273 quartz. In that diagram, all but one sample are clustered between 50 and 75°C isotherms, a  
274 range that includes the temperatures of  $64 \pm 5^\circ\text{C}$  (N = 9) and  $64 \pm 7^\circ\text{C}$  (N = 5) obtained by  
275 Mg-Li and chalcedony geothermometers, respectively — the latter corrected for dissolved  
276 silica activity and pressure (Kharaka and Mariner, 1989) (Table 2). The exception is  
277 represented by sample MJ20 (Majnoon oilfield), which is shifted towards the quartz-dolomite  
278 (ordered) model (Figure 4) and shows the lowest temperature from quartz and chalcedony  
279 from geothermometric equations (Table 2). Such an apparent convergence between quartz  
280 and chalcedony is probably attributable to the greater depth and pressure in the MJ20  
281 borehole (Table 1), conditions that could enhance simultaneous equilibria between the fluid  
282 and the two mineral phases (Giggenbach, 1991). For the MJ20 sample, a mean value of  
283  $70.5^\circ\text{C}$  between the geothermometric equations of quartz and chalcedony shows a good  
284 agreement with the  $68^\circ\text{C}$  obtained from the Mg-Li geothermometer (Table 2).

285 Globally, the mean inferred temperature of the brines are quite similar to the mean  
286 temperature measured at depth, confirming that the present-day borehole temperatures are not  
287 so different from those reached during Neogene burial (Abeed et al., 2013). Sample MJ20 is  
288 an exception, showing a temperature  $10^\circ\text{C}$  higher. This is probably due to the effect of  
289 greater borehole depth (Fig. 1B) and pressure. The Majnoon oilfield had the highest  
290 measured values (Table 1). Activity diagrams of Figures 5A and 5B show that Mg  
291 concentration in the brine seems to be limited by dolomite and by chlorite. To check the  
292 coexistence of the minerals, the thermodynamics of the following reaction have been  
293 calculated (Supplementary File 1):





296 At P = 20 MPa and buffering conditions of Figure 5A, except for Mg which has been  
297 buffered by clinocllore,  $\text{Mg}_5\text{Al}_2\text{Si}_3\text{O}_{10}(\text{OH})_8$ , instead of dolomite. The above reaction is in  
298 equilibria at 64°C using  $\log[\text{Ca}^{2+}/(\text{H}^+)^2] = 11.11$  and  $\log[\text{SiO}_2(\text{aq})] = -3.32$ , which  
299 corresponds to the mean activity values of all investigated samples (Supplementary File 1).  
300 Therefore, this corroborates not only that dolomite and chlorite could coexist in the studied  
301 basin, but also the temperature values obtained by geothermometers, in particular those by  
302 Li-Mg and chalcedony equations (Table 2).

303 Figure 5 also shows that the Ca/Na ratio is probably controlled by smectite instead of  
304 albite. The role of clays on the control of Na amount in solution by Ca-Na exchange or Na  
305 adsorption could also explain the lower temperatures of  $42 \pm 6$  °C obtained using the Na/Li  
306 geothermometer (Kharaka and Mariner, 1989; Sanjuan et al., 2014) (Table 2). Similarly, the  
307 values obtained from the boron isotope geothermometer gave an underestimation of the brine  
308 temperature (Table 2). This could be due to a higher  $\delta^{11}\text{B}$  value in Cretaceous seawater (up to  
309 3‰ higher than the present; Lemarchand et al. 2002), together with a fractionation effect due  
310 to evaporation up to halite saturation (approximately +4‰) (Vengosh et al. 1992). Actually,  
311 by subtracting a value of 7‰ from the original values of the brines, a mean temperature of 64  
312  $\pm 6$ °C was obtained from the boron isotope geothermometric equation (Boschetti et al.,  
313 2015), which matches with that obtained by the calcite-dolomite-chlorite-kaolinite equilibria.

#### 314 4.2. Oxygen and hydrogen stable isotope ratios

315 The isotope composition value — i.e. not considering the salt effect according to Horita et al.  
316 (1993) — of the studied formation water is similar to that of the Mishrif Formation values  
317 from the Qatar oilfield values (Danquigny et al., 2005) (Figure 6). However, the calculation  
318 of isotope activity due to the salt effect reveals a high enrichment in  $\delta^2\text{H}$  (up to +8.3‰) and a

319 slight depletion in  $\delta^{18}\text{O}$  (up to -0.3‰) in comparison to the analysed isotope composition. As  
320 presented in Figure 6, the isotope composition of the formation waters from the samples  
321 analyzed in this study fall close to the final part of the hook path derived from experimental  
322 seawater evaporation (e.g. Gonfiantini et al., 2018), thus confirming the marine origin of  
323 these samples, as previously inferred by the boron isotope (Awadh et al., 2018). It should be  
324 noted that the experimental hook paths of the evaporated seawater are generally analysed  
325 from salt pans without the addition of either new marine or meteoric water (i.e. closed  
326 system) (Gonfiantini, 1965; Gonfiantini et al., 2018). This could be the reason why the  
327 isotope activity values of the brine — i.e. considering the salt effect according to Horita et al.  
328 (1993) — do not fall on the hook path (Figure 6). In Figure 6, the Iraq meteoric water line  
329 (IMWL) and its prediction interval (parallel dashed lines with  $\delta^2\text{H} \pm 10.3$  ‰ from IMWL)  
330 were recalculated from the rainwater isotope data of Ali et al. (2015) using the error-in-  
331 variable (EIV) regression method (Boschetti et al., 2019). The extrapolation of the best fit  
332 line of the brine samples meets the prediction interval of the meteoric water line just between  
333 rain waters collected from Başrah city (Fig. 1) plus other southern Iraq areas (Al-Kinani et  
334 al., 2018; Ali et al., 2015; Jassem et al., 2018) and evaporated river samples from the Tigris  
335 and Euphrates (Jassem et al., 2018) (Figure 6). Sample RU287 shows the highest contribution  
336 of modern fresh water. It should also be remarked that, in comparison with other samples, the  
337 RU287 brine displays barite supersaturation (Table 2), which is probably due to the effect of  
338 mixing between brines and local water of meteoric origin or reinjected produced waters as a  
339 consequence of the water flooding (Ghalib and Almallah, 2017; Sorbie and Mackay, 2000).  
340 This is in line with the previously described chemical diagrams. On the opposite side, the  
341 extrapolated best fit line of the isotope activity of the brines meets the hooked evaporation  
342 path of seawater just on the top of the hump (Figure 6), which approximatively corresponds  
343 to gypsum saturation (Holser, 1979; Knauth and Beeunas, 1986).

344 Evaporated seawater samples from present-day sabkha and lagoon environments (i.e.  
1  
2 345 open systems) show  $\delta^{18}\text{O}$  up to +6.5‰, which is similar to those determined in the formation  
3  
4 346 brines of this study, but with  $\delta^2\text{H}$  enrichment up to approximately +30‰ (McKenzie et al.,  
5  
6  
7 347 1980; Nadler and Magaritz, 1980; Robinson and Gunatilaka, 1991). Lower deuterium values  
8  
9  
10 348 are mainly due to mixing with evaporated surface waters or groundwater of meteoric origin  
11  
12 349 (McKenzie et al., 1980; Robinson and Gunatilaka, 1991); whereas, flooding and mixing of  
13  
14 350 evaporated solution with new seawater inputs could shift the composition back to the starting  
15  
16  
17 351 values (i.e. near V-SMOW) (Nadler and Magaritz, 1980) (Figure 6). A similar effect was  
18  
19 352 observed in Miocene brines by comparison with  $\delta^{18}\text{O}$  from coeval gypsum, with the  
20  
21  
22 353 exception of the formation waters affected by a positive  $\delta^{18}\text{O}$ -shift as result of diagenetic  
23  
24 354 water-rock interaction with limestones (Boschetti et al., 2011). In a similar way, and  
25  
26  
27 355 assuming that starting seawater during the Phanerozoic has remained isotopically similar to  
28  
29 356 the present-day V-SMOW value (i.e. 0‰ both for oxygen and for hydrogen stable isotope  
30  
31 357 ratios) (Gregory and Taylor Jr, 1981; Ryb and Eiler, 2018; Sessions, 2016), the  $^{18}\text{O}$   
32  
33  
34 358 enrichment of formation waters as observed in samples MJ20, ZB140, and R590 could be due  
35  
36  
37 359 to water–rock interaction. Therefore, water-rock interaction and dilution seem to be the main  
38  
39 360 processes that affected in a significant manner the isotope composition of the studied brines.  
40  
41

42 361 Such a diagenetic effect was also hypothesised for the Mishrif Formation in Qatar  
43  
44 362 where limestones value ranges between  $+24.4 \text{ ‰} < \delta^{18}\text{O} \text{ (V-SMOW)} < +27.4 \text{ ‰}$ , formation  
45  
46  
47 363 brines  $\delta^{18}\text{O}$  up to +5‰ (V-SMOW), and temperatures between 50 and 70°C have been  
48  
49 364 measured (Deville de Periere, 2011). As the isotope values of the limestones from the same  
50  
51  
52 365 formation in southern Iraq are within the range of those measured in Qatar, i.e.  $+25.2 \text{ ‰} <$   
53  
54 366  $\delta^{18}\text{O} \text{ (V-SMOW)} < +27.4 \text{ ‰}$  (Taha and Abdullah, 2019), the diagenetic effect can be  
55  
56  
57 367 hypothesised also for this area. Considering a mean value  $\delta^{18}\text{O}(\text{H}_2\text{O})_a = +3.9 \text{ ‰}$  (V-SMOW)  
58  
59 368 for the brine samples that fall within the diagenetic arrow in Figure 6 and a mean value of  
60  
61  
62  
63  
64  
65

369  $\delta^{18}\text{O}$  (limestones) equal to +26.5 ‰ (V-SMOW) of the Mishrif Formation in southern Iraq, it  
370 is possible to calculate an oxygen isotope fractionation factor of  $1000\ln\alpha$  (calcite-water) =  
371 +22.3 ‰. This latter value corresponds to a temperature between 56°C (Kim and O'Neil,  
372 1997) and 69°C (Zheng, 1999). Other isotope effects due to clays and crude are probably not  
373 quantitatively important or less pronounced than the salt effect. Indeed, a fractionation  
374 between water and hydrocarbons should generate in brines a shift towards  $\delta^2\text{H}$  values higher  
375 than seawater (e.g., Horita, 2009), but this is not the case (Figure 6). Furthermore, the amount  
376 of clays minerals in the Mishrif Formation are probably insufficient to generate a significant  
377 isotope effect on the  $\delta^2\text{H}$  of the waters.

#### 378 4.3. Strontium isotope ratio

379 The strontium isotope ratios of the four brine samples analysed are  $0.707713 < {}^{87}\text{Sr}/{}^{86}\text{Sr} <$   
380  $0.707749$  (WQ87, RU287, ZB140, R590), which corresponds to a marine strontium of late  
381 Cenomanian–early Maastrichtian age (McArthur, 2010; McArthur et al., 2012); with the  
382 sample at the Majnoon oilfield (MJ20) showing the highest value of 0.708043. The Mishrif  
383 reservoir is Cenomanian–Turonian; therefore, the strontium isotope ratio should theoretically  
384 not be greater than  $0.707314 \pm 0.000005$  (McArthur, 2010; McArthur et al., 2012). The  
385 higher strontium isotope ratios in formation waters could suggest a contribution of more  
386 radiogenic strontium from injected waters when compared to the more saline and enriched  
387 brines (Danquigny et al., 2005), but in this case the oxygen and hydrogen stable isotope ratios  
388 are not less than the other samples. Moreover, it should be also noted that  ${}^{87}\text{Sr}/{}^{86}\text{Sr}$  values up  
389 to 0.707869 have been detected in the brines from the Mishrif Formation in Qatar (Al Khalij  
390 offshore field; Danquigny et al. 2005) and up to 0.70878 in the carbonate matrix of the coeval  
391 Sarvak Formation in southern Iran (Hajikazemi et al., 2012). Such elevated values detected at  
392 the disconformity surfaces of the formations are probably due to the contribution of meteoric  
393 water during diagenesis (e.g., Hajikazemi et al. 2012). However, the combination of high

394 manganese and radiogenic strontium contributions to the limestones of the Sarvak Formation  
1  
2  
3 395 of southern Iran were also attributed to different sources: i) a Cenomanian-Turonian subaerial  
4  
5 396 exposure; ii) diagenetic fluids; and iii) detritus (Navidtalab et al., 2016). Actually, all the  
6  
7 397 inspected brines of this study are undersaturated with respect to pure rhodocrosite ( $SI = -3.9 \pm$   
8  
9  
10 398  $0.8$ ), but in equilibrium with carbonate solid solution ( $SI = -0.082 \pm 0.261$ ) (Table 2). In  
11  
12 399 particular, despite its high Mn activity, the Majnoon brine MJ20 showed a slight  
13  
14 400 undersaturation in that solid solution. Therefore, the higher Mn concentration (up to 4 mg/l)  
15  
16 401 and radiogenic strontium at that brine could be acquired by limestone dissolution in a  
17  
18 402 disconformity layers. Alternatively, as suggested by the lowest gypsum and anhydrite  
19  
20 403 saturation indices of the Majnoon sample (Table 2), it cannot be excluded that there was a  
21  
22 404 contribution of radiogenic strontium-rich sulphate minerals from Cambrian salt domes (up to  
23  
24 405  $0.7092$ ) (McArthur et al., 2012). Salt domes characterise the fold settings in the oilfields of  
25  
26 406 southern Iraq (Al-Ameri et al., 2011; Al-Mimar and Awadh, 2019). The doming triggered  
27  
28 407 local uplift and emergence of paleo-exposure surfaces (Rahimpour-Bonab et al., 2013), thus  
29  
30 408 the shallow back shoal/lagoonal depositional environment of Mishrif limestones at the  
31  
32 409 Majnoon oilfield and the salt domes seem to be related (Aqrawi et al., 2010; Mahdi et al.,  
33  
34 410 2013). Moreover, “hydrothermal fluids” with temperatures up to  $80^{\circ}\text{C}$  were hypothesized to  
35  
36 411 form diagenetic cements (i.e., blocky calcite), dolomite and coarse crystalline pyrite during  
37  
38 412 deeper burial of the Sarvak Formation (Hajikazemi et al., 2017). Therefore, the chemical,  
39  
40 413 thermal and isotopic anomalies of the Majnoon brine suggest that it is the hottest fluid  
41  
42 414 probably related to the higher geothermal gradient of a deeper structure as the ZFF (Basilici  
43  
44 415 et al., 2020; Bordenave, 2008; Bordenave and Hegre, 2010).

## 54 416 **5. Conclusions**

57 417 This paper presented the first data on isotope ratios of oxygen, hydrogen, and strontium of  
58  
59 418 oilfield waters from southern Iraq, along with new trace element data and a reinterpretation of  
60

1  
2  
3  
4  
5  
6  
7  
8  
9  
10  
11  
12  
13  
14  
15  
16  
17  
18  
19  
20  
21  
22  
23  
24  
25  
26  
27  
28  
29  
30  
31  
32  
33  
34  
35  
36  
37  
38  
39  
40  
41  
42  
43  
44  
45  
46  
47  
48  
49  
50  
51  
52  
53  
54  
55  
56  
57  
58  
59  
60  
61  
62  
63  
64  
65

419 previous published chemistry. Processes like diagenesis and seawater evaporation that  
420 typically occur in these fluids can be distinguished using classical ‘basinal fluid’ chemical  
421 diagrams. Mishrif Formation waters are Cretaceous connate brines and the different chemical  
422 composition of seawater of that period needs to be taken into account for a more correct  
423 interpretation. The Ca-excess versus Na-deficit composition of these kinds of fluids are  
424 usually explained by albitisation. However, it was verified by activity plots that in the Mishrif  
425 limestone reservoir the Na/Ca exchange that occurs in brines is mainly due to water-smectite  
426 equilibrium.

427         The values  $\delta^2\text{H}$  and  $\delta^{18}\text{O}$  obtained on selected samples show that oxygen isotope  
428 composition of the brines was isotopically more affected by equilibria with limestone than  
429 evaporation. The global effect of the water-rock interaction is an  $^{18}\text{O}$ -enrichment of the  
430 brines. Locally, dilution by present-day water of meteoric origin and shift towards the local  
431 meteoric water line also detected, probably as consequence of water-flooding (Rumaila  
432 South, sample RU287). Furthermore, it is also shown that isotope data cannot be separated  
433 from the interpretation of the chemical composition of sedimentary brines. The contribution  
434 of the salt effect on the stable isotope ratios of water molecules, i.e.  $^2\text{H}/^1\text{H}$  and  $^{18}\text{O}/^{16}\text{O}$ , needs  
435 to be evaluated because this parameter could vary the results during fractionation processes  
436 such as seawater evaporation and diagenesis. Hydrogen isotope ratios are probably more  
437 affected by the salt effect than other fractionations. Furthermore, taking into account the salt  
438 effect, the temperature range inferred from carbonate-water oxygen isotope ratio fractionation  
439 is comparable to that obtained from the chemical geothermometers, i.e. between 50 and 75°C.  
440 According to Abeed et al. (2013), these evaluations confirm that the present-day borehole  
441 temperatures are not so different from those reached during Neogene burial.

442         More recent mixing processes such as water floods could be detected by a comparison  
443 with the composition of the formation brine, waters produced from crude dehydrators, and

1 444 the local waters of meteoric origin. The strontium isotope ratio confirms the interaction of  
2 445 Cretaceous limestone for most of the studied samples, suggesting a late Cenomanian–early  
3  
4 446 Maastrichtian age, and an input of more radiogenic strontium in the Majnoon oilfield (MJ20  
5  
6  
7 447 sample). The brine sample from this latter oilfield showed a particular geochemical  
8  
9  
10 448 characteristic. Despite the lower temperature measured at the MJ20 borehole (60°C), the  
11  
12 449 slightly higher temperature obtained by the Li-Mg, Na-Li and  $\delta^{11}\text{B}$  geothermometers (up to  
13  
14 450 74°C) is probably due to the deeper structure of that oilfield, which is closer to the ZFF. The  
15  
16  
17 451 more radiogenic strontium ratio at Majnoon could be related to: i) debris input in the  
18  
19 452 limestone, which could explain also the high Mn content; or ii) interaction with local  
20  
21  
22 453 Cambrian sulphates. An inspection of additional samples, sulphur stable isotope ratio  
23  
24 454 ( $^{34}\text{S}/^{32}\text{S}$ ) and radiogenic isotope of the halogens ( $^{139}\text{I}$ ,  $^{36}\text{Cl}$ ) could improve the knowledge of  
25  
26  
27 455 the past water flow events and clarify the relationship between the high Mn concentration /  
28  
29 456 high radiogenic strontium in the Cretaceous limestones and the salt domes.

## 31 457 **Acknowledgements**

32  
33  
34  
35 458 Special thanks to G. Venturelli for the comments and suggestions on a preliminary version of  
36  
37  
38 459 the manuscript. The authors very much appreciate the Associate Editor, B.J. Katz, and the  
39  
40 460 two anonymous reviewers for their careful reading of the manuscript and all valuable  
41  
42  
43 461 constructive comments and suggestions.

## 44 45 462 **Captions**

46  
47  
48 463 **Table 1** – Physicochemical parameters, major ion composition, trace elements concentration,  
49 464 and isotopic results from Awadh et al. (2018) and this study.

50  
51 465 **Table 2** – Geothermometric results in Celsius degree (°C); mineral saturation indices (SI),  
52 466 and carbon dioxide partial pressure as  $\log\text{P}(\text{CO}_2)\text{g}$  obtained by PHREECI code, version 3,  
53 467 along with Pitzer thermodynamic dataset at the measured temperature and water pressure  
54 468 conditions (Table 1). EQ 3/6 code was also used to calculate the saturation indexes of  
55 469 carbonates solid solution.

56  
57  
58 470 **Figure 1** – A) Location map showing the studied oilfields at the Zubair zone, within the  
59 471 southern part of the Mesopotamia plain and to the southwest of the Zagros Foredeep Fault  
60 472 (ZFF); Stratigraphic correlation of the five oilfield wells penetrating four formations



473 (Rumaila, Mishrif, Khasib, and Tanuma) in which there is a well from each oilfield (RU287  
474 from Rumaila South, R590 from Rumaila North, WQ87 from West Qurna, MJ20 from  
475 Majnoon, and ZB140 from Zubair oilfield); B) Typical section represents the stratigraphic  
476 setting in the study area.

477 **Figure 2** – Langelier–Ludwig (A) and Brine Differentiation Plot (B) of the oilfield brines of  
478 southern Iraq (Al-Mallah, 2014; Al-Marsoumi and Abdul-Wahab, 2005; Awadh et al., 2019b;  
479 Awadh et al., 2018; Jamil, 1978) compared with shallow groundwater (Hamdan, 2017), Shatt  
480 Al-Arab River (ROPME, 2011), Shatt Al-Basrah Canal, or ‘Main Drain’ (Al-Mallah, 2014)  
481 and seawater. In both diagrams, concentration of the dissolved species are in equivalent/liter;  
482 dashed ellipses depict the trend of the Tigris–Euphrates River system at Qurna and Shatt Al-  
483 Arab River during the 60s (Rzóska, 1980). In (B), Mishrif Formation’s brine waters from  
484 Awadh et al. (2018) are distinguished by black triangles; the five samples reprised in this  
485 study are highlighted by white crosses. The brine data from other references (Al-Mallah,  
486 2014; Al-Marsoumi and Abdul-Wahab, 2005; Awadh et al., 2019b; Jamil, 1978) are  
487 represented by white triangles. Produced waters from hydrocarbon dehydrators are also  
488 shown for comparison (dashed field) (Al-Furaiji, 2016; Al-Shamkhani, 2013). Arrows depict  
489 possible mixing trends. In the inset, the original fields of the diagram along with evaporation  
490 paths of present-day (Boschetti, 2011; Hounslow, 1995) and Cretaceous seawater (this study)  
491 are shown. G and H depict the gypsum and halite saturation points, respectively.

492 **Figure 3** –  $\text{Ca-excess} = 2 \times [\text{Ca}_{\text{meas}} - (\text{Ca}/\text{Cl})_{\text{SW}} \times \text{Cl}_{\text{meas}}]/40.08$  vs.  $\text{Na-deficit} = [(\text{Na}/\text{Cl})_{\text{SW}} \times$   
493  $\text{Cl}_{\text{meas}} - \text{Na}_{\text{meas}}] / 22.99$  diagram for oilfield waters from southern Iraq, where meas =  
494 measured, SW = seawater and Ca, Na and Cl are elemental concentrations in mg/l (Davisson  
495 and Criss, 1996). The 1Ca-2Na or 1Ca-1Na exchange arrows depict the possible paths of  
496 formation fluids in sedimentary basins during plagioclase albitisation (Davisson and Criss,  
497 1996). In (A) and (B) diagrams, present-day and Cretaceous seawater were used as SW-  
498 composition, respectively. In both: light gray ellipse at the origin of the plot represents the  
499 initial seawater composition (i.e. before evaporation), local groundwater and surface waters  
500 composition; dashed and dot-dashed lines depict the evaporation paths of Cretaceous and  
501 present-day seawaters, respectively. Other symbols and fields as in Figure 2.

502 **Figure 4** – Base-10 logarithm of silicium versus calcium/magnesium ratio diagram of the  
503 Mishrif Formation’s brines from southern Iraq (molar concentration). Dashed curves depict  
504 the simultaneous equilibria of calcite-dolomites plus quartz (light gray) or chacedony (black)  
505 calculated by PHREEQCI code and pitzer thermodynamic dataset (Parkhurst and Appelo,  
506 2013) at the mean pressure of the five samples (27.8 MPa; Table 1).

507 **Figure 5** – Activity plots for the system  $\text{Na}_2\text{O}-\text{CaO}-\text{MgO}-\text{Al}_2\text{O}_3-\text{SiO}_2-\text{H}_2\text{O}-\text{CO}_2$  at  $P = 200$   
508 bar and  $50 < T < 75$  °C. In (A), the activity of dissolved silica has been fixed at the mean  
509 value detected in the waters, i.e.:  $\log[\text{SiO}_2(\text{aq})] = -3.32$ , whereas in (B) it was buffered by  
510 chalcedony. In both diagrams: water activity at  $\log[\text{H}_2\text{O}] = -0.0855$  (mean value of the local  
511 brines); aluminium buffered by kaolinite; magnesium and  $\text{HCO}_3^-$  buffered by dolomite and  
512 calcite, respectively.

513 **Figure 6** –  $\delta^2\text{H}(\text{H}_2\text{O})$  vs.  $\delta^{18}\text{O}(\text{H}_2\text{O})$  diagram. Samples from this study are differentiated for  
514 isotope composition (white-crossed gray triangles) and isotope activity (white-crossed black  
515 triangles): the former represent analytical results of water samples after vacuum distillation  
516 and IRMS; the latter represent isotope composition plus the theoretical salt effect (Horita et  
517 al., 1993) (Table 1). Water isotope composition of brines from the Mishrif Formation in  
518 Qatar are also shown for comparison (open triangles) (Danquigny et al., 2005). Dotted lines  
519 depict the linear best fits of the two ways of representation of isotope ratios in brines.

520 Evaporated seawaters from a closed (Gonfiantini et al., 2018) and open (McKenzie et al.,  
1 521 1980; Nadler and Magaritz, 1980; Robinson and Gunatilaka, 1991) system are shown for  
2 522 comparison. The previous published data on isotope composition of the Arabian Gulf  
3 523 seawater and its evaporated composition are depicted by the field with waves and forward-  
4 524 back curved arrows, respectively (Bagheri et al., 2014; McKenzie et al., 1980; Robinson and  
5 525 Gunatilaka, 1991; Yurtsever, 1994). Rainwater samples (drops) from southern Iraq (Al-  
6 526 Kinani et al., 2018; Ali et al., 2015; Jassem et al., 2018) and northern Kuwait (Hadi et al.,  
7 527 2016) are also shown for comparison. Tigris and Euphrates samples are represented by open  
8 528 squares; samples out of the IMWL's (Iraq meteoric water line) prediction interval are  
9 529 evaporated surface water samples (arrow with slope  $\sim 4.3$ ) (Ali et al., 2015; Jassem et al.,  
10 530 2018).

11 531 **Supplementary File 1** - Calculation of the thermodynamic equilibria by Rxn tool of The  
12 532 Geochemist's Workbench® code (Bethke and Yeakel, 2008) and  $P = 20$  MPa thermodynamic  
13 533 dataset (Boschetti et al., 2016). To reduce the variables, the activity of calcium and hydrogen  
14 534 was rewritten as log-ratio in the reaction and automatically rebalanced by the tool.

## 15 535

## 16 536 **References**

17 537

18 538 Abbas, L.K., Mahdi, T.A., 2019. Reservoir units of Mishrif Formation in Majnoon Oil field,  
19 539 Southern Iraq. *Iraqi Journal of Science* 60, 2656-2663.

20 540 Abeed, Q., Leythaeuser, D., Littke, R., 2012. Geochemistry, origin and correlation of crude  
21 541 oils in Lower Cretaceous sedimentary sequences of the southern Mesopotamian Basin,  
22 542 southern Iraq. *Organic Geochemistry* 46, 113-126.

23 543 Abeed, Q., Littke, R., Strozyk, F., Uffmann, A.K., 2013. The Upper Jurassic–Cretaceous  
24 544 petroleum system of southern Iraq: A 3-D basin modelling study. *GeoArabia* 18, 179-200.

25 545 Al-Ameri, T.K., Jafar, M.S., Pitman, J., 2011. Hydrocarbon generation modeling of the  
26 546 Basrah oil fields, Southern Iraq. University of Baghdad, Jadiriya, AAPG Annual  
27 547 Convention and Exhibition. AAPG Search and Discovery, Houston, Texas.

28 548 Al-Furaiji, M., 2016. Hyper-saline produced water treatment for beneficial use. University of  
29 549 Twente, Gildeprint - The Netherlands.

30 550 Al-Kinani, S.A.A., Falih, A.H., Al-abidin, H.A.Z., Al-Naseri, S.K.A.A.H., 2018.  
31 551 Determination of the Meteoric Water Line Using Stable Isotopes in Precipitations at Several  
32 552 Locations In Baghdad. *Iraqi Journal of Science and Technology* 4, 36-42.

33 553 Al-Mallah, I.A., 2014. Assessment of the Environmental, Hydrological and Hydrogeological  
34 554 changes of the Main Drain, Iraq, College of Science - Department of Geology. University of  
35 555 Basrah, Basrah, Iraq.

36 556 Al-Marsoumi, A.M.H., Abdul-Wahab, D.S., 2005. Hydrogeochemistry of Yamama Reservoir  
37 557 formation water - west Qurna oil field - Southern Iraq. *Basrah Journal of Science* 23, 10-20.

558 Al-Mimar, H.S., Awadh, S.M., 2019. The Role of Chemistry of the Oil-Field Water in the  
1 559 Distribution of Reservoir Pressures: A Case Study of Mishrif Reservoir in the Southern Oil-  
2 560 Fields, Iraq. *Journal of Petroleum Research & Studies* 22, E52-E64.  
3  
4 561 Al-Mimar, H.S., Awadh, S.M., Al-Yaseri, A.A., Yaseen, Z.M., 2018. Sedimentary units-  
5 562 layering system and depositional model of the carbonate Mishrif reservoir in Rumaila  
6  
7 563 oilfield, Southern Iraq. *Modeling Earth Systems and Environment* 4, 1449-1465.  
8  
9 564 Al-Shamkhani, M.T., 2013. *Managing, Controlling and Improving the Treatment of Produced*  
10  
11 565 *Water Using the Six Sigma Methodology for the Iraqi Oil Fields*, College of Engineering and  
12  
13 566 *Computer Science - Department of Industrial Engineering and Management Systems.*  
14  
15 567 *University of Central Florida, Orlando, Florida.*  
16  
17 568 Al-Ziayyir, H.G.F., 2018. *Mineralisation-Related Flow Heterogeneity within the Zubair*  
18  
19 569 *Formation in the Rumaila Oilfield, Southern Iraq*, Faculty of Science and Engineering.  
20  
21 570 *University of Manchester, Manchester.*  
22  
23 571 Ali, K.K., Al-Kubaisi, Q.Y., Al-Paruany, K.B., 2015. Isotopic study of water resources in a  
24  
25 572 semi-arid region, western Iraq. *Environmental Earth Sciences* 74, 1671-1686.  
26  
27 573 Alsharhan, A.S., Nairn, A.E.M., 1988. A review of the Cretaceous Formations in the Arabian  
28  
29 574 Peninsula and Gulf: Part II. Mid-Cretaceous (Wasia Group) Stratigraphy and Paleogeography.  
30  
31 575 *Journal of Petroleum Geology* 11, 89-112.  
32  
33 576 Alyasi, A.I., Al-Jawad, S.N., Alshabender, L.Y., 2014. Geophysical Study to the Role of Salt  
34  
35 577 in Creating Buzurgan Oilfield Structure, Southeast of Iraq. *Iraqi Journal of Science* 55, 1579-  
36  
37 578 1587.  
38  
39 579 Aqrabi, A.A.M., Horbury, A.D., Sadooni, F.N., Goff, J.C., 2010. *The Petroleum Geology of*  
40  
41 580 *Iraq.* Scientific Press, Beaconsfield, Bucks, UK.  
42  
43 581 Aqrabi, A.A.M., Thehni, G.A., Sherwani, G.H., Kareem, B.M.A., 1998. Mid-Cretaceous  
44  
45 582 rudist-bearing carbonates of the Mishrif Formation: an important reservoir sequence in the  
46  
47 583 Mesopotamian Basin, Iraq. *Journal of Petroleum Geology* 21, 57-82.  
48  
49 584 Awadeesian, A.M., Awadh, S.M., Al-Dabbas, M.A., Al-Maliki, M.M., Al-Jawad, S.N.,  
50  
51 585 Hussein, A.K.S., 2019. A modified water injection technique to improve oil recovery: Mishrif  
52  
53 586 carbonate reservoirs in Southern Iraq oil fields, case study. *Iraqi Geological Journal* 52, 125-  
54  
55 587 146.  
56  
57 588 Awadh, S., Al-Mimar, H., Al-yaseri, A., 2019a. Potentiometric Salinity Mapping of Mishrif  
58  
59 589 Oilfield Waters in (Iraq's) Southern Oil Fields, in: Chaminé, H.I., Barbieri, M., Kisi, O.,  
60  
61 590 Chen, M., Merkel, B.D. (Eds.), *Advances in Sustainable and Environmental Hydrology,*  
62  
63 591 *Hydrogeology, Hydrochemistry and Water Resources - Proceedings of the 1st Springer*

592 Conference of the Arabian Journal of Geosciences (CAJG-1), Tunisia 2018. Springer Nature,  
1 Switzerland, pp. 49-52.  
2  
3  
4 594 Awadh, S.M., Al-Auweidy, M.R., Al-Yaseri, A.A., 2019b. Hydrochemistry as a tool for  
5 interpreting brine origin and chemical equilibrium in oilfields: Zubair reservoir southern Iraq  
6  
7 596 case study. Applied Water Science, 93.  
8  
9 597 Awadh, S.M., Al-Mimar, H.S., Al-Yaseri, A.A., 2018. Salinity mapping model and brine  
10 chemistry of Mishrif reservoir in Basrah oilfields, Southern Iraq. Arabian Journal of  
11 598 Geosciences 11.  
12  
13  
14 600 Babel, M., Schreiber, B.C., 2014. Geochemistry of Evaporites and Evolution of Seawater in:  
15  
16 601 Holland, H.D., Turekian, K.K. (Eds.), Treatise on Geochemistry, 2nd ed. Elsevier, Printed  
17  
18 602 and bound in Italy, pp. 483-560.  
19  
20 603 Bagheri, R., Nadri, A., Raeisi, E., Eggenkamp, H.G.M., Kazemi, G.A., Montaseri, A., 2014.  
21  
22 604 Hydrochemical and isotopic ( $\delta^{18}\text{O}$ ,  $\delta^2\text{H}$ ,  $^{87}\text{Sr}/^{86}\text{Sr}$ ,  $\delta^{37}\text{Cl}$  and  $\delta^{81}\text{Br}$ ) evidence for the origin of  
23  
24 605 saline formation water in a gas reservoir. Chemical Geology 384, 62-75.  
25  
26 606 Basilici, M., Mazzoli, S., Megna, A., Santini, S., Tavani, S., 2020. 3-D Geothermal Model of  
27  
28 607 the Lurestan Sector of the Zagros Thrust Belt, Iran. Energies 13.  
29  
30 608 Bethke, C.M., Yeakel, S., 2008. The Geochemist's Workbench® - Release 7. GWB  
31  
32 609 Essentials Guide, Hydrogeology Program. University of Illinois.  
33  
34 610 Bordenave, M.L., 2008. The origin of the Permo-Triassic gas accumulations in the Iranian  
35  
36 611 Zagros foldbelt and contiguous offshore areas: a review of the Palaeozoic petroleum system.  
37  
38 612 Journal of Petroleum Geology 31, 3-42.  
39  
40 613 Bordenave, M.L., Hegre, J.A., 2010. Current distribution of oil and gas fields in the Zagros  
41  
42 614 Fold Belt of Iran and contiguous offshore as the result of the petroleum systems, in: Leturmy,  
43  
44 615 P., Robin, C. (Eds.), Tectonic and Stratigraphic Evolution of Zagros and Makran during the  
45  
46 616 Mesozoic–Cenozoic. The Geological Society of London, London, pp. 291-353.  
47  
48 617 Boschetti, T., 2011. Application of brine differentiation and Langelier–Ludwig plots to fresh-  
49  
50 618 to-brine waters from sedimentary basins: Diagnostic potentials and limits. Journal of  
51  
52 619 Geochemical Exploration, 108, 126-130.  
53  
54 620 Boschetti, T., Angulo, B., Cabrera, F., Vásquez, J., Montero, R.L., 2016. Hydrogeochemical  
55  
56 621 characterization of oilfield waters from southeast Maracaibo Basin (Venezuela): Diagenetic  
57  
58 622 effects on chemical and isotopic composition. Marine and Petroleum Geology 73, 228-248.  
59  
60 623 Boschetti, T., Cifuentes, J., Iacumin, P., Selmo, E., 2019. Local Meteoric Water Line of  
61  
62 624 Northern Chile (18°S - 30°S): An application of error-in-variables regression to the oxygen  
63  
64 625 and hydrogen stable isotope ratio of precipitation. Water 11  
65

626 Boschetti, T., Toscani, L., Salvioli Mariani, E., 2015. Boron isotope geochemistry of  
627 Na- bicarbonate, Na- chloride, and Ca- chloride waters from the Northern Apennine  
628 Foredeep basin: other pieces of the sedimentary basin puzzle. *Geofluids* 15, 546-562.

629 Boschetti, T., Toscani, L., Shouakar-Stash, O., Iacumin, P., Venturelli, G., Mucchino, C.,  
630 Frappe, S.K., 2011. Salt waters of the Northern Apennine Foredeep Basin (Italy): origin and  
631 evolution. *Aquatic Geochemistry* 17, 71-108.

632 Clesceri, L.S., Greenberg, A.E., Eaton, A.D., 1999. Method 4500-SiO<sub>2</sub> D, Heteropoly Blue  
633 Method, Standard methods for the examination of water and wastewater, 20th. American  
634 Public Health Association, American Water Works Association, Water Environment  
635 Federation, Washington.

636 Danquigny, J.A., Matthews, J., Noman, R., Mohsen, A., 2005. Assessment of interwell  
637 communication in the carbonate Al Khalij oil field using isotope ratio water sample analysis,  
638 International Petroleum Technology Conference. IPTC, Doha, Qatar

639 Davison, M.L., Criss, R.E., 1996. Na-Ca-Cl relations in basinal fluids. *Geochimica et*  
640 *Cosmochimica Acta* 60, 2743-2752.

641 Deville de Periere, M., 2011. Origine sédimento-diagénétique de réservoirs carbonatés  
642 microporeux: exemple de la formation Mishrif (Cénomanién) du Moyen-Orient. Université  
643 de Bourgogne.

644 Ghalib, H.B., Almallah, I.A.R., 2017. Scaling simulation resulting from mixing predicted  
645 model between Mishrif formation water and different waters injection in Basrah oil field,  
646 southern Iraq. *Modeling Earth Systems and Environment* 3, 1557-1569.

647 Giggenbach, W.F., 1991. Chemical Techniques in geothermal exploration, in: D'Amore, F.  
648 (Ed.), *Application of Geochemistry in Geothermal Reservoir Development*. UNITAR, Rome,  
649 Italy, pp. 119–144.

650 Gonfiantini, R., 1965. Effetti isotopi nell'evaporazione di acque salate. *Atti della Società*  
651 *Toscana di Scienze Naturali - Memorie, Serie A* 72, 1-22.

652 Gonfiantini, R., Wassenaar, L.I., Araguas-Araguas, L., Aggarwal, P.K., 2018. A unified  
653 Craig-Gordon isotope model of stable hydrogen and oxygen isotope fractionation during  
654 fresh or saltwater evaporation. *Geochimica et Cosmochimica Acta* 235, 224-236.

655 Grabowski Jr., G.J., 2014. Iraq, in: Marlow, L., Kendall, M.C., Yose, L.A. (Eds.), *Petroleum*  
656 *systems of the Tethyan region*. The American Association of Petroleum Geologists, Tulsa,  
657 OK U.S.A., pp. 379–467.

658 Gregory, R.T., Taylor Jr, H.P., 1981. An oxygen isotope profile in a section of Cretaceous  
659 oceanic crust, Samail Ophiolite, Oman: Evidence for  $\delta^{18}\text{O}$  buffering of the oceans by deep (>

660 5 km) seawater- hydrothermal circulation at mid- ocean ridges. *Journal of Geophysical*  
661 *Research: Solid Earth* 86, 2737-2755.

662 Hadi, K., Kumar, U.S., Al-Senafy, M., Bhandary, H., 2016. Environmental isotope  
663 systematics of the groundwater system of southern Kuwait. *Environmental Earth Sciences* 75.  
664 Hajikazemi, E., Al-Aasm, I.S., Coniglio, M., 2017. Diagenetic history and reservoir  
665 properties of the Cenomanian-Turonian carbonates in southwestern Iran and the Persian Gulf.  
666 *Marine and Petroleum Geology* 88, 845-857.

667 Hajikazemi, E., Al- Aasm, I.S., Coniglio, M., 2012. Chemostratigraphy of Cenomanian–  
668 Turonian carbonates of the Sarvak Formation, southern Iran. *Journal of Petroleum Geology*  
669 35, 187-205.

670 Hamdan, A.N.A., 2017. The use of water quality index to evaluate groundwater quality in  
671 west of Basrah wells. *Kufa Journal of Engineering* 8, 51-64.

672 Holser, W., 1979. Trace elements and isotopes in evaporites, in: Burns, R.G. (Ed.), *Marine*  
673 *Minerals*. De Gruyter - Mineralogical Society of America, Berlin, Boston, pp. 295–346.

674 Hönisch, B., Ridgwell, A., Schmidt, D.N., Thomas, E., Gibbs, S.J., Sluijs, A., Zeebe, R.,  
675 Kump, L., Martindale, R.C., Greene, S.E., Kiessling, W., Ries, J., Zachos, J.C., Royer, D.L.,  
676 Barker, S., Marchitto Jr., T.M., Moyer, R., Pelejero, C., Ziveri, P., Foster, G.L., Williams, B.,  
677 2012. The geological record of ocean acidification. *Science* 335, 1058-1063.

678 Horita, J., 2009. Isotopic evolution of saline lakes in the low-latitude and polar regions.  
679 *Aquatic Geochemistry* 15, 43-69.

680 Horita, J., Cole, D.R., Wesolowski, D.J., 1993. The activity-composition relationship of  
681 oxygen and hydrogen isotopes in aqueous salt solutions: II. Vapor-liquid water equilibration  
682 of mixed salt solutions from 50 to 100 C and geochemical implications. *Geochimica et*  
683 *Cosmochimica Acta* 57, 4703-4711.

684 Hounslow, A.W., 1995. *Water Quality Data Analysis and Interpretation*. Lewis Publishers,  
685 Boca Raton, New York.

686 Jamil, A.K., 1978. Hydrochemical and Hydrodynamic Zones and the Probable Direction of  
687 Water Flow within Zubair Reservoir of Zubair and Rumaila Oil Fields (Southern Iraq).  
688 *Geologisches Jahrbuch, Reihe D, D25*, 199-211.

689 Jassem, A.A., Nada, K.B., Abdualamer, Z.S., 2018. Using  $^{18}\text{O}$ ,  $^2\text{H}$  isotopes to study the effect  
690 of fish lake on surface water in Al-Azezeya, Kut Governorate, Iraq. *The Iraqi Geological*  
691 *Journal* 51, 149-156.

692 Jassim, S.Z., Buday, T., 2006. Units of the Stable Shelf, in: Jassim, S.Z., Goff, J.C. (Eds.),  
693 *Geology of Iraq*. Dolin, Prague and Moravian Museum, Brno. Czech Republic, pp. 53-72.

694 Kharaka, Y.K., Mariner, R.H., 1989. Chemical geothermometers and their application to  
1 695 formation waters from sedimentary basins, in: Naeser, N.D., McCollin, T.H. (Eds.), Thermal  
2 696 history of sedimentary basins. Springer-Verlag, New York, pp. 99–117.  
3  
4 697 Kim, S.T., O'Neil, J.R., 1997. Equilibrium and nonequilibrium oxygen isotope effects in  
5 698 synthetic carbonates. *61 Geochimica et cosmochimica acta*, 3461-3475.  
6  
7 699 Knauth, L.P., Beeunas, M.A., 1986. Isotope geochemistry of fluid inclusions in Permian  
8 700 halite with implications for the isotopic history of ocean water and the origin of saline  
9 701 formation waters. *Geochimica et Cosmochimica Acta* 50, 419-433.  
10  
11 702 Konyuhov, A.I., Maleki, B., 2006. The Persian Gulf Basin: Geological history, sedimentary  
12 703 formations, and petroleum potential. *Lithology and Mineral Resources* 41, 344–361  
13  
14 704 Lemarchand, D., Gaillardet, J., Lewin, E., Allegre, C.J., 2002. Boron isotope systematics in  
15 705 large rivers: implications for the marine boron budget and paleo-pH reconstruction over the  
16 706 Cenozoic. *Chemical Geology* 190, 123-140.  
17  
18 707 Lowenstein, T.K., Hardie, L.A., Timofeeff, M.N., Demicco, R.V., 2003. Secular variation in  
19 708 seawater chemistry and the origin of calcium chloride basinal brines. *Geology* 31, 857-860.  
20  
21 709 Mahdi, T.A., Aqrawi, A.A., Horbury, A.D., Sherwani, G.H., 2013. Sedimentological  
22 710 characterization of the mid-Cretaceous Mishrif reservoir in southern Mesopotamian Basin,  
23 711 Iraq. *GeoArabia* 18, 139-174.  
24  
25 712 McArthur, J.M., 2010. Strontium isotope stratigraphy, in: Ratcliffe, K.T., Zaitlin, B.A. (Eds.),  
26 713 Application of modern stratigraphic techniques: theory and case histories. SEPM Society for  
27 714 Sedimentary Geology, Tulsa, Oklahoma, pp. 129–142.  
28  
29 715 McArthur, J.M., Howarth, R.J., Shields, G.A., 2012. Strontium isotope stratigraphy, in:  
30 716 Gradstein, F.M., Ogg, J.G., Schmitz, M.D., Ogg, G.M. (Eds.), *The geologic time scale 2012*.  
31 717 Elsevier, Oxford, pp. 127–144.  
32  
33 718 McKenzie, J.A., Hsü, K.J., Schneider, J.F., 1980. Movement of subsurface waters under the  
34 719 sabkha Abu Dhabi, UAE, and its relation to evaporative dolomite genesis, in: Zenger, D.H.,  
35 720 Dunham, J.B., Ethington, R.L. (Eds.), *Concepts and Models of Dolomitization*. SEPM  
36 721 Society for Sedimentary Geology, Tulsa, Oklahoma, USA, pp. 11-30.  
37  
38 722 Mortazavi, M., Heuss-Assbichler, S., Shahri, M., 2017. Hydrothermal systems in the salt  
39 723 domes of south Iran. *Procedia Earth and Planetary Science* 17, 913-916.  
40  
41 724 Murriss, R.J., 1980. Middle East: stratigraphic evolution and oil habitat. *AAPG Bulletin* 64,  
42 725 597-618.  
43  
44  
45  
46  
47  
48  
49  
50  
51  
52  
53  
54  
55  
56  
57  
58  
59  
60  
61  
62  
63  
64  
65

726 Nadler, A., Magaritz, M., 1980. Studies of marine solution basins isotopic and compositional  
727 changes during evaporation, in: Nissebaum, A. (Ed.), *Hypersaline Brines and Evaporitic*  
728 *Environments*. Elsevier, Amsterdam, The Netherlands, pp. 115-129.

729 Navidtalab, A., Rahimpour-Bonab, H., Huck, S., Heimhofer, U., 2016. Elemental  
730 geochemistry and strontium-isotope stratigraphy of Cenomanian to Santonian neritic  
731 carbonates in the Zagros Basin, Iran. *Sedimentary Geology* 346, 35-48.

732 Parkhurst, D.L., Appelo, C.A.J., 2013. Description of input and examples for PHREEQC  
733 version 3: a computer program for speciation, batch-reaction, one-dimensional transport, and  
734 inverse geochemical calculations *Techniques and Methods*. US Geological Survey, Reston,  
735 VA, p. This report is Chapter 43 of Section A: Groundwater in Book 46 *Modeling*  
736 *Techniques*.

737 Rahimpour- Bonab, H., Mehrabi, H., Navidtalab, A., Omidvar, M., Enayati- Bidgoli, A.H.,  
738 Sonei, R., Sajjadi, F., Amiri-Bakhtyar, H., Arzani, N., Izadi- Mazidi, E., 2013.  
739 Palaeo- exposure surfaces in Cenomanian–santonian carbonate reservoirs in the Dezful  
740 embayment, SW Iran. *Journal of Petroleum Geology* 36, 335-362.

741 Robinson, B.W., Gunatilaka, A., 1991. Stable isotope studies and the hydrological regime of  
742 sabkhas in southern Kuwait, Arabian Gulf. *Sedimentary Geology* 73, 141-159.

743 ROPME, 2011. The Marshes-Shatt al-Arab- Gulf System, in: *Environment, R.O.f.t.P.o.t.M.*  
744 (Ed.). Marine Science Centre – University of Basra in Cooperation with Ministry of  
745 Environment Iraq, p. 102.

746 Rosenthal, E., 1997. Thermomineral waters of Ca-chloride composition: review of  
747 diagnostics and of brine evolution. *Environmental Geology* 32, 245-250.

748 Ryb, U., Eiler, J.M., 2018. Oxygen isotope composition of the Phanerozoic ocean and a  
749 possible solution to the dolomite problem. *Proceedings of the National Academy of Sciences*  
750 115, 6602-6607.

751 Rzóśka, J., 1980. *Euphrates and Tigris, Mesopotamian ecology and destiny*. Dr. W. Junk by  
752 Publishers, The Hague The Netherlands.

753 Sadooni, F.N., 2005. The nature and origin of Upper Cretaceous basin-margin rudist buildups  
754 of the Mesopotamian Basin, southern Iraq, with consideration of possible hydrocarbon  
755 stratigraphic entrapment. *Cretaceous Research* 26, 213-224.

756 Sadooni, F.N., Aqrawi, A.A.M., 2000. Cretaceous sequence stratigraphic and petroleum  
757 potential of the Mesopotamian basin, Iraq, in: Alsharhan, A.S., Scott, R.W. (Eds.), *Middle*  
758 *East Models of Jurassic/Cretaceous Carbonate Systems*. SEPM Society for Sedimentary  
759 Geology, Tulsa, Oklahoma, USA, pp. 315-334.



760 Sanjuan, B., Millot, R., Asmundsson, R., Brach, M., Giroud, N., 2014. Use of two new Na/Li  
1 761 geothermometric relationships for geothermal fluids in volcanic environments. *Chemical*  
2 762 *Geology* 389, 60-81.  
3  
4  
5 763 Sessions, A.L., 2016. Factors controlling the deuterium contents of sedimentary  
6 764 hydrocarbons. *Organic Geochemistry* 96, 43–64.  
7  
8  
9 765 Singh, P., 2012. New Insights to the Implications of Salt Tectonics in the Northern Part of  
10 766 Kuwait Arch: An Integrated Modeling Study, First EAGE Workshop on Iraq-Hydrocarbon  
11 767 Exploration and Field Development. European Association of Geoscientists & Engineers  
12 768 (EAGE), Istanbul, Turkey  
13  
14  
15  
16 769 Sissakian, V., Abdul Ahad, A., Al-Ansari, N., Knutsson, S., 2017. Geomorphology, Geology  
17 770 and Tectonics of Jabal Sanam, Southern Iraq. *Journal of Earth Sciences and Geotechnical*  
18 771 *Engineering* 7, 97-113.  
19  
20  
21  
22 772 Sorbie, K.S., Mackay, E.J., 2000. Mixing of injected, connate and aquifer brines in  
23 773 waterflooding and its relevance to oilfield scaling. *Journal of Petroleum Science and*  
24 774 *Engineering*. 27, 85-106.  
25  
26  
27 775 Taha, T.M., Abdullah, E.J., 2019. Reconstruction of Paleo depth and Paleo temperature from  
28 776 C-O stable isotope records of Mishrif Formation, southern Iraq. *Iraqi Journal of Science* 60,  
29 777 1730-1742.  
30  
31  
32  
33 778 Vengosh, A., Starinsky, A., Kolodny, Y., Chivas, A.R., Raab, M., 1992. Boron isotope  
34 779 variations during fractional evaporation of sea water: new constraints on the marine vs.  
35 780 nonmarine debate. *Geology* 20, 799–802.  
36  
37  
38 781 Wang, Y., Huang, C., Sun, B., Quan, C., Wu, J., Lin, Z., 2014. Paleo-CO<sub>2</sub> variation trends  
39 782 and the Cretaceous greenhouse climate. *Earth-Science Reviews* 129, 136-147.  
40  
41  
42 783 Wolery, T.W., Jarek, R.L., 2003. EQ3/6, version 8.0—software user’s manual. Civilian  
43 784 radioactive waste management system, Management & Operating Contractor, Sandia  
44 785 National Laboratories, Albuquerque, New Mexico.  
45  
46  
47 786 Yurtsever, Y., 1994. Role of environmental isotopes in studies related to salinization  
48 787 processes and salt water intrusion dynamics, 13th Salt Water Intrusion Meeting - Session 3:  
49 788 Hydrogeochemical and environmental isotope studies. Mixing zone. Characterization of the  
50 789 origin and dynamics of salt and brackish waters, Cagliari, Italy, pp. 5-10.  
51  
52  
53  
54 790 Zheng, Y.-F., 1999. Oxygen isotope fractionation in carbonate and sulfate minerals.  
55 791 *Geochemical Journal* 33, 109-126.  
56  
57  
58 792  
59  
60  
61  
62  
63  
64  
65

1           **Chemical and isotope composition of the oilfield brines from Mishrif**

2           **Formation (southern Iraq): Diagenesis and geothermometry**

3           Tiziano Boschetti<sup>1</sup>, Salih Muhammad Awadh<sup>2</sup>, Heba Sadoon Al-Mimar<sup>2</sup>, Paola Iacumin<sup>1</sup>,

4           Lorenzo Toscani<sup>1</sup>, Enricomaria Selmo<sup>1</sup>, Zaher Mundher Yaseen<sup>3,\*</sup>

5           <sup>1</sup> Department of Chemistry, Life Sciences and Environmental Sustainability, University of

6           Parma, Parco Area delle Scienze 157/A, 43124 Parma, Italy

7           <sup>2</sup> Department of Geology, College of Science, University of Baghdad, Baghdad, Iraq

8           <sup>3</sup> Sustainable Developments in Civil Engineering Research Group, Faculty of Civil

9           Engineering, Ton Duc Thang University, Ho Chi Minh City, Vietnam

10           \*Corresponding authors: Zaher Mundher Yaseen

11           Email: [yaseen@tdtu.edu.vn](mailto:yaseen@tdtu.edu.vn)

## 26 Abstract

27 This paper focuses on the geochemical composition and isotope geochemistry of brines in the  
28 Cenomanian–Turonian carbonate Mishrif reservoir of southern Iraq. Main dissolved  
29 constituents, trace elements,  $\delta^2\text{H}$  and  $\delta^{18}\text{O}$ ,  $^{87}\text{Sr}/^{86}\text{Sr}$ , mineral saturation indices and  
30 thermodynamic calculations were investigated in formation waters from the Mishrif  
31 Formation to obtain a better understanding of brine evolution and diagenetic effects over  
32 geological time. Previous published  $\delta^{11}\text{B}$  data were also reinterpreted as a geothermometer  
33 tool. The results are compared with previous published data for local oilfields and coeval  
34 formations in the Arabian Gulf. The Mishrif brine has a marine origin and is diagenetically  
35 modified to Ca-excess and Na-deficit. Formation waters are quartz supersaturated and are in  
36 equilibrium with chalcedony and calcite-dolomite in the temperatures range of 50–75°C,  
37 which is also confirmed by calcite-water oxygen isotope fractionation and  $\delta^{11}\text{B}$   
38 geothermometer. The potential role of clays in conditioning brine chemistry during diagenetic  
39 processes was highlighted by activity diagrams; in particular, their adsorption/exchange  
40 effect on sodium could explain the lower temperature obtained by the Na/Li geothermometer  
41 ( $42 \pm 6$  °C). The  $\delta^2\text{H}$  and  $\delta^{18}\text{O}$  values show that oxygen isotope composition of the brines  
42 was isotopically more affected by interaction with limestone during diagenesis than seawater  
43 evaporation. The main effect is an  $^{18}\text{O}$ -enrichment on the brine starting from the SMOW  
44 value. Locally, dilution by present-day meteoric water was also detected (Rumaila South),  
45 which is shifted towards the local meteoric water line. The strontium isotope ratios range  
46 from 0.707713 to 0.707749 and correspond to a marine strontium of late Cenomanian–early  
47 Maastrichtian age, except for the Majnoon sample, which shows a more radiogenic value  
48 (0.708043). Radiogenic strontium and gypsum and anhydrite saturation indices of the  
49 Majnoon sample could indicate the contribution of calcium and sulphate from the strontium-  
50 rich sulphate minerals of the Cambrian salt domes occurring in the oilfields of southern Iraq.

1  
2  
3  
4  
5  
6  
7  
8  
9  
51 The higher manganese concentration (4 mg/l) and the slightly higher temperature inferred by  
52 geothermometers (up to 74 °C) in comparison with present-day could indicate that the  
53 Majnoon brine is a hot fluid, probably related to a deeper structure such as the Zagros  
54 Foredeep Fault.

10  
11  
12  
13  
14  
15  
55 **Keywords:** Oilfield waters; chemical composition; geothermometry; oxygen and hydrogen  
56 stable isotope ratios; strontium isotopes.

## 16 57 **1. Introduction**

17  
18  
19  
20  
21  
22  
23  
24  
25  
26  
27  
28  
29  
30  
31  
32  
33  
34  
35  
36  
37  
38  
39  
40  
41  
42  
43  
44  
45  
46  
47  
48  
49  
50  
51  
52  
53  
54  
55  
56  
57  
58  
59  
60  
61  
62  
63  
64  
65  
66  
67  
68  
69  
70  
71  
72  
73  
74  
75  
76  
77  
78  
79  
80  
81  
82  
83  
84  
85  
86  
87  
88  
89  
90  
91  
92  
93  
94  
95  
96  
97  
98  
99  
100  
101  
102  
103  
104  
105  
106  
107  
108  
109  
110  
111  
112  
113  
114  
115  
116  
117  
118  
119  
120  
121  
122  
123  
124  
125  
126  
127  
128  
129  
130  
131  
132  
133  
134  
135  
136  
137  
138  
139  
140  
141  
142  
143  
144  
145  
146  
147  
148  
149  
150  
151  
152  
153  
154  
155  
156  
157  
158  
159  
160  
161  
162  
163  
164  
165  
166  
167  
168  
169  
170  
171  
172  
173  
174  
175  
176  
177  
178  
179  
180  
181  
182  
183  
184  
185  
186  
187  
188  
189  
190  
191  
192  
193  
194  
195  
196  
197  
198  
199  
200  
201  
202  
203  
204  
205  
206  
207  
208  
209  
210  
211  
212  
213  
214  
215  
216  
217  
218  
219  
220  
221  
222  
223  
224  
225  
226  
227  
228  
229  
230  
231  
232  
233  
234  
235  
236  
237  
238  
239  
240  
241  
242  
243  
244  
245  
246  
247  
248  
249  
250  
251  
252  
253  
254  
255  
256  
257  
258  
259  
260  
261  
262  
263  
264  
265  
266  
267  
268  
269  
270  
271  
272  
273  
274  
275  
276  
277  
278  
279  
280  
281  
282  
283  
284  
285  
286  
287  
288  
289  
290  
291  
292  
293  
294  
295  
296  
297  
298  
299  
300  
301  
302  
303  
304  
305  
306  
307  
308  
309  
310  
311  
312  
313  
314  
315  
316  
317  
318  
319  
320  
321  
322  
323  
324  
325  
326  
327  
328  
329  
330  
331  
332  
333  
334  
335  
336  
337  
338  
339  
340  
341  
342  
343  
344  
345  
346  
347  
348  
349  
350  
351  
352  
353  
354  
355  
356  
357  
358  
359  
360  
361  
362  
363  
364  
365  
366  
367  
368  
369  
370  
371  
372  
373  
374  
375  
376  
377  
378  
379  
380  
381  
382  
383  
384  
385  
386  
387  
388  
389  
390  
391  
392  
393  
394  
395  
396  
397  
398  
399  
400  
401  
402  
403  
404  
405  
406  
407  
408  
409  
410  
411  
412  
413  
414  
415  
416  
417  
418  
419  
420  
421  
422  
423  
424  
425  
426  
427  
428  
429  
430  
431  
432  
433  
434  
435  
436  
437  
438  
439  
440  
441  
442  
443  
444  
445  
446  
447  
448  
449  
450  
451  
452  
453  
454  
455  
456  
457  
458  
459  
460  
461  
462  
463  
464  
465  
466  
467  
468  
469  
470  
471  
472  
473  
474  
475  
476  
477  
478  
479  
480  
481  
482  
483  
484  
485  
486  
487  
488  
489  
490  
491  
492  
493  
494  
495  
496  
497  
498  
499  
500  
501  
502  
503  
504  
505  
506  
507  
508  
509  
510  
511  
512  
513  
514  
515  
516  
517  
518  
519  
520  
521  
522  
523  
524  
525  
526  
527  
528  
529  
530  
531  
532  
533  
534  
535  
536  
537  
538  
539  
540  
541  
542  
543  
544  
545  
546  
547  
548  
549  
550  
551  
552  
553  
554  
555  
556  
557  
558  
559  
560  
561  
562  
563  
564  
565  
566  
567  
568  
569  
570  
571  
572  
573  
574  
575  
576  
577  
578  
579  
580  
581  
582  
583  
584  
585  
586  
587  
588  
589  
590  
591  
592  
593  
594  
595  
596  
597  
598  
599  
600  
601  
602  
603  
604  
605  
606  
607  
608  
609  
610  
611  
612  
613  
614  
615  
616  
617  
618  
619  
620  
621  
622  
623  
624  
625  
626  
627  
628  
629  
630  
631  
632  
633  
634  
635  
636  
637  
638  
639  
640  
641  
642  
643  
644  
645  
646  
647  
648  
649  
650  
651  
652  
653  
654  
655  
656  
657  
658  
659  
660  
661  
662  
663  
664  
665  
666  
667  
668  
669  
670  
671  
672  
673  
674  
675  
676  
677  
678  
679  
680  
681  
682  
683  
684  
685  
686  
687  
688  
689  
690  
691  
692  
693  
694  
695  
696  
697  
698  
699  
700  
701  
702  
703  
704  
705  
706  
707  
708  
709  
710  
711  
712  
713  
714  
715  
716  
717  
718  
719  
720  
721  
722  
723  
724  
725  
726  
727  
728  
729  
730  
731  
732  
733  
734  
735  
736  
737  
738  
739  
740  
741  
742  
743  
744  
745  
746  
747  
748  
749  
750  
751  
752  
753  
754  
755  
756  
757  
758  
759  
760  
761  
762  
763  
764  
765  
766  
767  
768  
769  
770  
771  
772  
773  
774  
775  
776  
777  
778  
779  
780  
781  
782  
783  
784  
785  
786  
787  
788  
789  
790  
791  
792  
793  
794  
795  
796  
797  
798  
799  
800  
801  
802  
803  
804  
805  
806  
807  
808  
809  
810  
811  
812  
813  
814  
815  
816  
817  
818  
819  
820  
821  
822  
823  
824  
825  
826  
827  
828  
829  
830  
831  
832  
833  
834  
835  
836  
837  
838  
839  
840  
841  
842  
843  
844  
845  
846  
847  
848  
849  
850  
851  
852  
853  
854  
855  
856  
857  
858  
859  
860  
861  
862  
863  
864  
865  
866  
867  
868  
869  
870  
871  
872  
873  
874  
875  
876  
877  
878  
879  
880  
881  
882  
883  
884  
885  
886  
887  
888  
889  
890  
891  
892  
893  
894  
895  
896  
897  
898  
899  
900  
901  
902  
903  
904  
905  
906  
907  
908  
909  
910  
911  
912  
913  
914  
915  
916  
917  
918  
919  
920  
921  
922  
923  
924  
925  
926  
927  
928  
929  
930  
931  
932  
933  
934  
935  
936  
937  
938  
939  
940  
941  
942  
943  
944  
945  
946  
947  
948  
949  
950  
951  
952  
953  
954  
955  
956  
957  
958  
959  
960  
961  
962  
963  
964  
965  
966  
967  
968  
969  
970  
971  
972  
973  
974  
975  
976  
977  
978  
979  
980  
981  
982  
983  
984  
985  
986  
987  
988  
989  
990  
991  
992  
993  
994  
995  
996  
997  
998  
999  
1000

In the Jurassic–Cretaceous petroleum system of southern Iraq, hydrocarbons are mainly trapped in Lower Cretaceous sandstone and carbonate reservoirs. Crude oil is generated from the organic-rich Upper Jurassic (Sargelu and Sulaiy formations) changing the Lower Cretaceous carbonates of the Yamama Formation and the Zubair Formation, a clastics reservoir (Abeed et al., 2012; Abeed et al., 2013). The chemical composition of formation waters from the Yamama reservoir in the Zubair and North/South Rumaila oilfields is mainly composed of chloride (up to 143,589 ppm) with a salinity 6.2 times higher than seawater (Jamil, 1978), as for West Qurna oilfield, salinity 7.3 times higher than seawater and dominated by 191,700 ppm of chloride (Al-Marsoumi and Abdul-Wahab, 2005). These prior works utilized brine chemistry but did not address the evolution of the reservoir brine, as they relied mainly on cations and anions without considering isotopes. More recently, the boron stable isotope ratio of the brine from the Mishrif reservoir has given a seawater signature (Awadh et al., 2019a; Awadh et al., 2018) and highlighted the role of salinity in generating the formation pressure and controlling the fluid flow (Al-Mimar and Awadh, 2019). The developing of the oilfield brines over the geological time and its response to the flooding and diagenesis have a significant impact on petroleum reservoir quality, but this subject has not yet been investigated.

1  
2  
3  
4  
5  
6  
7  
8  
9  
10  
11  
12  
13  
14  
15  
16  
17  
18  
19  
20  
21  
22  
23  
24  
25  
26  
27  
28  
29  
30  
31  
32  
33  
34  
35  
36  
37  
38  
39  
40  
41  
42  
43  
44  
45  
46  
47  
48  
49  
50  
51  
52  
53  
54  
55  
56  
57  
58  
59  
60  
61  
62  
63  
64  
65

75 The diagenetic effects on brine waters can be evaluated by comparing the Na, Ca and  
76 Cl concentrations of the brine with those of seawater and with the so-called basinal fluid line  
77 in the Ca-excess versus Na-deficit binary diagram (Davisson and Criss, 1996). However, in  
78 this plot the interpretation could be misguided because: (i) the reference basinal fluid line  
79 takes into account only plagioclase albitisation, often without checking the real  
80 thermodynamic equilibria state of the involved waters; and ii) modelling involves the current  
81 seawater composition disregarding that of past periods (Babel and Schreiber, 2014;  
82 Lowenstein et al., 2003). A combination of isotope parameters as O-H stable isotope ratios  
83 and  $^{87}\text{Sr}/^{86}\text{Sr}$  was proposed by Danquigny et al. (2005) to evaluate the effect of water  
84 flooding in the Mishrif Formation water of Qatar. However, in that work, seawater  
85 evaporation, the isotope salt effect (Horita et al., 1993), and the contribution of radiogenic  
86 strontium to the limestones of the Mishrif Formation were not considered.

75  
76  
77  
78  
79  
80  
81  
82  
83  
84  
85  
86  
87  
88  
89  
90  
91  
92  
93  
94  
95  
96  
97  
98

The objectives of this research are: i) to investigate the origin of the oilfield waters; ii)  
to evaluate the composition of oilfield waters over time; and iii) to trace the influence of  
diagenesis and any geothermal effects on the brine. This investigation considers the above  
described effects and processes in the Mishrif Formation brines by reinterpreting the  
previously published main chemical constituents, along with new and original data on trace  
elements, oxygen and hydrogen water isotope ratio, the  $^{87}\text{Sr}/^{86}\text{Sr}$  ratio, and thermodynamic  
calculations. Moreover, the previously published data of boron isotope ratio  $\delta^{11}\text{B}$  (Awadh et  
al., 2019a; Awadh et al., 2018) are here reinterpreted as a geothermometer tool, and are  
results compared with those obtained from chemical geothermometers. The main research  
contribution is to obtain better understanding of the oilfield brines evolution.

## 2. Geological setting

### 2.1. Oilfield locations, main geological features and tectonics

99 The studied oilfields, Rumaila South (RU), Rumaila North (R), West Qurna (WQ), Zubair  
100 (ZB) and Majnoon (MJ) are located in southern part of Iraq (Jassim and Buday, 2006) (Fig.  
101 1A). The Mesopotamian zone extends from middle to southern Iraq as a relatively flat terrain  
102 with a gradient of less than 10 cm/km in the north-west to the Arabian Gulf. The zone was  
103 probably uplifted during Hercynian deformation but was subject to subsidence from the Late  
104 Permian onwards (Jassim and Buday, 2006). The oilfields are located in the Zubair zone  
105 (Grabowski Jr., 2014; Sadooni and Aqrabi, 2000), southern part of the Mesopotamia plain  
106 (Fig. 1A), an area characterized by the presence of a gentle subsurface succession of  
107 anticlinal and synclinal structures. These structures form giant hydrocarbon traps: Rumaila  
108 South (37 km length, 16 km width), Rumaila North (40 km, 13.5 km), West Qurna (35 km, 8  
109 km) and Majnoon (48 km, 10 km).

110 From the interpretation of gravity and magnetic data, Alyasi et al. (2014) mentioned  
111 that the presence of anticlinal structures is due to the effect of the evaporites of the Late  
112 Jurassic Gotnia Formation and Late Ediacaran – Early Cambrian Hormuz Formation in  
113 addition to other tectonic forces, where salts moves upward by buoyant forces and the denser  
114 rocks remain below them. To the north of the Arabian Gulf, huge salt-gypsum domes are  
115 exposed at a surface coexisting with a mixture of igneous and metamorphic rocks peeled off  
116 from the Precambrian crystalline basement (Mortazavi et al., 2017). Jabal Sanam is one of the  
117 salt diapirs in southern Iraq / northern Kuwait border (Fig. 1); it is an extension of the  
118 Hormuz Formation, located in Iran at the northern part of the Arabian Gulf, which contains  
119 more than 200 salt domes composed of sequences of evaporates, shales, siltstones and  
120 carbonates (Mortazavi et al., 2017). The role of tectonic events (extensional faulting) and  
121 differential loading of sedimentary cover above the mobile salt layer are the main triggering  
122 factors of the salt diapirism (Singh, 2012). In particular, the Permo-Triassic Tethyan rifting,  
123 the Cretaceous-Paleogene obduction and the compressive events associated with basement

124 reactivation of north-south Arabian trends could have started the episodic salt diapir activity  
125 in the area of this study (Singh, 2012). However, traces of a neotectonic reactivation were  
126 also documented (Sissakian et al., 2017).

127 The Zubair zone is a southern part of the Mesopotamian Basin that is located close to  
128 the junction of the Arabian Shelf and Iranian continental block. Collision of these plates at  
129 the Mesozoic-Cenozoic boundary produced the Zagros Foredeep fault and the Mesopotamian  
130 Basin, which is a member of the Arabian Gulf Basin (Konyuhov and Maleki, 2006). During  
131 the Mesozoic and Cenozoic, the study area was a tropical region, with organic-rich  
132 carbonates or organic-rich argillaceous sediments being deposited. Good-quality source rocks  
133 were preserved in different intervals of geological time, particularly during the Mesozoic. For  
134 example (Fig. 1B): the Alan Formation in the Middle Jurassic; the Sargelu, Najmah and  
135 Sulaiy formations are the source rocks in the Upper Jurassic; the Yamama Formation is a  
136 reservoir and productive carbonate and the Zubair Formation is a reservoir and productive  
137 sand in the Lower Cretaceous; the Ratawi, Shuaiba and Nahr Umr formations are carbonate  
138 reservoirs in the Lower Cretaceous. The Mauddud, Ahmadi and Rumaila formations are the  
139 mainly carbonate **reservoirs** in the Cenomanian. The Mishrif Formation is a main carbonate  
140 reservoir of the Cenomanian-Turonian (Fig. 1B). The Khasib and Tanuma formations are  
141 poor reservoirs. Tectonic fracturing of younger higher carbonate permits vertical migration of  
142 hydrocarbons into anticlines under efficient evaporitic seals. The regional evaporite seal is  
143 Gotnia Formation in the Upper Jurassic, and Fat'ha Formation in the **Tertiary** (Fig. 1B).

## 144 *2.2. Stratigraphy, paleogeography and mineralogy*

145 The Mishrif Formation is the main productive reservoir in southern Iraq, the United Arab  
146 Emirates, Oman, and Qatar. It was deposited in a shallow environment on the Rumaila  
147 Formation conformity. Its upper contact is unconformable with the Khasib Formation,  
148 representing a regression in the Turonian-Campanian age (Al-Mimar et al., 2018;

149 Awadeesian et al., 2019). It is represented by a unique lithostratigraphic unit regionally  
150 deposited in a fluctuating environment of shallow to deep-water reflecting the tectonic  
151 activity in the area (Alsharhan and Nairn, 1988). The carbonate rocks are composed of  
152 bioclastic particles (algae, rudist and coral reef) and represent the main facies of the Mishrif  
153 Formation. In terms of mineralogy, the Mishrif Formation is mainly composed of calcite  
154 (90% av.), with heterogeneous distribution of small amounts of dolomite, kaolinite, chlorite,  
155 authigenic quartz and clays (smectites and mixed layers) that do not exceed 10% (Al-Mimar  
156 et al., 2018). Southwardly, facies change to distal mid-ramp and proximal mid-ramp deposits  
157 and grade into outer-ramp deposits (Aqrawi et al., 1998). Eastwardly, close to the Zagros  
158 Foredeep Fault (ZFF) on the border with Iran, the Mishrif Formation is thicker (up to 400 m)  
159 and deeper (up to 3000 m) (Abbas and Mahdi, 2019; Mahdi et al., 2013). In particular, thick  
160 lagoonal units were deposited in the Majnoon field, implying a paleogeographic change in the  
161 eastern part of the study area where carbonate production caught up with the rising sea level  
162 until the filling of accommodation space with lagoonal deposits (Mahdi et al., 2013). The  
163 movement of the Hormuz Formation's salts was particularly important in southern Iraq  
164 (Murriss, 1980). Sadooni (2005) suggested that rudist build-ups in the Basrah area nucleated  
165 on the crests of growing salt structures. When the build-ups reached wave-base, they were  
166 eroded and rudist fragments were reworked, transported and dispersed to form bioclastic  
167 packstone/grainstones (Aqrawi et al., 2010).

### 3. Methodology

#### 3.1. Chemical and isotope analyses

170 Physicochemical parameters and major ion composition of five formation water samples  
171 from Rumaila South (RU287), Rumaila North (R590), West Qurna (WQ87), Majnoon  
172 (MJ20), and Zubair (ZB140) oilfields were reprised from Awadh et al. (2018) (mean values



173 and standard deviations at N = 28) and reinterpreted to investigate diagenesis and the  
174 temperature of the system using geothermometry. In this study, trace elements (total sulphur,  
175 Ba, Li, Fe, Mn, Rb, Sr) were analysed at the ALS Group Laboratory in Seville (Spain) using  
176 Inductively Coupled Plasma-Atomic Emission Spectroscopy (ICP-AES; ALS analytical code  
177 ME-ICP14L) after filtration and acidification by nitric acid. The dissolved silica as SiO<sub>2</sub>(aq)  
178 was analysed using the heteropoly blue spectrophotometric method (Clesceri et al., 1999) on  
179 filtered and diluted (1:5 by 18 MOhm ASTM Type 1 water) samples. The delta isotope  
180 values of hydrogen and oxygen of water molecules in ‰ versus V-SMOW reference standard  
181  $\delta^2\text{H}(\text{H}_2\text{O})_c$  and  $\delta^{18}\text{O}(\text{H}_2\text{O})_c$ , respectively, were obtained; where subscript ‘c’ represents the  
182 ‘composition’ scale (Horita et al., 1993). These isotope measurements were conducted by the  
183 H<sub>2</sub>-H<sub>2</sub>O and CO<sub>2</sub>-H<sub>2</sub>O gas equilibration isotope ratio mass spectrometry (IRMS) method on  
184 the vacuum-distilled samples (Boschetti et al., 2011). The salt effect parameter  $10^3\ln\Gamma$  of the  
185 brines was calculated taking into account the chemical composition and the temperature of  
186 the samples by PHREEQCI code, version 3, with the Pitzer thermodynamic database  
187 (Boschetti et al., 2011; Horita et al., 1993; Parkhurst and Appelo, 2013). According to Horita  
188 et al. (1993), the delta activity of hydrogen and oxygen,  $\delta^2\text{H}(\text{H}_2\text{O})_a$  and  $\delta^{18}\text{O}(\text{H}_2\text{O})_a$ ,  
189 respectively, was obtained summing the salt effect parameter and the delta isotope  
190 composition of hydrogen and oxygen.

191 The strontium isotope ratios,  $^{87}\text{Sr}/^{86}\text{Sr}$ , of the brines were obtained using thermal  
192 ionization mass spectrometry (TIMS). Prior to the analytical process, separation of Sr from  
193 the matrix bulk elements, and especially from Rb, was executed using heat plate evaporation  
194 with Teflon® vials at 80°C, followed by chromatographic extraction using Sr-Resin™  
195 (TrisKem International) (crown-ether (4, 4' (5')-di-t-butylcyclohexano-18-crown-6). The  
196 final Sr fraction was recovered from the bulk using HNO<sub>3</sub> 0.05M as eluent, then evaporated  
197 on a heat plate at 80°C and introduced into the mass spectrometer. Possible  $^{87}\text{Rb}$  interferences

198 were corrected in the Sr analysis and the  $^{87}\text{Sr}/^{86}\text{Sr}$  ratio was normalised in order to correct for  
199 mass fractionation, taking into account a reference value of  $^{86}\text{Sr}/^{88}\text{Sr} = 0.1194$ . The  $^{87}\text{Sr}/^{86}\text{Sr}$   
200 results were normalised to NBS SRM 987 (National Bureau of Standards Standard Reference  
201 Material 987 – strontium carbonate). Internal precision was  $3 \times 10^{-6}$ .

### 202 *3.2. Thermodynamic calculations*

203 PHREEQCI code and Pitzer thermodynamic dataset were also used to define:

- 204 i) the mineral-water saturation indices  $SI = \log(\text{IAP}/K)$ , where IAP and K are the ion  
205 activity product of the dissolved constituents and K is the mineral solubility product in a  
206 specific reaction, respectively, and the partial pressure of carbon dioxide by the Peng–  
207 Robinson equation of state (Parkhurst and Appelo, 2013);
- 208 ii) a geothermal model based on multimineral equilibria.

209 Results were compared to previously published chemical and isotopic  
210 geothermometers specific for sedimentary brines (Boschetti et al., 2015; Kharaka and  
211 Mariner, 1989; Sanjuan et al., 2014). The calculated activity of the dissolved constituents was  
212 also used to calculate the saturation index of a carbonate solid solution made of calcite,  
213 magnesite, rhodochrosite, siderite and strontianite by EQ3/6 code, version 8 (Wolery and  
214 Jarek, 2003).

215 The Geochemist's Workbench® code (GWB), version 7.0.6 (Bethke and Yeakel,  
216 2008), was used to calculate the evaporation path of Cretaceous seawater using the React  
217 tool, HMW thermodynamic database, and the main chemical composition of seawater during  
218 that period (Bäbel and Schreiber, 2014). According to Bäbel and Schreiber (2014), a chloride  
219 concentration of present-day seawater ( $565 \text{ mmol kg}^{-1} \text{ H}_2\text{O}$ ) was taken as a reference; then  
220 chloride concentration was charge-balanced, taking into account other main constituents and  
221  $\text{pH} = 7.5$  (Hönisch et al., 2012), and a  $\log\text{PCO}_2(\text{g}) = -3$  was settled during evaporation. This

222 latter corresponded to a mean concentration of 1000 ppmv of CO<sub>2</sub> in the Cretaceous  
223 atmosphere (Hönisch et al., 2012; Wang et al., 2014).

224 Finally, activity diagrams using a thermodynamic database of the minerals and  
225 dissolved constituents, recalculated at a pressure of 20 MPa, were plotted using the Act tool  
226 of the GWB-code (Boschetti et al., 2016). The Rxn tool of the same code was also used to  
227 check the thermodynamic equilibria of specific reactions.

#### 228 **4. Results and Discussion**

229 The physicochemical and isotope parameters are reported in Table 1. The recalculated main  
230 chemical composition in equivalents per liter of formation water from the southern region of  
231 Iraq shows a Cl-Na composition. In particular, the Na/Cl equivalent ratios range span  
232 between 0.77 and 0.91, with a mean of  $0.83 \pm 0.05$ , which is similar to that of present-day  
233 seawater (0.86). The Ca/(SO<sub>4</sub> + HCO<sub>3</sub>) equivalent ratios of the brines are largely over 1, with  
234 a mean of  $44 \pm 19$  and a range between 15 and 78. Therefore, brines can be classified also as  
235 Ca-Cl, according to Rosenthal (1997). The mean measured temperature of the water sampled  
236 in the Mishrif Formation is  $65 \pm 2$  °C (N = 28) (Awadh et al., 2018). Between the  
237 investigated trace elements, the concentration of barium and manganese are higher in  
238 Majnoon (5.43 and 4.47 mg/l, respectively) in comparison with the range of the samples from  
239 the other oilfields (1.44-1.79 and 0.10-0.13 mg/l, respectively). All samples showed  
240 supersaturation in calcite, aragonite, and dolomite (Table 2). Barite and anhydrite are also  
241 supersaturated in all but one sample (RU287). Finally, waters are in equilibrium with  
242 chalcedony and oversaturated in quartz.

##### 243 *4.1 Chemical composition: diagenesis and geothermometry*

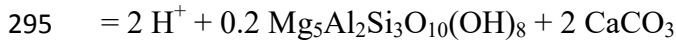
244 According to the previous published works on southern Iraq oilfields (Awadh et al., 2019a;  
245 Awadh et al., 2018), the above described chemical ratios of Na/Cl =  $0.83 \pm 0.05$  and Ca/(SO<sub>4</sub>

246 + HCO<sub>3</sub>) = 44 ± 19 are typical of marine origin formation waters that have undergone  
247 chemical modification due to diagenesis (Boschetti et al., 2011; Rosenthal, 1997). The  
248 Langelier–Ludwig and brine differentiation diagrams (Boschetti, 2011; Hounslow, 1995) of  
249 Figure 2 depict the distinct composition of the oilfield brines in comparison with the local  
250 shallow groundwater (Hamdan, 2017) and surface waters (Al-Mallah, 2014; ROPME, 2011;  
251 Rzóška, 1980). Surface water (Ghalib and Almallah, 2017), water produced from crude oil  
252 dehydration (Al-Shamkhani, 2013) or a mixture of both were used in the oilfields for water-  
253 flooding purposes. In Figure 2A, the brine samples from this study and literature are grouped  
254 in a narrow field, whereas in the brine differentiation plot (Figure 2B), brines are displaced  
255 between the evaporation curve of Cretaceous seawater and the produced waters from  
256 dehydrators (Al-Furaiji, 2016; Al-Shamkhani, 2013). Similarly to the Cretaceous formation  
257 brines in Venezuela (Boschetti et al., 2016), most of the studied brines affected by diagenesis  
258 show a Ca-excess and Na-deficit and seem to follow the typical Ca-Na exchange trend of the  
259 so-called basinal fluid line (Davisson and Criss, 1996) (Figure 3). Sample RU287 was  
260 probably affected by dolomitization and then by mixing with waters produced from crude  
261 dehydrators (“produced water” field in Figure 3). The hottest (115°C) water sample from the  
262 deeper Zubair sandstone indicates that the chemical effects of Ca-Na reactions (Al-Marsoumi  
263 and Abdul-Wahab, 2005), most probably due to albitisation, are more pronounced at higher  
264 temperatures (Figure 3A). Different from the Mishrif Formation, albite was found in the  
265 Zubair Formation (Al-Ziayyir, 2018). Moreover, from a theoretical point of view, the  
266 diagenetic effects could be more or less pronounced if the variability of the seawater  
267 composition in the past was considered. If Cretaceous seawater is used as a reference instead  
268 of present-day seawater, the oilfield brines are more clustered towards the axes **origin of**  
269 **Figure 3B** (which coincides with the composition of less saline surface water) or towards the  
270 “produced water” fields. The dolomitization process seems to have had a greater role in the

271 Ca-excess of the waters (Figure 3B). However, the geothermal modelling indicated in Figure  
272 4, also suggests that calcite-dolomite equilibration occurred along with chalcedony instead of  
273 quartz. In that diagram, all but one sample are clustered between 50 and 75°C isotherms, a  
274 range that includes the temperatures of  $64 \pm 5^\circ\text{C}$  (N = 9) and  $64 \pm 7^\circ\text{C}$  (N = 5) obtained by  
275 Mg-Li and chalcedony geothermometers, respectively — the latter corrected for dissolved  
276 silica activity and pressure (Kharaka and Mariner, 1989) (Table 2). The exception is  
277 represented by sample MJ20 (Majnoon oilfield), which is shifted towards the quartz-dolomite  
278 (ordered) model (Figure 4) and shows the lowest temperature from quartz and chalcedony  
279 from geothermometric equations (Table 2). Such an apparent convergence between quartz  
280 and chalcedony is probably attributable to the greater depth and pressure in the MJ20  
281 borehole (Table 1), conditions that could enhance simultaneous equilibria between the fluid  
282 and the two mineral phases (Giggenbach, 1991). For the MJ20 sample, a mean value of  
283  $70.5^\circ\text{C}$  between the geothermometric equations of quartz and chalcedony shows a good  
284 agreement with the  $68^\circ\text{C}$  obtained from the Mg-Li geothermometer (Table 2).

285 Globally, the mean inferred temperature of the brines are quite similar to the mean  
286 temperature measured at depth, confirming that the present-day borehole temperatures are not  
287 so different from those reached during Neogene burial (Abeed et al., 2013). Sample MJ20 is  
288 an exception, showing a temperature  $10^\circ\text{C}$  higher. This is probably due to the effect of  
289 greater borehole depth (Fig. 1B) and pressure. The Majnoon oilfield had the highest  
290 measured values (Table 1). Activity diagrams of Figures 5A and 5B show that Mg  
291 concentration in the brine seems to be limited by dolomite and by chlorite. To check the  
292 coexistence of the minerals, the thermodynamics of the following reaction have been  
293 calculated (Supplementary File 1):





296 At P = 20 MPa and buffering conditions of Figure 5A, except for Mg which has been  
297 buffered by clinocllore,  $\text{Mg}_5\text{Al}_2\text{Si}_3\text{O}_{10}(\text{OH})_8$ , instead of dolomite. The above reaction is in  
298 equilibria at 64°C using  $\log[\text{Ca}^{2+}/(\text{H}^+)^2] = 11.11$  and  $\log[\text{SiO}_2(\text{aq})] = -3.32$ , which  
299 corresponds to the mean activity values of all investigated samples (Supplementary File 1).  
300 Therefore, this corroborates not only that dolomite and chlorite could **coexist** in the studied  
301 basin, but also the temperature values obtained by geothermometers, in particular those by  
302 Li-Mg and chalcedony equations (Table 2).

303 Figure 5 also shows that the Ca/Na ratio is probably controlled by smectite instead of  
304 albite. The role of clays on the control of Na amount in solution by Ca-Na exchange or Na  
305 adsorption could also explain the lower temperatures of  $42 \pm 6$  °C obtained using the Na/Li  
306 geothermometer (Kharaka and Mariner, 1989; Sanjuan et al., 2014) (Table 2). Similarly, the  
307 values obtained from the boron isotope geothermometer **gave an** underestimation of the brine  
308 temperature (Table 2). This could be due to a higher  $\delta^{11}\text{B}$  value in Cretaceous seawater (up to  
309 3‰ higher than the present; Lemarchand et al. 2002), together with a fractionation effect due  
310 to evaporation up to halite saturation (approximately +4‰) (Vengosh et al. 1992). Actually,  
311 by subtracting a value of 7‰ from the original values of the brines, a mean temperature of  $64$   
312  $\pm 6$ °C was obtained from the boron isotope geothermometric equation (Boschetti et al.,  
313 2015), which matches with that obtained by the calcite-dolomite-chlorite-kaolinite equilibria.

#### 314 4.2. Oxygen and hydrogen stable isotope ratios

315 The isotope composition value — i.e. not considering the salt effect according to Horita et al.  
316 (1993) — of the studied formation water is similar to that of the Mishrif Formation values  
317 from the Qatar oilfield values (Danquigny et al., 2005) (Figure 6). However, the calculation  
318 of isotope activity due to the salt effect reveals a high enrichment in  $\delta^2\text{H}$  (up to +8.3‰) and a

319 slight depletion in  $\delta^{18}\text{O}$  (up to -0.3‰) in comparison to the analysed isotope composition. As  
320 presented in Figure 6, the isotope composition of the formation waters from the samples  
321 analyzed in this study fall close to the final part of the hook path derived from experimental  
322 seawater evaporation (e.g. Gonfiantini et al., 2018), thus confirming the marine origin of  
323 these samples, as previously inferred by the boron isotope (Awadh et al., 2018). It should be  
324 noted that the experimental hook paths of the evaporated seawater are generally analysed  
325 from salt pans without the addition of either new marine or meteoric water (i.e. closed  
326 system) (Gonfiantini, 1965; Gonfiantini et al., 2018). This could be the reason why the  
327 isotope activity values of the brine — i.e. considering the salt effect according to Horita et al.  
328 (1993) — do not fall on the hook path (Figure 6). In Figure 6, the Iraq meteoric water line  
329 (IMWL) and its prediction interval (parallel dashed lines with  $\delta^2\text{H} \pm 10.3$  ‰ from IMWL)  
330 were recalculated from the rainwater isotope data of Ali et al. (2015) using the error-in-  
331 variable (EIV) regression method (Boschetti et al., 2019). The extrapolation of the best fit  
332 line of the brine samples meets the prediction interval of the meteoric water line just between  
333 rain waters collected from Başrah city (Fig. 1) plus other southern Iraq areas (Al-Kinani et  
334 al., 2018; Ali et al., 2015; Jassem et al., 2018) and evaporated river samples from the Tigris  
335 and Euphrates (Jassem et al., 2018) (Figure 6). Sample RU287 shows the highest contribution  
336 of modern fresh water. It should also be remarked that, in comparison with other samples, the  
337 RU287 brine displays barite supersaturation (Table 2), which is probably due to the effect of  
338 mixing between brines and local water of meteoric origin or reinjected produced waters as a  
339 consequence of the water flooding (Ghalib and Almallah, 2017; Sorbie and Mackay, 2000).  
340 This is in line with the previously described chemical diagrams. On the opposite side, the  
341 extrapolated best fit line of the isotope activity of the brines meets the hooked evaporation  
342 path of seawater just on the top of the hump (Figure 6), which approximatively corresponds  
343 to gypsum saturation (Holser, 1979; Knauth and Beeunas, 1986).

344 Evaporated seawater samples from present-day sabkha and lagoon environments (i.e.  
1  
2 345 open systems) show  $\delta^{18}\text{O}$  up to +6.5‰, which is similar to those determined in the formation  
3  
4 346 brines of this study, but with  $\delta^2\text{H}$  enrichment up to approximately +30‰ (McKenzie et al.,  
5  
6  
7 347 1980; Nadler and Magaritz, 1980; Robinson and Gunatilaka, 1991). Lower deuterium values  
8  
9  
10 348 are mainly due to mixing with evaporated surface waters or groundwater of meteoric origin  
11  
12 349 (McKenzie et al., 1980; Robinson and Gunatilaka, 1991); whereas, flooding and mixing of  
13  
14 350 evaporated solution with new seawater inputs could shift the composition back to the starting  
15  
16 351 values (i.e. near V-SMOW) (Nadler and Magaritz, 1980) (Figure 6). A similar effect was  
17  
18  
19 352 observed in Miocene brines by comparison with  $\delta^{18}\text{O}$  from coeval gypsum, with the  
20  
21  
22 353 exception of the formation waters affected by a positive  $\delta^{18}\text{O}$ -shift as result of diagenetic  
23  
24 354 water-rock interaction with limestones (Boschetti et al., 2011). In a similar way, and  
25  
26 355 assuming that starting seawater during the Phanerozoic has remained isotopically similar to  
27  
28  
29 356 the present-day V-SMOW value (i.e. 0‰ both for oxygen and for hydrogen stable isotope  
30  
31 357 ratios) (Gregory and Taylor Jr, 1981; Ryb and Eiler, 2018; Sessions, 2016), the  $^{18}\text{O}$   
32  
33  
34 358 enrichment of formation waters as observed in samples MJ20, ZB140, and R590 could be due  
35  
36 359 to water–rock interaction. Therefore, water-rock interaction and dilution seem to be the main  
37  
38  
39 360 processes that affected in a significant manner the isotope composition of the studied brines.  
40  
41

42 361 Such a diagenetic effect was also hypothesised for the Mishrif Formation in Qatar  
43  
44 362 where limestones value ranges between  $+24.4 \text{ ‰} < \delta^{18}\text{O} \text{ (V-SMOW)} < +27.4 \text{ ‰}$ , formation  
45  
46 363 brines  $\delta^{18}\text{O}$  up to +5‰ (V-SMOW), and temperatures between 50 and 70°C have been  
47  
48  
49 364 measured (Deville de Periere, 2011). As the isotope values of the limestones from the same  
50  
51  
52 365 formation in southern Iraq are within the range of those measured in Qatar, i.e.  $+25.2 \text{ ‰} <$   
53  
54 366  $\delta^{18}\text{O} \text{ (V-SMOW)} < +27.4 \text{ ‰}$  (Taha and Abdullah, 2019), the diagenetic effect can be  
55  
56 367 hypothesised also for this area. Considering a mean value  $\delta^{18}\text{O}(\text{H}_2\text{O})_a = +3.9 \text{ ‰}$  (V-SMOW)  
57  
58  
59 368 for the brine samples that fall within the diagenetic arrow in Figure 6 and a mean value of  
60  
61  
62  
63  
64  
65



369  $\delta^{18}\text{O}$  (limestones) equal to +26.5 ‰ (V-SMOW) of the Mishrif Formation in southern Iraq, it  
370 is possible to calculate an oxygen isotope fractionation factor of  $1000\ln\alpha$  (calcite-water) =  
371 +22.3 ‰. This latter value corresponds to a temperature between 56°C (Kim and O'Neil,  
372 1997) and 69°C (Zheng, 1999). Other isotope effects due to clays and crude are probably not  
373 quantitatively important or less pronounced than the salt effect. Indeed, a fractionation  
374 between water and hydrocarbons should generate in brines a shift towards  $\delta^2\text{H}$  values higher  
375 than seawater (e.g., Horita, 2009), but this is not the case (Figure 6). Furthermore, the amount  
376 of clays minerals in the Mishrif Formation are probably insufficient to generate a significant  
377 isotope effect on the  $\delta^2\text{H}$  of the waters.

#### 378 4.3. Strontium isotope ratio

379 The strontium isotope ratios of the four brine samples analysed are  $0.707713 < {}^{87}\text{Sr}/{}^{86}\text{Sr} <$   
380  $0.707749$  (WQ87, RU287, ZB140, R590), which corresponds to a marine strontium of late  
381 Cenomanian–early Maastrichtian age (McArthur, 2010; McArthur et al., 2012); with the  
382 sample at the Majnoon oilfield (MJ20) showing the highest value of 0.708043. The Mishrif  
383 reservoir is Cenomanian–Turonian; therefore, the strontium isotope ratio should theoretically  
384 not be greater than  $0.707314 \pm 0.000005$  (McArthur, 2010; McArthur et al., 2012). The  
385 higher strontium isotope ratios in formation waters could suggest a contribution of more  
386 radiogenic strontium from injected waters when compared to the more saline and enriched  
387 brines (Danquigny et al., 2005), but in this case the oxygen and hydrogen stable isotope ratios  
388 are not less than the other samples. Moreover, it should be also noted that  ${}^{87}\text{Sr}/{}^{86}\text{Sr}$  values up  
389 to 0.707869 have been detected in the brines from the Mishrif Formation in Qatar (Al Khalij  
390 offshore field; Danquigny et al. 2005) and up to 0.70878 in the carbonate matrix of the coeval  
391 Sarvak Formation in southern Iran (Hajikazemi et al., 2012). Such elevated values detected at  
392 the disconformity surfaces of the formations are probably due to the contribution of meteoric  
393 water during diagenesis (e.g., Hajikazemi et al. 2012). However, the combination of high

394 manganese and radiogenic strontium contributions to the limestones of the Sarvak Formation  
1  
2  
3 395 of southern Iran were also attributed to different sources: i) a Cenomanian-Turonian subaerial  
4  
5 396 exposure; ii) diagenetic fluids; and iii) detritus (Navidtalab et al., 2016). Actually, all the  
6  
7 397 inspected brines of this study are undersaturated with respect to pure rhodocrosite ( $SI = -3.9 \pm$   
8  
9  
10 398  $0.8$ ), but in equilibrium with carbonate solid solution ( $SI = -0.082 \pm 0.261$ ) (Table 2). In  
11  
12 399 particular, despite its high Mn activity, the Majnoon brine MJ20 showed a slight  
13  
14 400 undersaturation in that solid solution. Therefore, the higher Mn concentration (up to 4 mg/l)  
15  
16 401 and radiogenic strontium at that brine could be acquired by limestone dissolution in a  
17  
18 402 disconformity layers. Alternatively, as suggested by the lowest gypsum and anhydrite  
19  
20 403 saturation indices of the Majnoon sample (Table 2), it cannot be excluded that there was a  
21  
22 404 contribution of radiogenic strontium-rich sulphate minerals from Cambrian salt domes (up to  
23  
24 405  $0.7092$ ) (McArthur et al., 2012). Salt domes characterise the fold settings in the oilfields of  
25  
26 406 southern Iraq (Al-Ameri et al., 2011; Al-Mimar and Awadh, 2019). The doming triggered  
27  
28 407 local uplift and emergence of paleo-exposure surfaces (Rahimpour-Bonab et al., 2013), thus  
29  
30 408 the shallow back shoal/lagoonal depositional environment of Mishrif limestones at the  
31  
32 409 Majnoon oilfield and the salt domes seem to be related (Aqrawi et al., 2010; Mahdi et al.,  
33  
34 410 2013). Moreover, “hydrothermal fluids” with temperatures up to  $80^{\circ}\text{C}$  were hypothesized to  
35  
36 411 form diagenetic cements (i.e., blocky calcite), dolomite and coarse crystalline pyrite during  
37  
38 412 deeper burial of the Sarvak Formation (Hajikazemi et al., 2017). Therefore, the chemical,  
39  
40 413 thermal and isotopic anomalies of the Majnoon brine suggest that it is the hottest fluid  
41  
42 414 probably related to the higher geothermal gradient of a deeper structure as the ZFF (Basilici  
43  
44 415 et al., 2020; Bordenave, 2008; Bordenave and Hegre, 2010).

## 54 416 **5. Conclusions**

57 417 This paper presented the first data on isotope ratios of oxygen, hydrogen, and strontium of  
58  
59 418 oilfield waters from southern Iraq, along with new trace element data and a reinterpretation of  
60  
61  
62  
63  
64  
65

1  
2  
3  
4  
5  
6  
7  
8  
9  
10  
11  
12  
13  
14  
15  
16  
17  
18  
19  
20  
21  
22  
23  
24  
25  
26  
27  
28  
29  
30  
31  
32  
33  
34  
35  
36  
37  
38  
39  
40  
41  
42  
43  
44  
45  
46  
47  
48  
49  
50  
51  
52  
53  
54  
55  
56  
57  
58  
59  
60  
61  
62  
63  
64  
65

419 previous published chemistry. Processes like diagenesis and seawater evaporation that  
420 typically occur in these fluids can be distinguished using classical ‘basinal fluid’ chemical  
421 diagrams. Mishrif Formation waters are Cretaceous connate brines and the different chemical  
422 composition of seawater of that period needs to be taken into account for a more correct  
423 interpretation. The Ca-excess versus Na-deficit composition of these kinds of fluids are  
424 usually explained by albitisation. However, it was verified by activity plots that in the Mishrif  
425 limestone reservoir the Na/Ca exchange that occurs in brines is mainly due to water-smectite  
426 equilibrium.

427         The values  $\delta^2\text{H}$  and  $\delta^{18}\text{O}$  obtained on selected samples show that oxygen isotope  
428 composition of the brines was isotopically more affected by equilibria with limestone than  
429 evaporation. The global effect of the water-rock interaction is an  $^{18}\text{O}$ -enrichment of the  
430 brines. Locally, dilution by present-day water of meteoric origin and shift towards the local  
431 meteoric water line also detected, probably as consequence of water-flooding (Rumaila  
432 South, sample RU287). Furthermore, it is also shown that isotope data cannot be separated  
433 from the interpretation of the chemical composition of sedimentary brines. The contribution  
434 of the salt effect on the stable isotope ratios of water molecules, i.e.  $^2\text{H}/^1\text{H}$  and  $^{18}\text{O}/^{16}\text{O}$ , needs  
435 to be evaluated because this parameter could vary the results during fractionation processes  
436 such as seawater evaporation and diagenesis. Hydrogen isotope ratios are probably more  
437 affected by the salt effect than other fractionations. Furthermore, taking into account the salt  
438 effect, the temperature range inferred from carbonate-water oxygen isotope ratio fractionation  
439 is comparable to that obtained from the chemical geothermometers, i.e. between 50 and 75°C.  
440 According to Abeed et al. (2013), these evaluations confirm that the present-day borehole  
441 temperatures are not so different from those reached during Neogene burial.

442         More recent mixing processes such as water floods could be detected by a comparison  
443 with the composition of the formation brine, waters produced from crude dehydrators, and

1 444 the local waters of meteoric origin. The strontium isotope ratio confirms the interaction of  
2 445 Cretaceous limestone for most of the studied samples, suggesting a late Cenomanian–early  
3  
4 446 Maastrichtian age, and an input of more radiogenic strontium in the Majnoon oilfield (MJ20  
5  
6  
7 447 sample). The brine sample from this latter oilfield showed a particular geochemical  
8  
9 448 characteristic. Despite the lower temperature measured at the MJ20 borehole (60°C), the  
10  
11 449 slightly higher temperature obtained by the Li-Mg, Na-Li and  $\delta^{11}\text{B}$  geothermometers (up to  
12  
13 450 74°C) is probably due to the deeper structure of that oilfield, which is closer to the ZFF. The  
14  
15 451 more radiogenic strontium ratio at Majnoon could be related to: i) debris input in the  
16  
17 452 limestone, which could explain also the high Mn content; or ii) interaction with local  
18  
19 453 Cambrian sulphates. An inspection of additional samples, sulphur stable isotope ratio  
20  
21 454 ( $^{34}\text{S}/^{32}\text{S}$ ) and radiogenic isotope of the halogens ( $^{139}\text{I}$ ,  $^{36}\text{Cl}$ ) could improve the knowledge of  
22  
23 455 the past water flow events and clarify the relationship between the high Mn concentration /  
24  
25 456 high radiogenic strontium in the Cretaceous limestones and the salt domes.  
26  
27  
28  
29  
30

### 31 **Acknowledgements**

32  
33  
34  
35 458 Special thanks to G. Venturelli for the comments and suggestions on a preliminary version of  
36  
37 459 the manuscript. The authors very much appreciate the Associate Editor, B.J. Katz, and the  
38  
39 460 two anonymous reviewers for their careful reading of the manuscript and all valuable  
40  
41 461 constructive comments and suggestions.  
42  
43  
44  
45

### 46 **Captions**

47  
48 463 **Table 1** – Physicochemical parameters, major ion composition, trace elements concentration,  
49 464 and isotopic results from Awadh et al. (2018) and this study.

50  
51 465 **Table 2** – Geothermometric results in Celsius degree (°C); mineral saturation indices (SI),  
52 466 and carbon dioxide partial pressure as  $\log\text{P}(\text{CO}_2)\text{g}$  obtained by PHREECI code, version 3,  
53 467 along with Pitzer thermodynamic dataset at the measured temperature and water pressure  
54 468 conditions (Table 1). EQ 3/6 code was also used to calculate the saturation indexes of  
55 469 carbonates solid solution.  
56

57  
58 470 **Figure 1** – A) Location map showing the studied oilfields at the Zubair zone, within the  
59 471 southern part of the Mesopotamia plain and to the southwest of the Zagros Foredeep Fault  
60 472 (ZFF); Stratigraphic correlation of the five oilfield wells penetrating four formations  
61

473 (Rumaila, Mishrif, Khasib, and Tanuma) in which there is a well from each oilfield (RU287  
474 from Rumaila South, R590 from Rumaila North, WQ87 from West Qurna, MJ20 from  
475 Majnoon, and ZB140 from Zubair oilfield); B) Typical section represents the stratigraphic  
476 setting in the study area.

477 **Figure 2** – Langelier–Ludwig (A) and Brine Differentiation Plot (B) of the oilfield brines of  
478 southern Iraq (Al-Mallah, 2014; Al-Marsoumi and Abdul-Wahab, 2005; Awadh et al., 2019b;  
479 Awadh et al., 2018; Jamil, 1978) compared with shallow groundwater (Hamdan, 2017), Shatt  
480 Al-Arab River (ROPME, 2011), Shatt Al-Basrah Canal, or ‘Main Drain’ (Al-Mallah, 2014)  
481 and seawater. In both diagrams, concentration of the dissolved species are in equivalent/liter;  
482 dashed ellipses depict the trend of the Tigris–Euphrates River system at Qurna and Shatt Al-  
483 Arab River during the 60s (Rzóska, 1980). In (B), Mishrif Formation’s brine waters from  
484 Awadh et al. (2018) are distinguished by black triangles; the five samples reprised in this  
485 study are highlighted by white crosses. The brine data from other references (Al-Mallah,  
486 2014; Al-Marsoumi and Abdul-Wahab, 2005; Awadh et al., 2019b; Jamil, 1978) are  
487 represented by white triangles. Produced waters from hydrocarbon dehydrators are also  
488 shown for comparison (dashed field) (Al-Furaiji, 2016; Al-Shamkhani, 2013). Arrows depict  
489 possible mixing trends. In the inset, the original fields of the diagram along with evaporation  
490 paths of present-day (Boschetti, 2011; Hounslow, 1995) and Cretaceous seawater (this study)  
491 are shown. G and H depict the gypsum and halite saturation points, respectively.

492 **Figure 3** –  $\text{Ca-excess} = 2 \times [\text{Ca}_{\text{meas}} - (\text{Ca}/\text{Cl})_{\text{SW}} \times \text{Cl}_{\text{meas}}]/40.08$  vs.  $\text{Na-deficit} = [(\text{Na}/\text{Cl})_{\text{SW}} \times$   
493  $\text{Cl}_{\text{meas}} - \text{Na}_{\text{meas}}] / 22.99$  diagram for oilfield waters from southern Iraq, where meas =  
494 measured, SW = seawater and Ca, Na and Cl are elemental concentrations in mg/l (Davisson  
495 and Criss, 1996). The 1Ca-2Na or 1Ca-1Na exchange arrows depict the possible paths of  
496 formation fluids in sedimentary basins during plagioclase albitisation (Davisson and Criss,  
497 1996). In (A) and (B) diagrams, present-day and Cretaceous seawater were used as SW-  
498 composition, respectively. In both: light gray ellipse at the origin of the plot represents the  
499 initial seawater composition (i.e. before evaporation), local groundwater and surface waters  
500 composition; dashed and dot-dashed lines depict the evaporation paths of Cretaceous and  
501 present-day seawaters, respectively. Other symbols and fields as in Figure 2.

502 **Figure 4** – Base-10 logarithm of silicium versus calcium/magnesium ratio diagram of the  
503 Mishrif Formation’s brines from southern Iraq (molar concentration). Dashed curves depict  
504 the simultaneous equilibria of calcite-dolomites plus quartz (light gray) or chacedony (black)  
505 calculated by PHREEQCI code and pitzer thermodynamic dataset (Parkhurst and Appelo,  
506 2013) at the mean pressure of the five samples (27.8 MPa; Table 1).

507 **Figure 5** – Activity plots for the system  $\text{Na}_2\text{O}-\text{CaO}-\text{MgO}-\text{Al}_2\text{O}_3-\text{SiO}_2-\text{H}_2\text{O}-\text{CO}_2$  at  $P = 200$   
508 bar and  $50 < T < 75$  °C. In (A), the activity of dissolved silica has been fixed at the mean  
509 value detected in the waters, i.e.:  $\log[\text{SiO}_2(\text{aq})] = -3.32$ , whereas in (B) it was buffered by  
510 chalcedony. In both diagrams: water activity at  $\log[\text{H}_2\text{O}] = -0.0855$  (mean value of the local  
511 brines); aluminium buffered by kaolinite; magnesium and  $\text{HCO}_3^-$  buffered by dolomite and  
512 calcite, respectively.

513 **Figure 6** –  $\delta^2\text{H}(\text{H}_2\text{O})$  vs.  $\delta^{18}\text{O}(\text{H}_2\text{O})$  diagram. Samples from this study are differentiated for  
514 isotope composition (white-crossed gray triangles) and isotope activity (white-crossed black  
515 triangles): the former represent analytical results of water samples after vacuum distillation  
516 and IRMS; the latter represent isotope composition plus the theoretical salt effect (Horita et  
517 al., 1993) (Table 1). Water isotope composition of brines from the Mishrif Formation in  
518 Qatar are also shown for comparison (open triangles) (Danquigny et al., 2005). Dotted lines  
519 depict the linear best fits of the two ways of representation of isotope ratios in brines.

520 Evaporated seawaters from a closed (Gonfiantini et al., 2018) and open (McKenzie et al.,  
1 521 1980; Nadler and Magaritz, 1980; Robinson and Gunatilaka, 1991) system are shown for  
2 522 comparison. The previous published data on isotope composition of the Arabian Gulf  
3 523 seawater and its evaporated composition are depicted by the field with waves and forward-  
4 524 back curved arrows, respectively (Bagheri et al., 2014; McKenzie et al., 1980; Robinson and  
5 525 Gunatilaka, 1991; Yurtsever, 1994). Rainwater samples (drops) from southern Iraq (Al-  
6 526 Kinani et al., 2018; Ali et al., 2015; Jassem et al., 2018) and northern Kuwait (Hadi et al.,  
7 527 2016) are also shown for comparison. Tigris and Euphrates samples are represented by open  
8 528 squares; samples out of the IMWL's (Iraq meteoric water line) prediction interval are  
9 529 evaporated surface water samples (arrow with slope  $\sim 4.3$ ) (Ali et al., 2015; Jassem et al.,  
10 530 2018).

11 531 **Supplementary File 1** - Calculation of the thermodynamic equilibria by Rxn tool of The  
12 532 Geochemist's Workbench® code (Bethke and Yeakel, 2008) and  $P = 20$  MPa thermodynamic  
13 533 dataset (Boschetti et al., 2016). To reduce the variables, the activity of calcium and hydrogen  
14 534 was rewritten as log-ratio in the reaction and automatically rebalanced by the tool.

## 15 535

## 16 536 **References**

17 537

18 538 Abbas, L.K., Mahdi, T.A., 2019. Reservoir units of Mishrif Formation in Majnoon Oil field,  
19 539 Southern Iraq. *Iraqi Journal of Science* 60, 2656-2663.

20 540 Abeed, Q., Leythaeuser, D., Littke, R., 2012. Geochemistry, origin and correlation of crude  
21 541 oils in Lower Cretaceous sedimentary sequences of the southern Mesopotamian Basin,  
22 542 southern Iraq. *Organic Geochemistry* 46, 113-126.

23 543 Abeed, Q., Littke, R., Strozyk, F., Uffmann, A.K., 2013. The Upper Jurassic–Cretaceous  
24 544 petroleum system of southern Iraq: A 3-D basin modelling study. *GeoArabia* 18, 179-200.

25 545 Al-Ameri, T.K., Jafar, M.S., Pitman, J., 2011. Hydrocarbon generation modeling of the  
26 546 Basrah oil fields, Southern Iraq. University of Baghdad, Jadiriya, AAPG Annual  
27 547 Convention and Exhibition. AAPG Search and Discovery, Houston, Texas.

28 548 Al-Furaiji, M., 2016. Hyper-saline produced water treatment for beneficial use. University of  
29 549 Twente, Gildeprint - The Netherlands.

30 550 Al-Kinani, S.A.A., Falih, A.H., Al-abidin, H.A.Z., Al-Naseri, S.K.A.A.H., 2018.  
31 551 Determination of the Meteoric Water Line Using Stable Isotopes in Precipitations at Several  
32 552 Locations In Baghdad. *Iraqi Journal of Science and Technology* 4, 36-42.

33 553 Al-Mallah, I.A., 2014. Assessment of the Environmental, Hydrological and Hydrogeological  
34 554 changes of the Main Drain, Iraq, College of Science - Department of Geology. University of  
35 555 Basrah, Basrah, Iraq.

36 556 Al-Marsoumi, A.M.H., Abdul-Wahab, D.S., 2005. Hydrogeochemistry of Yamama Reservoir  
37 557 formation water - west Qurna oil field - Southern Iraq. *Basrah Journal of Science* 23, 10-20.

558 Al-Mimar, H.S., Awadh, S.M., 2019. The Role of Chemistry of the Oil-Field Water in the  
1  
2 559 Distribution of Reservoir Pressures: A Case Study of Mishrif Reservoir in the Southern Oil-  
3  
4 560 Fields, Iraq. *Journal of Petroleum Research & Studies* 22, E52-E64.

5  
6 561 Al-Mimar, H.S., Awadh, S.M., Al-Yaseri, A.A., Yaseen, Z.M., 2018. Sedimentary units-  
7  
8 562 layering system and depositional model of the carbonate Mishrif reservoir in Rumaila  
9  
10 563 oilfield, Southern Iraq. *Modeling Earth Systems and Environment* 4, 1449-1465.

11 564 Al-Shamkhani, M.T., 2013. *Managing, Controlling and Improving the Treatment of Produced*  
12  
13 565 *Water Using the Six Sigma Methodology for the Iraqi Oil Fields*, College of Engineering and  
14  
15 566 *Computer Science - Department of Industrial Engineering and Management Systems*.  
16  
17 567 *University of Central Florida, Orlando, Florida*.

18 568 Al-Ziayyir, H.G.F., 2018. *Mineralisation-Related Flow Heterogeneity within the Zubair*  
19  
20 569 *Formation in the Rumaila Oilfield, Southern Iraq*, Faculty of Science and Engineering.  
21  
22 570 *University of Manchester, Manchester*.

23 571 Ali, K.K., Al-Kubaisi, Q.Y., Al-Paruany, K.B., 2015. Isotopic study of water resources in a  
24  
25 572 semi-arid region, western Iraq. *Environmental Earth Sciences* 74, 1671-1686.

27 573 Alsharhan, A.S., Nairn, A.E.M., 1988. A review of the Cretaceous Formations in the Arabian  
28  
29 574 Peninsula and Gulf: Part II. Mid-Cretaceous (Wasia Group) Stratigraphy and Paleogeography.  
30  
31 575 *Journal of Petroleum Geology* 11, 89-112.

32 576 Alyasi, A.I., Al-Jawad, S.N., Alshabender, L.Y., 2014. Geophysical Study to the Role of Salt  
34  
35 577 in Creating Buzurgan Oilfield Structure, Southeast of Iraq. *Iraqi Journal of Science* 55, 1579-  
36  
37 578 1587.

38 579 Aqrabi, A.A.M., Horbury, A.D., Sadooni, F.N., Goff, J.C., 2010. *The Petroleum Geology of*  
39  
40 580 *Iraq*. Scientific Press, Beaconsfield, Bucks, UK.

41 581 Aqrabi, A.A.M., Thehni, G.A., Sherwani, G.H., Kareem, B.M.A., 1998. Mid-Cretaceous  
43  
44 582 rudist-bearing carbonates of the Mishrif Formation: an important reservoir sequence in the  
45  
46 583 Mesopotamian Basin, Iraq. *Journal of Petroleum Geology* 21, 57-82.

47 584 Awadeesian, A.M., Awadh, S.M., Al-Dabbas, M.A., Al-Maliki, M.M., Al-Jawad, S.N.,  
48  
49 585 Hussein, A.K.S., 2019. A modified water injection technique to improve oil recovery: Mishrif  
50  
51 586 carbonate reservoirs in Southern Iraq oil fields, case study. *Iraqi Geological Journal* 52, 125-  
52  
53 587 146.

54 588 Awadh, S., Al-Mimar, H., Al-yaseri, A., 2019a. Potentiometric Salinity Mapping of Mishrif  
55  
56 589 Oilfield Waters in (Iraq's) Southern Oil Fields, in: Chaminé, H.I., Barbieri, M., Kisi, O.,  
57  
58 590 Chen, M., Merkel, B.D. (Eds.), *Advances in Sustainable and Environmental Hydrology,*  
59  
60 591 *Hydrogeology, Hydrochemistry and Water Resources - Proceedings of the 1st Springer*

592 Conference of the Arabian Journal of Geosciences (CAJG-1), Tunisia 2018. Springer Nature,  
1 Switzerland, pp. 49-52.  
2  
3  
4 594 Awadh, S.M., Al-Auweidy, M.R., Al-Yaseri, A.A., 2019b. Hydrochemistry as a tool for  
5 interpreting brine origin and chemical equilibrium in oilfields: Zubair reservoir southern Iraq  
6  
7 596 case study. Applied Water Science, 93.  
8  
9 597 Awadh, S.M., Al-Mimar, H.S., Al-Yaseri, A.A., 2018. Salinity mapping model and brine  
10 chemistry of Mishrif reservoir in Basrah oilfields, Southern Iraq. Arabian Journal of  
11 598 Geosciences 11.  
12  
13  
14 600 Babel, M., Schreiber, B.C., 2014. Geochemistry of Evaporites and Evolution of Seawater in:  
15  
16 601 Holland, H.D., Turekian, K.K. (Eds.), Treatise on Geochemistry, 2nd ed. Elsevier, Printed  
17  
18 602 and bound in Italy, pp. 483-560.  
19  
20 603 Bagheri, R., Nadri, A., Raeisi, E., Eggenkamp, H.G.M., Kazemi, G.A., Montaseri, A., 2014.  
21  
22 604 Hydrochemical and isotopic ( $\delta^{18}\text{O}$ ,  $\delta^2\text{H}$ ,  $^{87}\text{Sr}/^{86}\text{Sr}$ ,  $\delta^{37}\text{Cl}$  and  $\delta^{81}\text{Br}$ ) evidence for the origin of  
23  
24 605 saline formation water in a gas reservoir. Chemical Geology 384, 62-75.  
25  
26 606 Basilici, M., Mazzoli, S., Megna, A., Santini, S., Tavani, S., 2020. 3-D Geothermal Model of  
27  
28 607 the Lurestan Sector of the Zagros Thrust Belt, Iran. Energies 13.  
29  
30 608 Bethke, C.M., Yeakel, S., 2008. The Geochemist's Workbench® - Release 7. GWB  
31  
32 609 Essentials Guide, Hydrogeology Program. University of Illinois.  
33  
34 610 Bordenave, M.L., 2008. The origin of the Permo-Triassic gas accumulations in the Iranian  
35  
36 611 Zagros foldbelt and contiguous offshore areas: a review of the Palaeozoic petroleum system.  
37  
38 612 Journal of Petroleum Geology 31, 3-42.  
39  
40 613 Bordenave, M.L., Hegre, J.A., 2010. Current distribution of oil and gas fields in the Zagros  
41  
42 614 Fold Belt of Iran and contiguous offshore as the result of the petroleum systems, in: Leturmy,  
43  
44 615 P., Robin, C. (Eds.), Tectonic and Stratigraphic Evolution of Zagros and Makran during the  
45  
46 616 Mesozoic–Cenozoic. The Geological Society of London, London, pp. 291-353.  
47  
48 617 Boschetti, T., 2011. Application of brine differentiation and Langelier–Ludwig plots to fresh-  
49  
50 618 to-brine waters from sedimentary basins: Diagnostic potentials and limits. Journal of  
51  
52 619 Geochemical Exploration, 108, 126-130.  
53  
54 620 Boschetti, T., Angulo, B., Cabrera, F., Vásquez, J., Montero, R.L., 2016. Hydrogeochemical  
55  
56 621 characterization of oilfield waters from southeast Maracaibo Basin (Venezuela): Diagenetic  
57  
58 622 effects on chemical and isotopic composition. Marine and Petroleum Geology 73, 228-248.  
59  
60 623 Boschetti, T., Cifuentes, J., Iacumin, P., Selmo, E., 2019. Local Meteoric Water Line of  
61  
62 624 Northern Chile (18°S - 30°S): An application of error-in-variables regression to the oxygen  
63  
64 625 and hydrogen stable isotope ratio of precipitation. Water 11  
65



626 Boschetti, T., Toscani, L., Salvioli Mariani, E., 2015. Boron isotope geochemistry of  
627 Na- bicarbonate, Na- chloride, and Ca- chloride waters from the Northern Apennine  
628 Foredeep basin: other pieces of the sedimentary basin puzzle. *Geofluids* 15, 546-562.

629 Boschetti, T., Toscani, L., Shouakar-Stash, O., Iacumin, P., Venturelli, G., Mucchino, C.,  
630 Frappe, S.K., 2011. Salt waters of the Northern Apennine Foredeep Basin (Italy): origin and  
631 evolution. *Aquatic Geochemistry* 17, 71-108.

632 Clesceri, L.S., Greenberg, A.E., Eaton, A.D., 1999. Method 4500-SiO<sub>2</sub> D, Heteropoly Blue  
633 Method, Standard methods for the examination of water and wastewater, 20th. American  
634 Public Health Association, American Water Works Association, Water Environment  
635 Federation, Washington.

636 Danquigny, J.A., Matthews, J., Noman, R., Mohsen, A., 2005. Assessment of interwell  
637 communication in the carbonate Al Khalij oil field using isotope ratio water sample analysis,  
638 International Petroleum Technology Conference. IPTC, Doha, Qatar

639 Davison, M.L., Criss, R.E., 1996. Na-Ca-Cl relations in basinal fluids. *Geochimica et*  
640 *Cosmochimica Acta* 60, 2743-2752.

641 Deville de Periere, M., 2011. Origine sédimento-diagénétique de réservoirs carbonatés  
642 microporeux: exemple de la formation Mishrif (Cénomanién) du Moyen-Orient. Université  
643 de Bourgogne.

644 Ghalib, H.B., Almallah, I.A.R., 2017. Scaling simulation resulting from mixing predicted  
645 model between Mishrif formation water and different waters injection in Basrah oil field,  
646 southern Iraq. *Modeling Earth Systems and Environment* 3, 1557-1569.

647 Giggenbach, W.F., 1991. Chemical Techniques in geothermal exploration, in: D'Amore, F.  
648 (Ed.), *Application of Geochemistry in Geothermal Reservoir Development*. UNITAR, Rome,  
649 Italy, pp. 119–144.

650 Gonfiantini, R., 1965. Effetti isotopi nell'evaporazione di acque salate. *Atti della Società*  
651 *Toscana di Scienze Naturali - Memorie, Serie A* 72, 1-22.

652 Gonfiantini, R., Wassenaar, L.I., Araguas-Araguas, L., Aggarwal, P.K., 2018. A unified  
653 Craig-Gordon isotope model of stable hydrogen and oxygen isotope fractionation during  
654 fresh or saltwater evaporation. *Geochimica et Cosmochimica Acta* 235, 224-236.

655 Grabowski Jr., G.J., 2014. Iraq, in: Marlow, L., Kendall, M.C., Yose, L.A. (Eds.), *Petroleum*  
656 *systems of the Tethyan region*. The American Association of Petroleum Geologists, Tulsa,  
657 OK U.S.A., pp. 379–467.

658 Gregory, R.T., Taylor Jr, H.P., 1981. An oxygen isotope profile in a section of Cretaceous  
659 oceanic crust, Samail Ophiolite, Oman: Evidence for  $\delta^{18}\text{O}$  buffering of the oceans by deep (>

660 5 km) seawater- hydrothermal circulation at mid- ocean ridges. *Journal of Geophysical*  
661 *Research: Solid Earth* 86, 2737-2755.

662 Hadi, K., Kumar, U.S., Al-Senafy, M., Bhandary, H., 2016. Environmental isotope  
663 systematics of the groundwater system of southern Kuwait. *Environmental Earth Sciences* 75.  
664 Hajikazemi, E., Al-Aasm, I.S., Coniglio, M., 2017. Diagenetic history and reservoir  
665 properties of the Cenomanian-Turonian carbonates in southwestern Iran and the Persian Gulf.  
666 *Marine and Petroleum Geology* 88, 845-857.

667 Hajikazemi, E., Al- Aasm, I.S., Coniglio, M., 2012. Chemostratigraphy of Cenomanian–  
668 Turonian carbonates of the Sarvak Formation, southern Iran. *Journal of Petroleum Geology*  
669 35, 187-205.

670 Hamdan, A.N.A., 2017. The use of water quality index to evaluate groundwater quality in  
671 west of Basrah wells. *Kufa Journal of Engineering* 8, 51-64.

672 Holser, W., 1979. Trace elements and isotopes in evaporites, in: Burns, R.G. (Ed.), *Marine*  
673 *Minerals*. De Gruyter - Mineralogical Society of America, Berlin, Boston, pp. 295–346.

674 Hönisch, B., Ridgwell, A., Schmidt, D.N., Thomas, E., Gibbs, S.J., Sluijs, A., Zeebe, R.,  
675 Kump, L., Martindale, R.C., Greene, S.E., Kiessling, W., Ries, J., Zachos, J.C., Royer, D.L.,  
676 Barker, S., Marchitto Jr., T.M., Moyer, R., Pelejero, C., Ziveri, P., Foster, G.L., Williams, B.,  
677 2012. The geological record of ocean acidification. *Science* 335, 1058-1063.

678 Horita, J., 2009. Isotopic evolution of saline lakes in the low-latitude and polar regions.  
679 *Aquatic Geochemistry* 15, 43-69.

680 Horita, J., Cole, D.R., Wesolowski, D.J., 1993. The activity-composition relationship of  
681 oxygen and hydrogen isotopes in aqueous salt solutions: II. Vapor-liquid water equilibration  
682 of mixed salt solutions from 50 to 100 C and geochemical implications. *Geochimica et*  
683 *Cosmochimica Acta* 57, 4703-4711.

684 Hounslow, A.W., 1995. *Water Quality Data Analysis and Interpretation*. Lewis Publishers,  
685 Boca Raton, New York.

686 Jamil, A.K., 1978. Hydrochemical and Hydrodynamic Zones and the Probable Direction of  
687 Water Flow within Zubair Reservoir of Zubair and Rumaila Oil Fields (Southern Iraq).  
688 *Geologisches Jahrbuch, Reihe D, D25*, 199-211.

689 Jassem, A.A., Nada, K.B., Abdualamer, Z.S., 2018. Using  $^{18}\text{O}$ ,  $^2\text{H}$  isotopes to study the effect  
690 of fish lake on surface water in Al-Azezeya, Kut Governorate, Iraq. *The Iraqi Geological*  
691 *Journal* 51, 149-156.

692 Jassim, S.Z., Buday, T., 2006. Units of the Stable Shelf, in: Jassim, S.Z., Goff, J.C. (Eds.),  
693 *Geology of Iraq*. Dolin, Prague and Moravian Museum, Brno. Czech Republic, pp. 53-72.

694 Kharaka, Y.K., Mariner, R.H., 1989. Chemical geothermometers and their application to  
1 formation waters from sedimentary basins, in: Naeser, N.D., McCollin, T.H. (Eds.), Thermal  
2 history of sedimentary basins. Springer-Verlag, New York, pp. 99–117.  
3  
4 696 Kim, S.T., O'Neil, J.R., 1997. Equilibrium and nonequilibrium oxygen isotope effects in  
5 synthetic carbonates. 61 *Geochimica et cosmochimica acta*, 3461-3475.  
6  
7 698 Knauth, L.P., Beeunas, M.A., 1986. Isotope geochemistry of fluid inclusions in Permian  
8 halite with implications for the isotopic history of ocean water and the origin of saline  
9 formation waters. *Geochimica et Cosmochimica Acta* 50, 419-433.  
10  
11 700 Konyuhov, A.I., Maleki, B., 2006. The Persian Gulf Basin: Geological history, sedimentary  
12 formations, and petroleum potential. *Lithology and Mineral Resources* 41, 344–361  
13  
14 702 Lemarchand, D., Gaillardet, J., Lewin, E., Allegre, C.J., 2002. Boron isotope systematics in  
15 large rivers: implications for the marine boron budget and paleo-pH reconstruction over the  
16 Cenozoic. *Chemical Geology* 190, 123-140.  
17  
18 704 Lowenstein, T.K., Hardie, L.A., Timofeeff, M.N., Demicco, R.V., 2003. Secular variation in  
19 seawater chemistry and the origin of calcium chloride basinal brines. *Geology* 31, 857-860.  
20  
21 705 Mahdi, T.A., Aqrawi, A.A., Horbury, A.D., Sherwani, G.H., 2013. Sedimentological  
22 characterization of the mid-Cretaceous Mishrif reservoir in southern Mesopotamian Basin,  
23 Iraq. *GeoArabia* 18, 139-174.  
24  
25 707 McArthur, J.M., 2010. Strontium isotope stratigraphy, in: Ratcliffe, K.T., Zaitlin, B.A. (Eds.),  
26 Application of modern stratigraphic techniques: theory and case histories. SEPM Society for  
27 Sedimentary Geology, Tulsa, Oklahoma, pp. 129–142.  
28  
29 709 McArthur, J.M., Howarth, R.J., Shields, G.A., 2012. Strontium isotope stratigraphy, in:  
30 Gradstein, F.M., Ogg, J.G., Schmitz, M.D., Ogg, G.M. (Eds.), *The geologic time scale 2012*.  
31 Elsevier, Oxford, pp. 127–144.  
32  
33 712 McKenzie, J.A., Hsü, K.J., Schneider, J.F., 1980. Movement of subsurface waters under the  
34 sabkha Abu Dhabi, UAE, and its relation to evaporative dolomite genesis, in: Zenger, D.H.,  
35 Dunham, J.B., Ethington, R.L. (Eds.), *Concepts and Models of Dolomitization*. SEPM  
36 Society for Sedimentary Geology, Tulsa, Oklahoma, USA, pp. 11-30.  
37  
38 715 Mortazavi, M., Heuss-Assbichler, S., Shahri, M., 2017. Hydrothermal systems in the salt  
39 domes of south Iran. *Procedia Earth and Planetary Science* 17, 913-916.  
40  
41 717 Murriss, R.J., 1980. Middle East: stratigraphic evolution and oil habitat. *AAPG Bulletin* 64,  
42 597-618.  
43  
44  
45  
46  
47  
48  
49  
50  
51  
52  
53  
54  
55  
56  
57  
58  
59  
60  
61  
62  
63  
64  
65

726 Nadler, A., Magaritz, M., 1980. Studies of marine solution basins isotopic and compositional  
727 changes during evaporation, in: Nissebaum, A. (Ed.), *Hypersaline Brines and Evaporitic*  
728 *Environments*. Elsevier, Amsterdam, The Netherlands, pp. 115-129.

729 Navidtalab, A., Rahimpour-Bonab, H., Huck, S., Heimhofer, U., 2016. Elemental  
730 geochemistry and strontium-isotope stratigraphy of Cenomanian to Santonian neritic  
731 carbonates in the Zagros Basin, Iran. *Sedimentary Geology* 346, 35-48.

732 Parkhurst, D.L., Appelo, C.A.J., 2013. Description of input and examples for PHREEQC  
733 version 3: a computer program for speciation, batch-reaction, one-dimensional transport, and  
734 inverse geochemical calculations *Techniques and Methods*. US Geological Survey, Reston,  
735 VA, p. This report is Chapter 43 of Section A: Groundwater in Book 46 *Modeling*  
736 *Techniques*.

737 Rahimpour- Bonab, H., Mehrabi, H., Navidtalab, A., Omidvar, M., Enayati- Bidgoli, A.H.,  
738 Sonei, R., Sajjadi, F., Amiri-Bakhtyar, H., Arzani, N., Izadi- Mazidi, E., 2013.  
739 Palaeo- exposure surfaces in Cenomanian–santonian carbonate reservoirs in the Dezful  
740 embayment, SW Iran. *Journal of Petroleum Geology* 36, 335-362.

741 Robinson, B.W., Gunatilaka, A., 1991. Stable isotope studies and the hydrological regime of  
742 sabkhas in southern Kuwait, Arabian Gulf. *Sedimentary Geology* 73, 141-159.

743 ROPME, 2011. The Marshes-Shatt al-Arab- Gulf System, in: *Environment, R.O.f.t.P.o.t.M.*  
744 (Ed.). Marine Science Centre – University of Basra in Cooperation with Ministry of  
745 Environment Iraq, p. 102.

746 Rosenthal, E., 1997. Thermomineral waters of Ca-chloride composition: review of  
747 diagnostics and of brine evolution. *Environmental Geology* 32, 245-250.

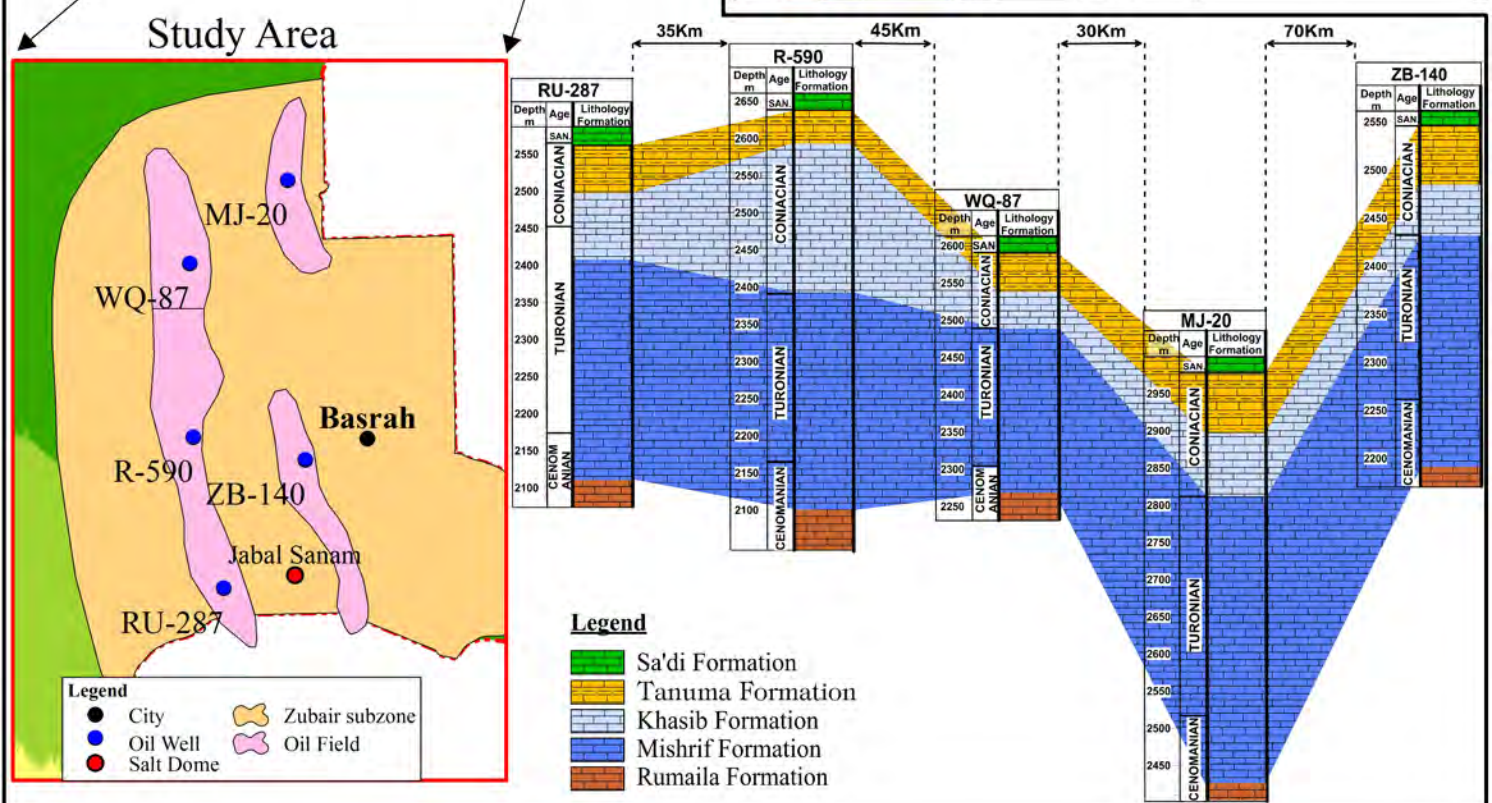
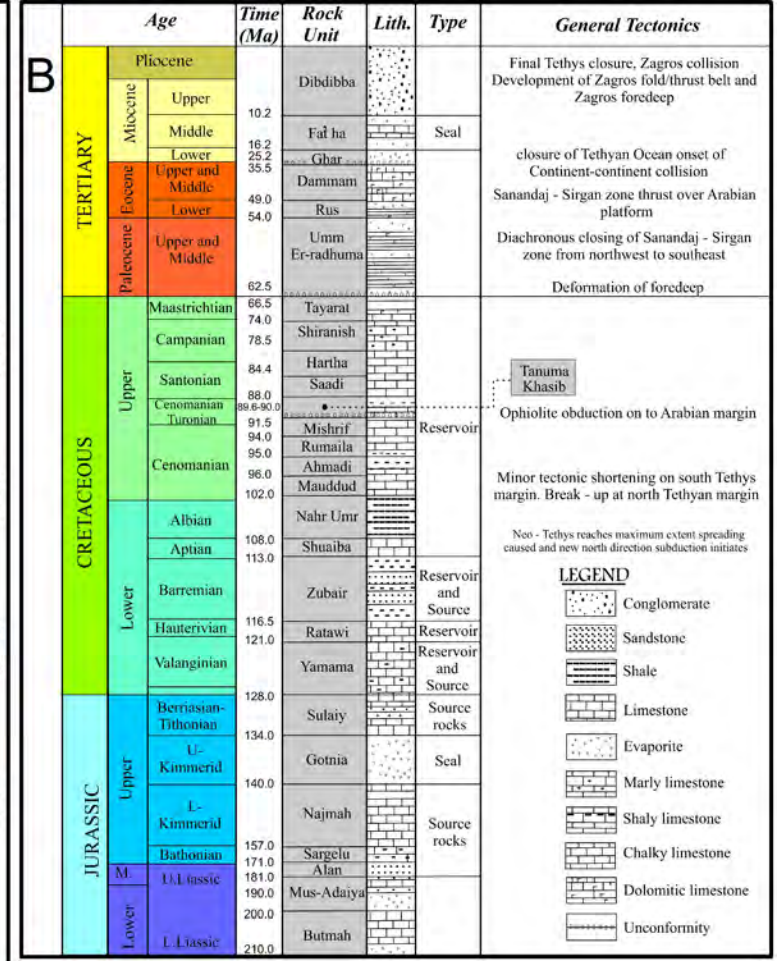
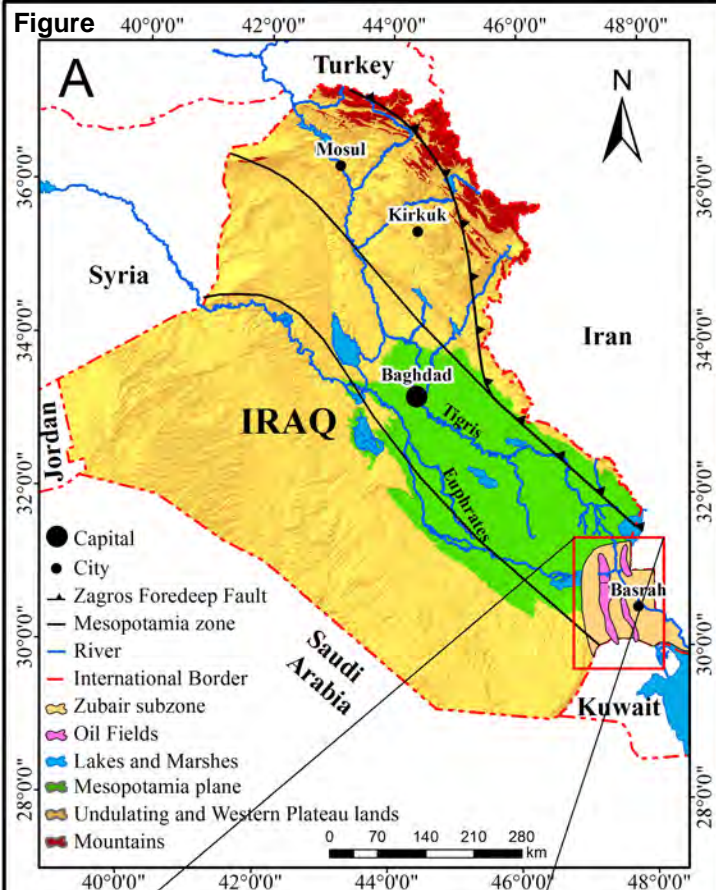
748 Ryb, U., Eiler, J.M., 2018. Oxygen isotope composition of the Phanerozoic ocean and a  
749 possible solution to the dolomite problem. *Proceedings of the National Academy of Sciences*  
750 115, 6602-6607.

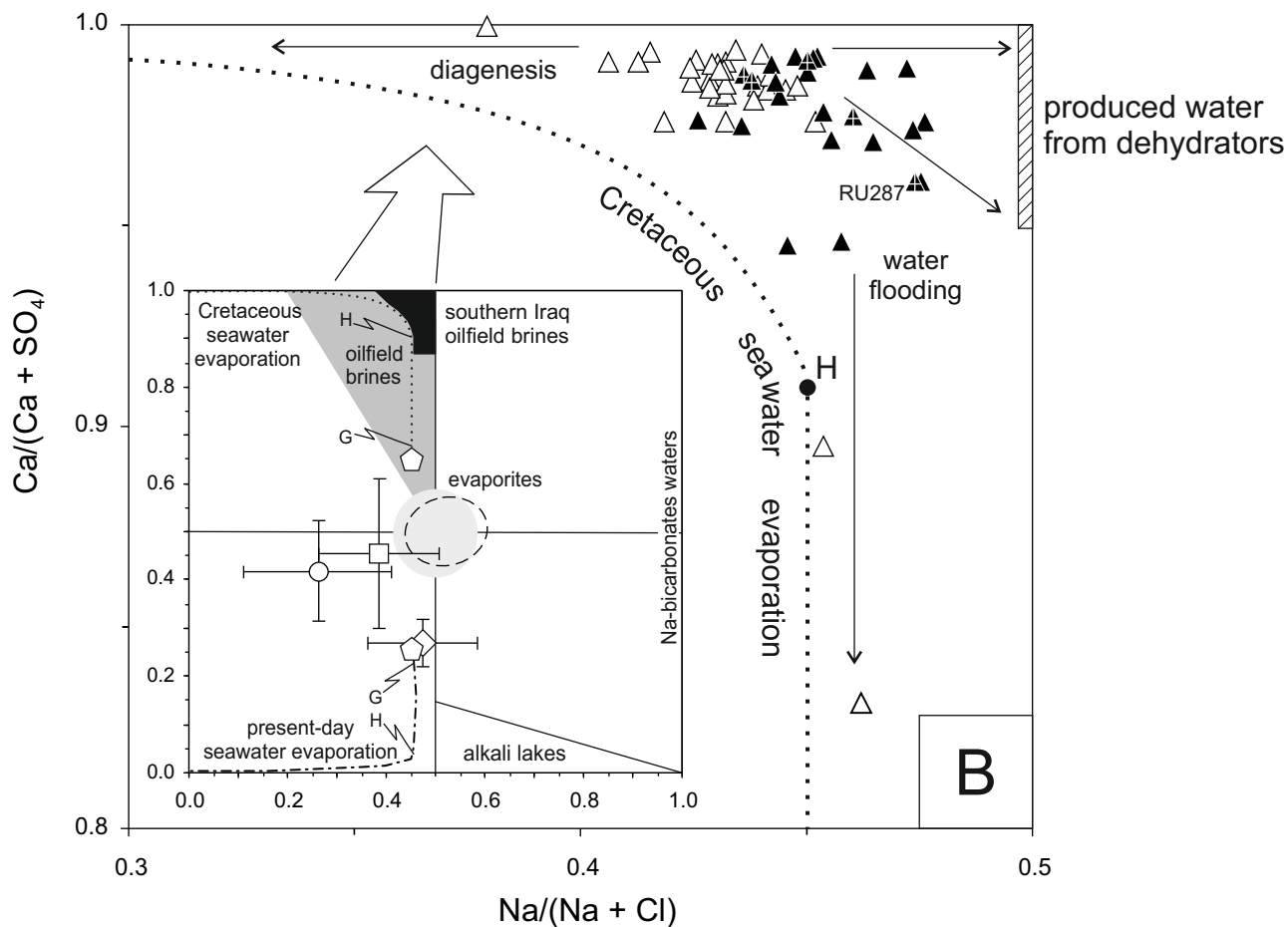
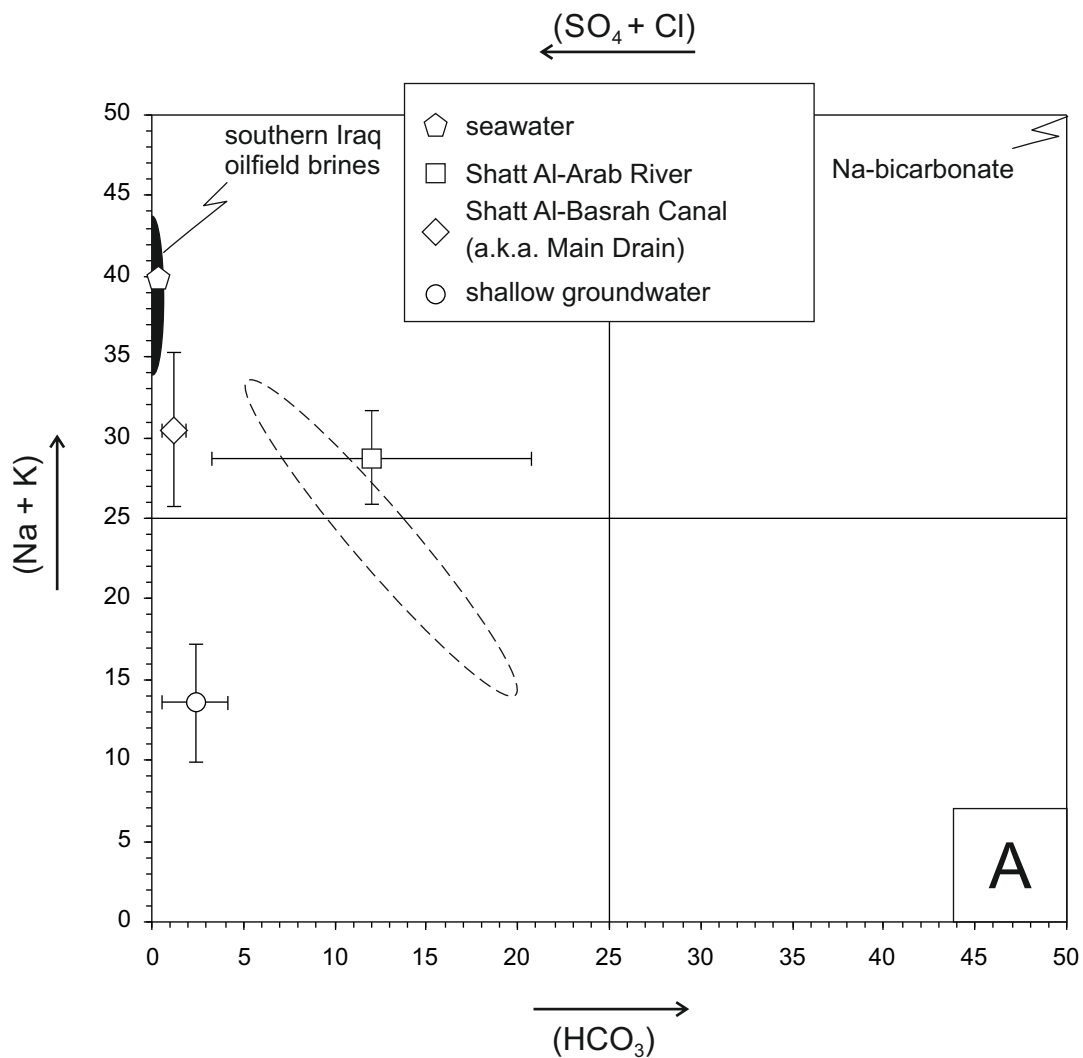
751 Rzóśka, J., 1980. *Euphrates and Tigris, Mesopotamian ecology and destiny*. Dr. W. Junk by  
752 Publishers, The Hague The Netherlands.

753 Sadooni, F.N., 2005. The nature and origin of Upper Cretaceous basin-margin rudist buildups  
754 of the Mesopotamian Basin, southern Iraq, with consideration of possible hydrocarbon  
755 stratigraphic entrapment. *Cretaceous Research* 26, 213-224.

756 Sadooni, F.N., Aqrawi, A.A.M., 2000. Cretaceous sequence stratigraphic and petroleum  
757 potential of the Mesopotamian basin, Iraq, in: Alsharhan, A.S., Scott, R.W. (Eds.), *Middle*  
758 *East Models of Jurassic/Cretaceous Carbonate Systems*. SEPM Society for Sedimentary  
759 *Geology*, Tulsa, Oklahoma, USA, pp. 315-334.

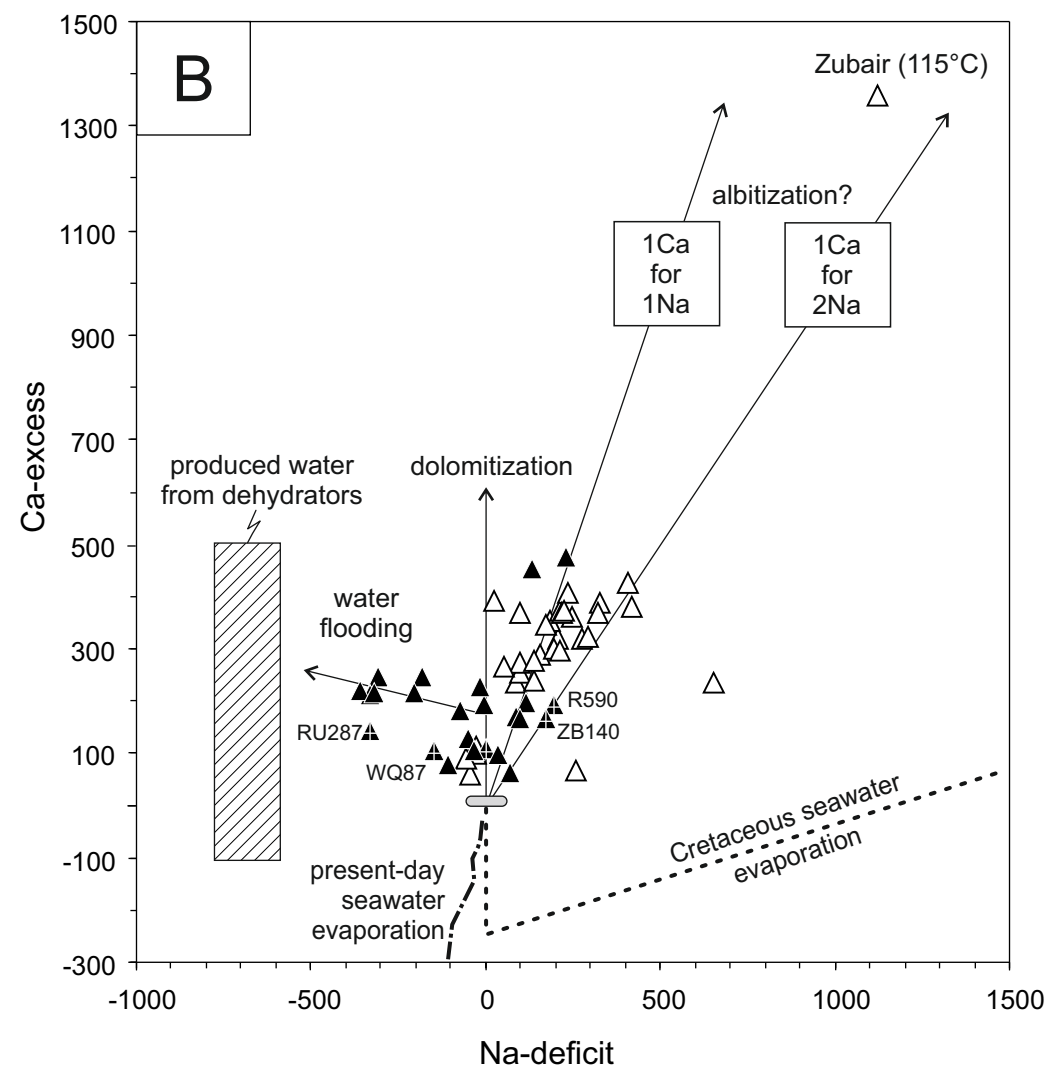
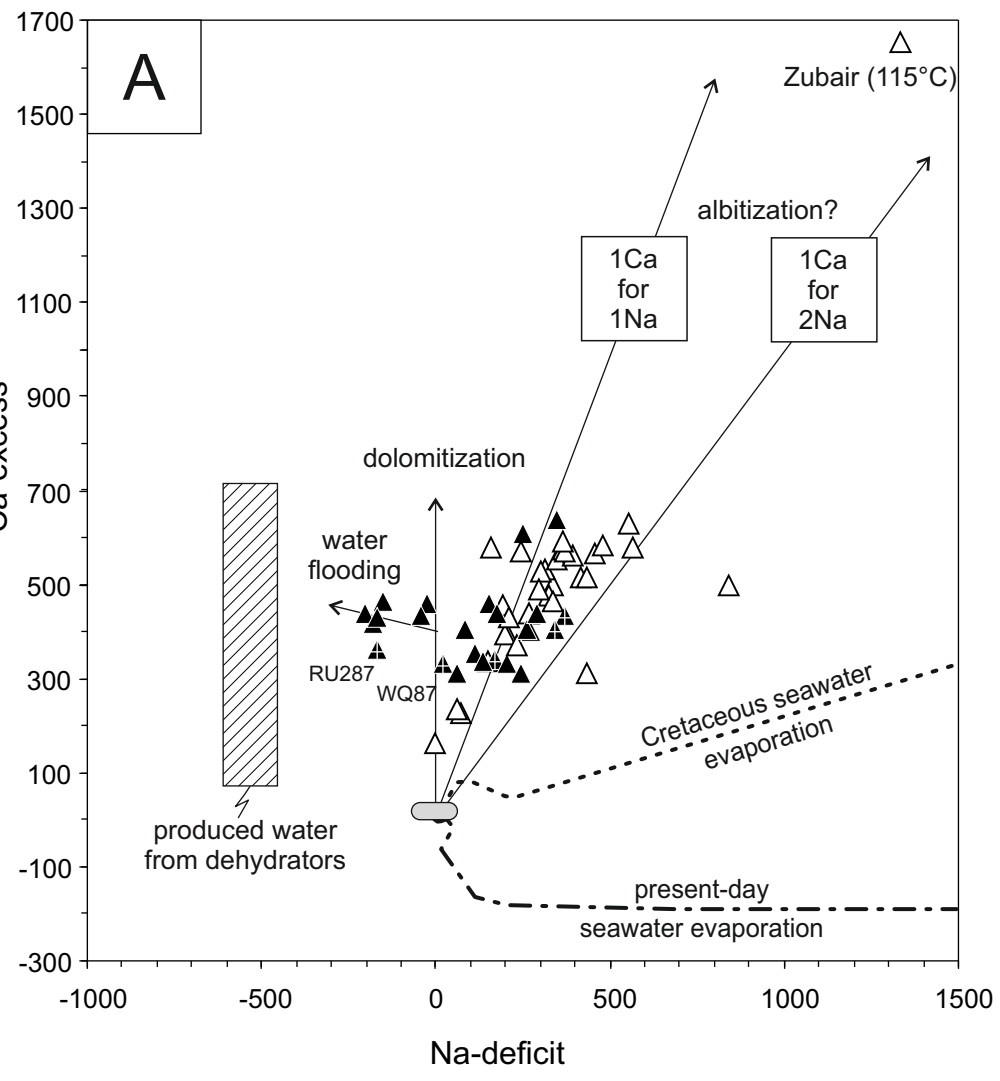
760 Sanjuan, B., Millot, R., Asmundsson, R., Brach, M., Giroud, N., 2014. Use of two new Na/Li  
1 761 geothermometric relationships for geothermal fluids in volcanic environments. *Chemical*  
2 762 *Geology* 389, 60-81.  
3  
4  
5 763 Sessions, A.L., 2016. Factors controlling the deuterium contents of sedimentary  
6 764 hydrocarbons. *Organic Geochemistry* 96, 43–64.  
7  
8  
9 765 Singh, P., 2012. New Insights to the Implications of Salt Tectonics in the Northern Part of  
10 766 Kuwait Arch: An Integrated Modeling Study, First EAGE Workshop on Iraq-Hydrocarbon  
11 767 Exploration and Field Development. European Association of Geoscientists & Engineers  
12 768 (EAGE), Istanbul, Turkey  
13  
14  
15  
16 769 Sissakian, V., Abdul Ahad, A., Al-Ansari, N., Knutsson, S., 2017. Geomorphology, Geology  
17 770 and Tectonics of Jabal Sanam, Southern Iraq. *Journal of Earth Sciences and Geotechnical*  
18 771 *Engineering* 7, 97-113.  
19  
20  
21  
22 772 Sorbie, K.S., Mackay, E.J., 2000. Mixing of injected, connate and aquifer brines in  
23 773 waterflooding and its relevance to oilfield scaling. *Journal of Petroleum Science and*  
24 774 *Engineering*. 27, 85-106.  
25  
26  
27 775 Taha, T.M., Abdullah, E.J., 2019. Reconstruction of Paleo depth and Paleo temperature from  
28 776 C-O stable isotope records of Mishrif Formation, southern Iraq. *Iraqi Journal of Science* 60,  
29 777 1730-1742.  
30  
31  
32  
33 778 Vengosh, A., Starinsky, A., Kolodny, Y., Chivas, A.R., Raab, M., 1992. Boron isotope  
34 779 variations during fractional evaporation of sea water: new constraints on the marine vs.  
35 780 nonmarine debate. *Geology* 20, 799–802.  
36  
37  
38 781 Wang, Y., Huang, C., Sun, B., Quan, C., Wu, J., Lin, Z., 2014. Paleo-CO<sub>2</sub> variation trends  
39 782 and the Cretaceous greenhouse climate. *Earth-Science Reviews* 129, 136-147.  
40  
41  
42 783 Wolery, T.W., Jarek, R.L., 2003. EQ3/6, version 8.0—software user’s manual. Civilian  
43 784 radioactive waste management system, Management & Operating Contractor, Sandia  
44 785 National Laboratories, Albuquerque, New Mexico.  
45  
46  
47 786 Yurtsever, Y., 1994. Role of environmental isotopes in studies related to salinization  
48 787 processes and salt water intrusion dynamics, 13th Salt Water Intrusion Meeting - Session 3:  
49 788 Hydrogeochemical and environmental isotope studies. Mixing zone. Characterization of the  
50 789 origin and dynamics of salt and brackish waters, Cagliari, Italy, pp. 5-10.  
51  
52  
53  
54 790 Zheng, Y.-F., 1999. Oxygen isotope fractionation in carbonate and sulfate minerals.  
55 791 *Geochemical Journal* 33, 109-126.  
56  
57  
58  
59  
60  
61  
62  
63  
64  
65





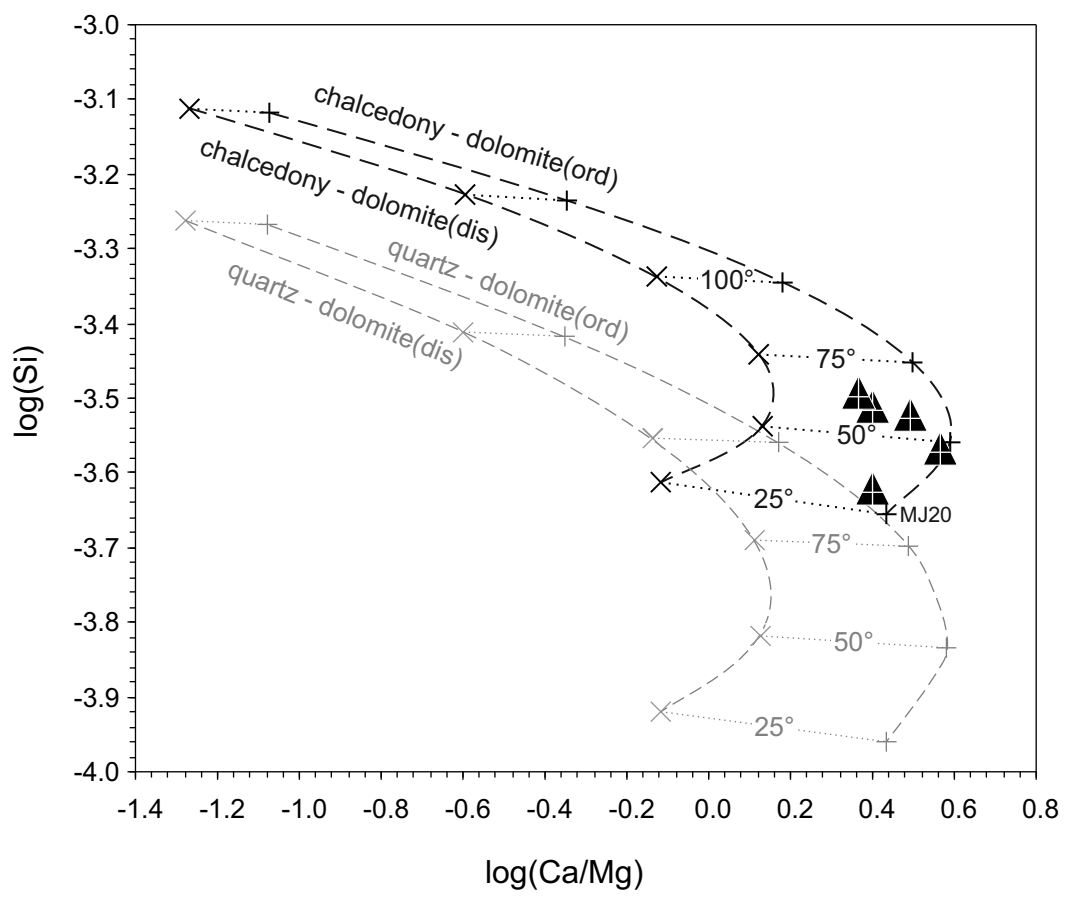
1  
2  
3  
4  
5  
6  
7  
8  
9  
10  
11  
12  
13  
14  
15  
16  
17  
18  
19  
20  
21  
22  
23  
24  
25  
26  
27  
28  
29  
30  
31  
32  
33  
34  
35  
36  
37  
38  
39  
40  
41  
42  
43  
44  
45  
46  
47  
48  
49  
50  
51  
52  
53  
54  
55  
56  
57  
58  
59  
60  
61  
62  
63  
64  
65

1  
2  
3  
4  
5  
6  
7  
8  
9  
10  
11  
12  
13  
14  
15  
16  
17  
18  
19  
20  
21  
22  
23  
24  
25  
26  
27  
28  
29  
30  
31  
32  
33  
34  
35  
36  
37  
38  
39  
40  
41  
42  
43  
44  
45  
46  
47  
48  
49

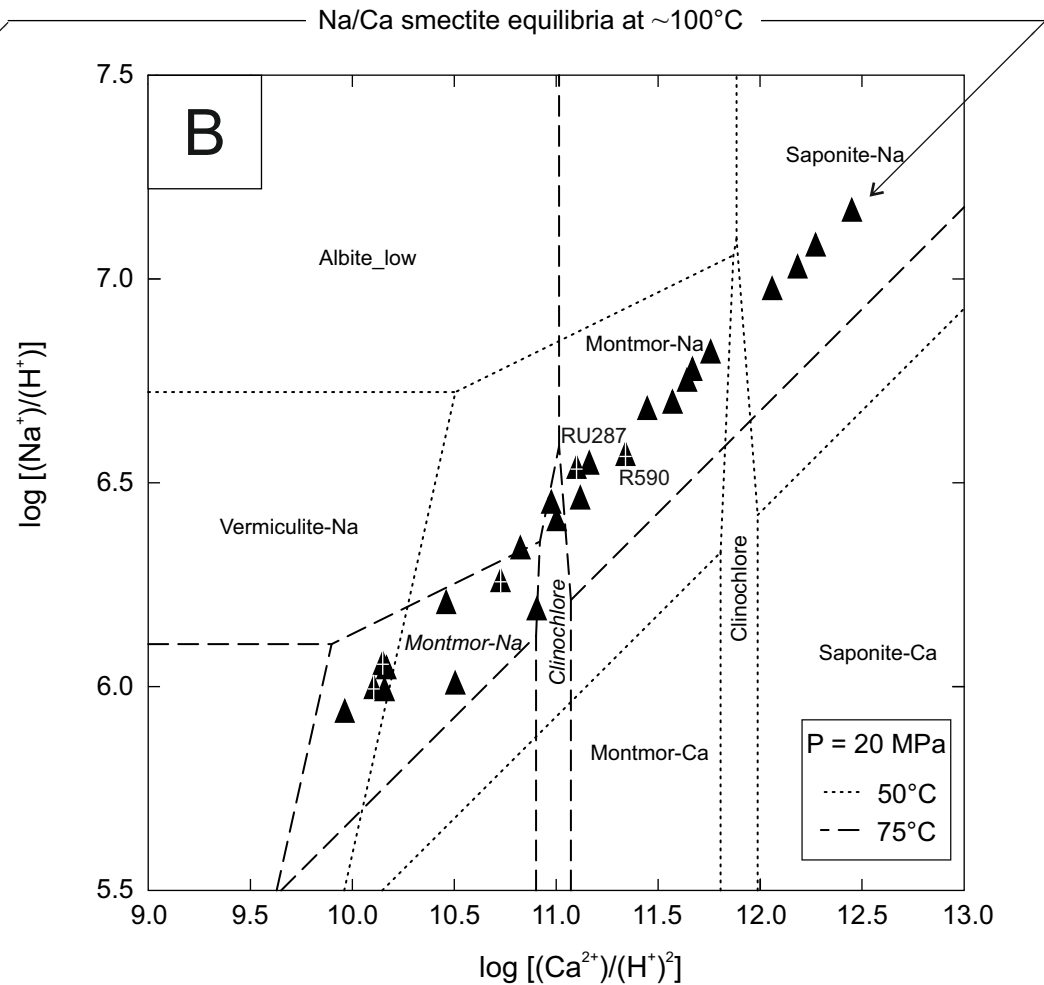
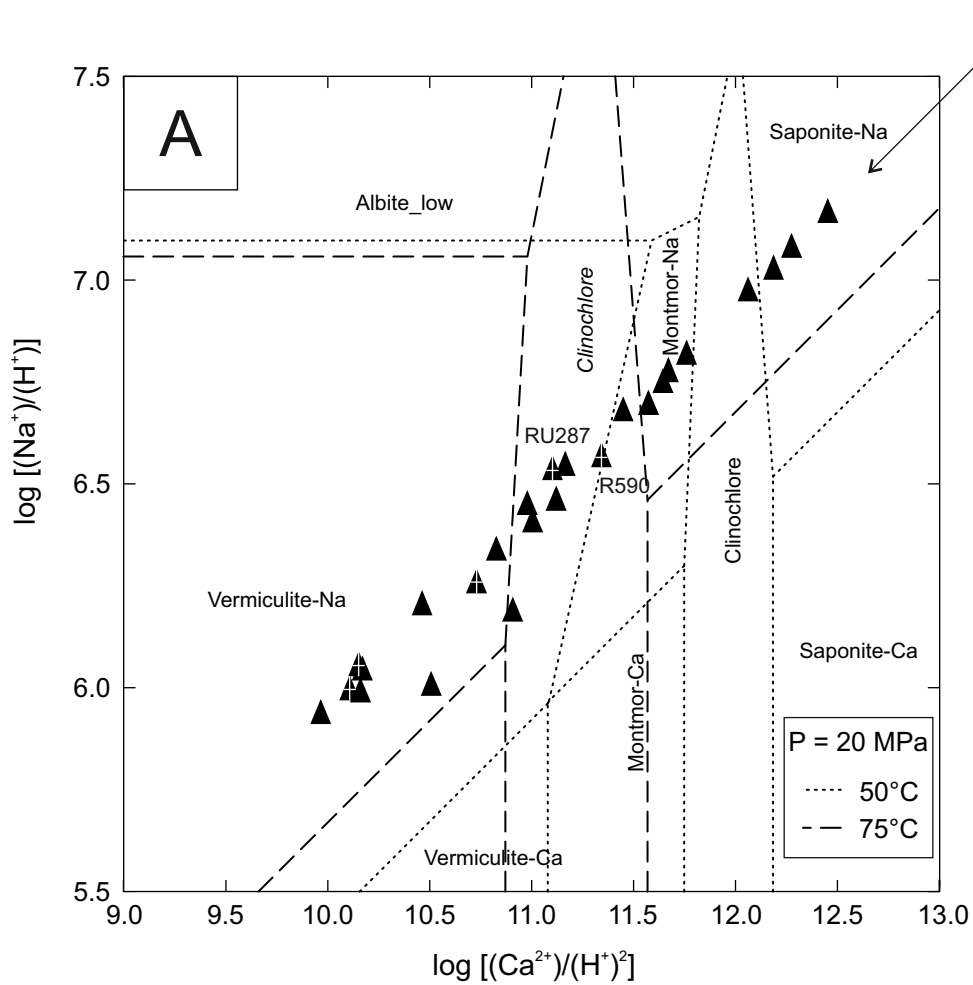




1  
2  
3  
4  
5  
6  
7  
8  
9  
10  
11  
12  
13  
14  
15  
16  
17  
18  
19  
20  
21  
22  
23  
24  
25  
26  
27  
28  
29  
30  
31  
32  
33  
34  
35  
36  
37  
38  
39  
40  
41  
42  
43  
44  
45  
46  
47  
48  
49  
50  
51  
52  
53  
54  
55  
56  
57  
58  
59  
60  
61  
62  
63  
64  
65



1  
2  
3  
4  
5  
6  
7  
8  
9  
10  
11  
12  
13  
14  
15  
16  
17  
18  
19  
20  
21  
22  
23  
24  
25  
26  
27  
28  
29  
30  
31  
32  
33  
34  
35  
36  
37  
38  
39  
40  
41  
42  
43  
44  
45  
46  
47  
48  
49



1  
2  
3  
4  
5  
6  
7  
8  
9  
10  
11  
12  
13  
14  
15  
16  
17  
18  
19  
20  
21  
22  
23  
24  
25  
26  
27  
28  
29  
30  
31  
32  
33  
34  
35  
36  
37  
38  
39  
40  
41  
42  
43  
44  
45  
46  
47  
48  
49  
50  
51  
52  
53  
54  
55  
56  
57  
58  
59  
60  
61  
62  
63  
64  
65

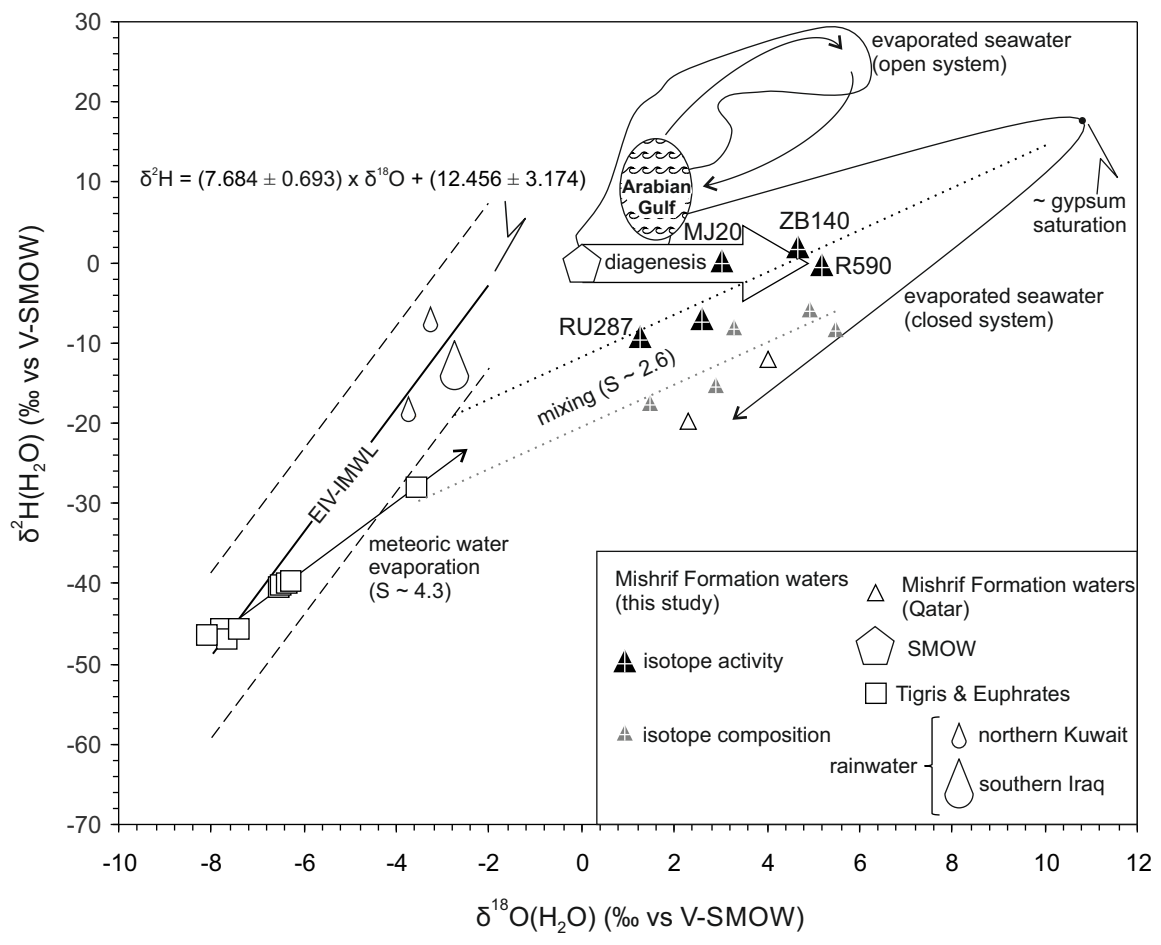


Table 1

borehole code	unit	RU287	R590	WQ87	MJ20	*ZB140	mean	±	std.dev.	CV %	N	reference
depth oil	m	2438	2682	2295	2836	2464	2412	±	118	5	28	Awadh et al. 2018
depth water	m	2700	2362	2316	2646	2377	2588	±	151	6	28	Awadh et al. 2018
oil pressure	kPa	29027	27717	25511	28613	27614	26977	±	1139	4	28	Awadh et al. 2018
water pressure	kPa	28751	30337	24759	32095	28269	28185	±	2292	8	28	Awadh et al. 2018
Temperature	°C	66	65	67	60	64	65	±	2	3	28	Awadh et al. 2018
pH		6.0	6.1	5.5	5.5	5.8	6.0	±	0.4	6	28	Awadh et al. 2018
Eh (S <sup>-II</sup> /S <sup>VI</sup> redox couple)	V	-	-0.165	-0.118	-0.120	-0.140	-0.144	±	0.023	-16	8	this study
TDS	mg/l	235500	255997	248000	249123	246798	243342.75	±	21229	9	28	Awadh et al. 2018
Na	mg/l	83500	77987	82413	80945	77994	78508	±	8561	11	28	Awadh et al. 2018
Ca	mg/l	10300	11980	9870	10105	11356	11417	±	1351	12	28	Awadh et al. 2018
Mg	mg/l	2000	2895	2587	2445	1880	2391	±	543	23	28	Awadh et al. 2018
K	mg/l	1750	2740	1800	2290	480	1709	±	767	45	28	Awadh et al. 2018
Cl	mg/l	143000	155341	148900	152410	154260	145857	±	14281	10	28	Awadh et al. 2018
SO <sub>4</sub>	mg/l	1000	360	550	213	385	595	±	347	58	28	Awadh et al. 2018
HCO <sub>3</sub>	mg/l	200	120	162	416	196	208	±	89	43	28	Awadh et al. 2018
sulfide as S	mg/l	-	144	68	64	86	103	±	38	37	8	this study
Li	mg/l	4.20	4.06	3.88	5.28	3.09	4.35	±	0.90	21	9	this study
Ba	mg/l	1.77	1.79	1.71	5.43	1.44	2.28	±	1.73	76	9	this study
Sr	mg/l	392	384	365	330	299	371	±	47	13	9	this study
Rb	mg/l	0.80	0.90	0.80	0.80	0.80	0.86	±	0.09	10	9	this study
Fe	mg/l	0.20	0.25	0.22	0.25	0.18	0.25	±	0.04	16	9	this study
Mn	mg/l	0.12	0.12	0.13	4.47	0.10	0.82	±	1.52	184	9	this study
SiO <sub>2</sub>	mg/l	15.5	17.0	16.5	13.0	15.0	15.4	±	1.6	10	5	this study
B	mg/l	31.1	28.1	30.8	21.9	24.9	27.4	±	3.9	14	5	Awadh et al. 2018
δ <sup>11</sup> B	‰	35.8	35.9	35.8	33.7	35.6	35.4	±	0.9	3	5	Awadh et al. 2018
δ <sup>18</sup> O(H <sub>2</sub> O)c	‰	1.47	5.48	2.89	3.30	4.94	3.6	±	1.6	45	5	this study
δ <sup>2</sup> H(H <sub>2</sub> O)c	‰	-17.4	-8.4	-15.3	-8.1	-5.8	-11.0	±	5.0	-46	5	this study
10 <sup>3</sup> lnΓ( <sup>18</sup> O)	‰	-0.23	-0.29	-0.31	-0.26	-0.26	-0.27	±	0.03	-11	5	this study

1  
2  
3  
4  
5  
6  
7  
8  
9  
10  
11  
12  
13  
14  
15  
16  
17  
18  
19  
20  
21  
22  
23  
24  
25  
26  
27  
28  
29  
30  
31  
32  
33  
34  
35  
36  
37  
38  
39  
40  
41  
42  
43  
44  
45  
46  
47  
48  
49

$10^3 \ln \Gamma(^2\text{H})$	‰	8.0	8.0	8.3	8.3	7.8	8.1 ± 0.2	3	5	this study
$\delta^{18}\text{O}(\text{H}_2\text{O})_a$	‰	1.24	5.19	2.58	3.04	4.68	3.35 ± 1.60	48	5	this study
$\delta^2\text{H}(\text{H}_2\text{O})_a$	‰	-9.40	-0.42	-6.99	0.18	1.93	-2.94 ± 4.95	-168	5	this study
$^{87}\text{Sr}/^{86}\text{Sr}$		0.707729	0.707749	0.707724	0.708043	0.707713	0.707792 ± 0.000141	0.02	5	this study

---

\* boron concentration and stable isotope ratio from ZB142 borehole (*in italic*).  
- not measured or not detected.

Table 2

	RU287	R590	WQ87	MJ20	ZB140	mean	±	std.dev.	CV %	N	
	geothermometers [°C]										reference
Li-Mg	65	61	61	68	59	64	±	5	8	9	Kharaka and Mariner 1989 (equation 19 in that work)
Li-Mg	64	59	59	68	57	63	±	6	9	9	Kharaka and Mariner 1989 (equation 18 in that work)
*Quartz	97	97	101	86	89	94	±	6	7	5	Kharaka and Mariner 1989 (table 6.4, equation 1 in that work)
*Chalcedony	67	66	71	55	58	64	±	7	10	5	Kharaka and Mariner 1989 (table 6.4, equation 2 in that work)
Na-Li	40	41	38	47	34	42	±	6	13	9	Kharaka and Mariner 1989 (table 6.4, equation 8 in that work)
Na-Li	40	41	39	48	34	42	±	6	13	9	Sanjuan et al. 2014 (equation 9 in that work)
δ <sup>11</sup> B	19	18	19	32	20	21	±	6	27	5	Boschetti et al. 2015
†δ <sup>11</sup> B-corrected	61	61	61	74	61	64	±	6	9	5	Boschetti et al. 2015; this work
B	73	70	72	62	66	68	±	5	7	5	Boschetti et al. 2016 (equation 3 in that work)
♣mean	66	63	65	68	60						
♣std.dev.	4	4	6	4	3						
	saturation indexes [SI = (logIAP)/(logK)]										code
calcite	1.1	1.0	0.58	0.87	0.92	1.1	±	0.4	34	28	PHREEQCI
aragonite	0.77	0.69	0.24	0.54	0.59	0.78	±	0.38	48	28	PHREEQCI
magnesite	-0.13	-0.27	-0.56	-0.40	-0.44	-0.18	±	0.33	-179	28	PHREEQCI
rhodochrosite	-4.04	-4.31	-4.60	-2.70	-4.31	-3.9	±	0.8	-22	9	PHREEQCI
siderite	-3.16	-3.44	-3.80	-3.40	-3.51	-3.4	±	0.3	-10	9	PHREEQCI
strontianite	-1.19	-1.49	-1.78	-1.55	-1.55	-1.4	±	0.4	-25	9	PHREEQCI
♣carbonates-SS	0.22	0.11	-0.44	-0.21	-0.089	-	±	0.261	-319	5	EQ3/6
dolomite-disordered	1.5	1.4	0.55	1.1	1.0	1.5	±	0.8	52	28	PHREEQCI
dolomite-ordered	1.9	1.8	0.95	1.5	1.4	1.9	±	0.8	41	28	PHREEQCI
quartz	0.30	0.30	0.33	0.25	0.24	0.28	±	0.03	12	5	PHREEQCI
chalcedony	-0.024	-	0.0088	-	-0.082	-	±	0.040	-100	5	PHREEQCI
anhydrite	0.094	-0.36	-0.13	-0.65	-0.33	-0.21	±	0.28	-134	28	PHREEQCI
gypsum	-0.15	-0.58	-0.39	-0.82	-0.54	-0.43	±	0.27	-63	28	PHREEQCI
barite	0.061	-0.42	-0.21	-	-0.43	-0.45	±	0.58	-129	9	PHREEQCI
halite	-0.44	-0.50	-0.41	-0.47	-0.53	-0.50	±	0.15	-31	28	PHREEQCI
logP(CO <sub>2</sub> )g	-0.45	-0.77	-0.050	0.352	-0.25	-0.46	±	0.41	-91	28	PHREEQCI

\* the equation takes into account the effects of pressure and salinity on mineral solubility;

1  
2  
3  
4  
5  
6  
7  
8  
9  
10  
11  
12  
13  
14  
15  
16  
17  
18  
19  
20  
21  
22  
23  
24  
25  
26  
27  
28  
29  
30  
31  
32  
33  
34  
35  
36  
37  
38  
39  
40  
41  
42  
43  
44  
45  
46  
47  
48  
49

- † before calculation, both the effect due to Cretaceous seawater (-3‰) and evaporation (-4‰) were subtracted from the values of the brine samples (Table 1);
- ♣ all geothermometric results were considered, except those from Na-Li equations and uncorrected  $\delta^{11}\text{B}$ . For MJ20, the standard deviation was calculated considering the central value of the temperature obtained by quartz and calcedony equation (see Fig. 4 and text for details).
- ♣ calcite, magnesite, siderite, strontianite and rhodocrosite solid solution.

**Supplementary Material (for online publication only)**

[Click here to download Supplementary Material \(for online publication only\): Supplementary File 1.docx](#)



**Author Contributions:** Conceptualization, TB, SMA and ZMY; Data curation, SMA and TB; Formal analysis, TB, SMA, HSA, PI, LT, ES and ZMY; Investigation, TB, SMA, HSA, PI, LT, ES and ZMY; Methodology, TB and SMA; Project administration, TB, SMA, and ZMY; Resources, SMA; Supervision, TB and SMA; Validation, TB, SMA, HSA, PI, LT, ES and ZM; Visualization, TB, SMA, HSA, PI, LT, ES and ZMY; Writing – original draft, TB, SMA, HSA, PI, LT, ES and ZMY; Writing– review & editing, TB, SMA and ZMY.

**Declaration of interests**

The authors declare that they have no known competing financial interests or personal relationships that could have appeared to influence the work reported in this paper.

The authors declare the following financial interests/personal relationships which may be considered as potential competing interests:

On behalf of the co-authors

Zaher Mundher Yaseen

Faculty of Civil Engineering,  
Ton Duc Thang University,  
Ho Chi Minh City,  
Vietnam  
[yaseen@tdtu.edu.vn](mailto:yaseen@tdtu.edu.vn)